Magnetic Field Effects and Biophysical Studies on DNA Charge Transport and Repair

Thesis by

Theodore Joseph Zwang

In Partial Fulfilment of the Requirements for the
Degree of Doctor of Philosophy in Chemistry

California Institute of Technology
Pasadena, California
2018
(Defended July 24, 2017)

Acknowledgements

I am forever indebted to my advisor, Jackie Barton, for guiding me through the gauntlet that is graduate school. I would never have reached this point if not for the attentive help you gave me. You always keep your door open to me and other students in the lab, despite the incredible number of responsibilities that you manage. It truly shows how much you care about our success. Your example serves as a constant reminder that it is important to make myself available to help those around me no matter how busy life gets. You are one of the most impressive people that I have ever met, and a true role model for the kind of scientist that I wish to be.

Thanks also goes to my thesis committee: Professors Doug Rees, Harry Gray, and Tom Miller. I appreciate the positivity and friendliness that you have all shown me, as well as the genuine interest you have taken in my growth as a scientist. The advice you’ve given me, both about science and being a scientist, has helped me grow into the capable person that I am today. I’m sure that I will look back on our conversations as a source of inspiration in my future career.

Michael Hill, the time you spent with me while working through my initial spin experiments is invaluable. You taught me more than just rigorous electrochemistry. You taught me to have true appreciation for rigorous science. You are a genuinely good person and someone that I look forward to seeing at conferences in the future.

My Pomona College professors, particularly Matthew Sazinsky and Malkiat Johal, sparked my desire to become a chemist. You showed me just how enjoyable and exciting research can be. I owe you my gratitude for putting me on this path. I can’t imagine myself this happy doing anything else.

I am thankful to past members of the Barton group who taught me many things. Natalie Muren helped me through some difficulty adjusting to graduate school, and really made me feel like a member of the lab. Other members, including Eric Olmon, Anna Arnold, and Pam Sontz, were positive role models whose discussions helped me learn far better than anything I read. Katie Schaefer was a good source of positivity and a real pleasure to be around. And I must thank Mike Groddick for being a good friend to me, as well as a brilliant colleague who was a pleasure to work with.

I also feel fortunate that everyone currently in the Barton group has made it a welcoming and friendly place for me. I have been working most closely with Edmund Tse and Rebekah Silva, and it has been really incredible how dedicated you both are to conducting quality research. I find it extremely motivating to be around you! I’m going to miss late night boba runs when we’re all working in lab together. Andy Zhou, you have a sense of humor that is infectious. I’m going to miss talking with you about the absurd shows we both used to watch. Kelsey Boyle, your commitment to teaching and helping others really shines through. It has been a pleasure working with you. Phil Bartels, we joined the lab around the same time and it has been quite the adventure! It’s been great having you as a colleague. Liz O’Brien, you have been doing some extraordinary work and I think your research is inspirational. It’s amazing to see how your commitment to a project with so many difficulties turned into such a wonderful story! I definitely find it motivating any time I hit a road bump. Siobhan and Stephanie, you have been great colleagues to work with and talk science with. I'm excited to see where your research goes. Adam Boynton, you have always been such a source of positivity. I appreciate all your help with safety and synthesis. Levi Ekanger, you have been a great addition to the lab. You're such a friendly and helpful person, and I can say that you've made my experiments exponentially easier with all you've done fixing up the glove bag. Yingxin Deng, you have been a great help making electrode substrates. I'm really excited to see where you take them! Adela Nano, you have been a fantastic colleague to work with. I appreciate the advice you've given me when I'm trying to troubleshoot syntheses.

I would also like to thank the administrative assistants, Mo Renta and Elisha Okawa, who have helped keep the lab running. Elisha has been a great addition to the lab and is one of the friendliest, most helpful people that I've ever worked with. I would also like to thank all of the staff in the chemistry department for the many services they keep running. Much of what you do has made my life easier and my time at Caltech more pleasant.

I would like to thank my friends, both inside and outside of Caltech, for helping keep me grounded in the world. In particular, I must thank Brandon Carroll, Zachary Nicolaou, and Nicky Young for being such great housemates and friends for my entire time here. You all helped keep me happy even when everything else was driving me insane. You're all great people and I look forward to hanging out wherever the future might take us. I'm going to miss the support I've received living with you over the last six years.

Finally, I would like to thank my family for their extraordinary support through all of my education. Thank you, mom and dad, for raising me with the curiosity and creativity that I have now. Thank you, Arielle, for being a great sister that I can always talk to about anything. I feel lucky for having you in my life. Thank you all for encouraging me to pursue my passion for chemistry!

Abstract

DNA-mediated charge transport (DNA CT) is well established in both ground and excited state systems. Although theoretical models are still being developed, it is clear that the integrity of the extended π-stack of the aromatic heterocycles, the nucleic acid bases, plays a critical role. Electron donors and acceptors must be electronically well coupled into the π-stack, typically via intercalation. Perturbations that distort the π-stack, such as single-base mismatches, abasic sites, base lesions, and protein binding that kinks the double helix, attenuate DNA CT dramatically.

This thesis encompasses work that first aims to understand how DNA duplex structure informs characteristics of DNA CT and then continues to develop an understanding of the role these structural features play in biological systems. To contextualize these advancements, this first chapter outlines foundational work that has shown ways that DNA structure influences its ability to conduct charge.

Next, experiments were conducted on magnetized DNA-modified electrodes to explore spin-selective electron transport through hydrated duplex DNA. These results show that the two spins migrate through duplex DNA with a different yield and that spin selectivity requires charge transport through the DNA duplex. Significantly, shifting the same duplex DNA between right-handed B- and left-handed Z-forms leads to a diode-like switch in spin selectivity; which spin moves more efficiently through the duplex depends upon the DNA helicity. With DNA, the supramolecular organization of chiral moieties, rather than the chirality of the individual monomers, determines the selectivity in spin, and thus a conformational change can switch the spin selectivity.

This exquisite spin selectivity begged the question: how might biology take advantage of such a spin filter? Photolyase and cryptochromes both have been shown to exhibit magnetosensitive chemistry nearby a DNA binding pocket, and photolyase had previously been shown capable of DNA CT. Thus, electrochemical studies were conducted to monitor the repair of cyclobutane pyrimidine dimer lesions by *E coli* photolyase and truncated *A Thaliana* Cryptochrome 1 with an applied magnetic field. We find that the yield of dimer repair is dependent on the strength and angle of the applied magnetic field even when using magnetic fields weaker than 1 Gauss, though spin selective DNA CT is not involved. These data illustrate how cyclobutane dimer repair could be used in a biological compass that is informed by the angles of Earth's magnetic field.

Next DNA-mediated electrochemistry and atomic force microscopy studies were used to describe a role for redox active 4Fe-4S clusters in DNA-mediated charge transport signaling. DNA-modified electrochemistry shows that the 4Fe-4S cluster of DNA-bound DinG, an ATP-dependent helicase that repairs R-loops, is redox-active at cellular potentials and ATP hydrolysis increases DNA-mediated redox signaling. Atomic force microscopy experiments demonstrate that DinG and Endonuclease III, a base excision repair enzyme, cooperate at long range using DNA charge transport to redistribute to regions of DNA damage. These data are then described using an equilibrium model which elucidates fundamental characteristics of this redox chemistry that allow DNA CT to coordinate the activities of DNA repair enzymes across the genome.

The importance of the oxidation state of the redox-active [4Fe4S] cluster in the DNA damage detection process is then further explored using a mixture of electrochemistry and atomic force microscopy. DNA-modified electrodes were utilized to generate repair proteins with [4Fe4S] clusters in the 2+ and 3+ states by bulk electrolysis under an O_2-free atmosphere. Anaerobic microscale thermophoresis results indicate that proteins carrying $[4Fe4S]^{3+}$ clusters bind to DNA 550 times more tightly than those with $[4Fe4S]^{2+}$ clusters. The measured increase in DNA-binding affinity matches the calculated affinity change associated with the redox potential shift observed for [4Fe4S] cluster proteins upon binding to DNA. An electrostatic model was developed that shows this change in DNA-binding affinity of these proteins can be fully explained by the differences in electrostatic interactions between DNA and the [4Fe4S] cluster in the reduced versus oxidized state. Atomic force microscopy demonstrates that the redox state of the [4Fe4S] clusters regulates the ability of two DNA repair proteins, Endonuclease III and DinG, to bind preferentially to DNA duplexes containing a single base mismatch which inhibits DNA charge transport. Together, these results show that the reduction and oxidation of [4Fe4S] clusters through DNA-mediated charge transport facilitates long-range signaling between [4Fe4S] repair proteins. The redox-modulated change in DNA-binding affinity regulates the ability of [4Fe4S] repair proteins to collaborate in the lesion detection process.

Published Content and Contributions

Grodick, M.A.; Segal, H.M.; Zwang, T.J.; and Barton, J.K. *J. Am. Chem. Soc.* **2014**, *136* (17), 6470-6478
DOI: 10.1021/ja501973c
T.J. Zwang performed atomic force microscopy experiments, modeling, and analysis.

Zwang, T.J., Hurlimann, S., Hill, M.G., and Barton, J.K. *J. Am. Chem. Soc.*, **2016**, *138* (48), 15551-15554
DOI: 10.1021/jacs.6b10538
T.J. Zwang was the primary author on the manuscript, prepared and characterized DNA, assembled DNA-modified electrodes, and performed electrochemistry experiments.

Table of Contents

List of Figures

Chapter 1

Chapter 2

Chapter 3

Chapter 4

Chapter 5

List of Tables

Chapter 1

Chapter 2

Chapter 4

Chapter 5

Chapter 1

The Importance of DNA Structure for Charge Transport

Introduction

DNA-mediated charge transport (CT) is fascinating chemistry that relies on the π-stacked structure present in some DNA conformations. Under the right conditions DNA CT can occur over extraordinarily long distances with shallow distance dependence. Many characteristics of DNA CT are strongly dependent on the structure and dynamics of the DNA that is used as well as the assembly that is used to initiate and measure DNA CT. Understanding the role that all of these components play is essential to developing DNA CT for use in nanoelectronics or characterizing DNA CT's role in biological systems.

This thesis encompasses work that first aims to understand how DNA duplex structure informs characteristics of DNA CT and then continues to develop an understanding of the role these structural features play in biological systems. To contextualize these advancements, this first chapter outlines foundational work that has shown ways that DNA structure influences its ability to conduct charge. Specific focus is given to macromolecular structure and its associated characteristics that can vary with sequence or by exposing DNA to different environments. Additionally, the local structural changes, including those induced by mismatches, abasic sites, and lesions, are discussed.

Complexities of DNA Structure

The structure of deoxyribonucleic acid (DNA) is best described by considering the many pieces that can fit together in different ways. The basic building block of DNA are nucleotides, which consist of three molecular pieces: a sugar, a heterocyclic base, and a phosphate. The sugar, deoxyribose (or ribose in RNA), is cyclic and connected via a β-glycosyl linkage to a heterocyclic base. Though many natural and unnatural modifications are possible, typical DNA will have access to four different bases: adenine, guanine, cytosine, and thymine. Either the 3’- or 5’- hydroxyl group of the sugar is phosphorylated, which can then form phosphodiester bonds to link with adjacent nucleotides to become an oligonucleotide. (1)

In most of the known oligonucleotide crystal structures two complementary strands are observed associating in double-helical arrangements termed DNA duplexes. In a well-matched duplex complementary bases, one from each strand, hydrogen bond with one another to form adenine-thymine (AT) or guanine-cytosine (GC) pairs. Perpendicular to each pairing are adjacent nucleotides whose heterocycles’ π-orbitals overlap, creating a path for charge to transport down the helical axis.

Sometimes oligonucleotides can crystallize with other conformations; nonhelical entities are observed with looped configurations. (1) The different crystal structures indicate the conformational flexibility that is afforded to DNA which, despite being most often considered as a B-form, right-handed helix, allows for many relevant polymorphisms. Depending on the nucleotide sequence, modifications, and its exposure to different environments, DNA can adopt A, B, C, D, and Z duplexes among other forms. (1-6) Some of the structural parameters of different DNA duplexes are outlined in table 1.1.

Table 1.1. Duplex structure types and helical parameters of DNA observed by X-ray diffraction. Partially adapted from (1).

Structure Type	*Pitch (Å)*	*Helical Symmetry**	*Axial rise per nucleotide (Å)*	*Axial turn angle per nucleotide (degrees)*	*Minor groove width (Å)*	*Major groove width (Å)*	*Minor groove depth (Å)*	*Major groove depth (Å)*
A	28.2	11	2.56	32.7	11.0	2.7	2.8	13.5
B	33.8	10	3.38	36.0	5.7	11.7	7.5	8.5
C	31	9.33	3.32	38.6	4.8	10.5	7.9	7.5
D	24.3	8	3.04	45	1.3	8.9	6.7	5.8
Z	45	6**	3.7	-30.0	8.8	2.0	3.7	13.8

*number of residues per one turn after which repeat structure is observed

**for dinucleotide as repeating unit

Measurements of DNA-mediated charge transport

There are many different techniques that have been used to measure DNA-mediated charge transport. The majority of experiments testing DNA CT have been performed in solution and tend to involve a photoexcited charge donor that transfers charge to an acceptor through a DNA bridge. (7) A wide variety of donors and acceptors have been used, ranging from transition metal complexes to purely organic molecules, base analogs, and proteins. (8, 9, 10) Experiments have been conducted on electrodes, typically gold or graphite, that are covered by a self-assembled monolayer of DNA. (11,12) DNA duplexes are linked to the surface by a covalent modification on the phosphate backbone (thiols for gold or pyrene for graphite) that allows for them to stand upright. Redox molecules, either noncovalently or covalently attached to the DNA, can then be reduced or oxidized by applying a potential across the electrode surface. (13)

Other experimental setups have allowed for measurements of DNA conductivity. Conductive atomic force microscopy has been used to create metal-DNA-metal junctions that can be used as a circuit to measure the current-voltage characteristics of DNA. (14) Scanning tunneling microscopy break junction technique measures the conductivity as the tip is pushed towards and retracted away from the surface, apparently hybridizing and de-hybridizing the duplex. (15) The current is measured as a function of the distance of the tip from the surface with the assumption that the stretch of separation where the current is constant represents the conductivity of a DNA duplex bridge. Single DNA molecule circuits have also been made that tether DNA between a nanotube gap and measure the change in current that passes through the circuit. (16)

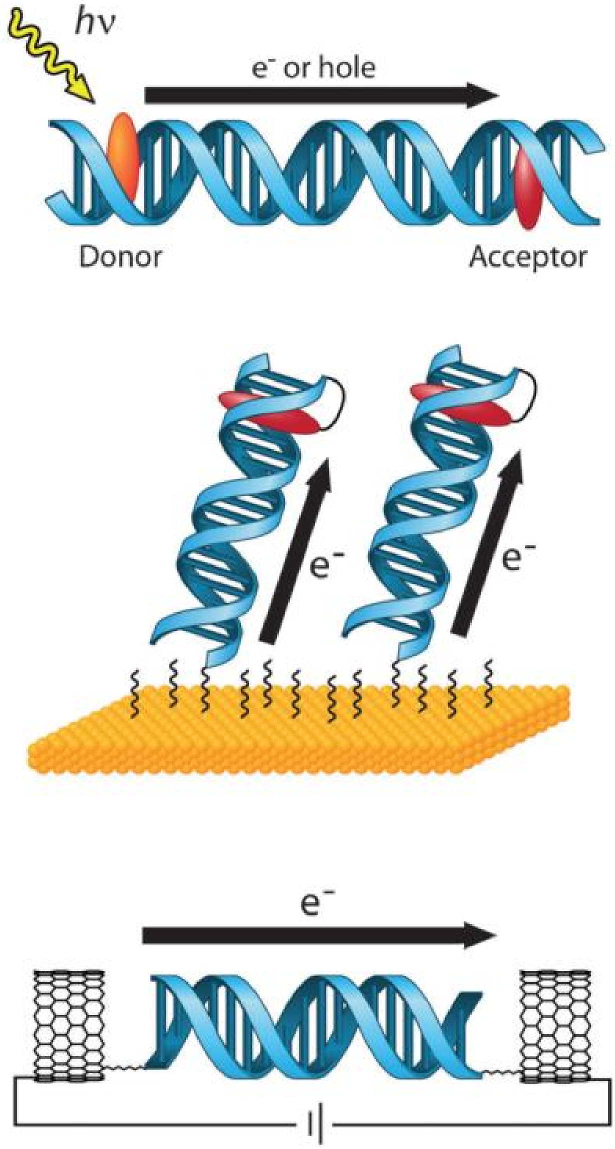

Figure 1.1 Platforms for the study of DNA CT. (Top) donor and acceptor molecules are incorporated into a DNA duplex. Photoexcitation initiates charge transported through the DNA bridge and is measured using spectroscopy or other means generally probing the donor or acceptor. (Middle) DNA is covalently tethered to an electrode surface with a redox active probe at the distal end away from the surface. A potential is applied that results in charge being transported through the DNA either to or from the electrode, which can be measured as a change in the current during a potential sweep. (Bottom) DNA is attached across a carbon nanotube gap to make a circuit which can probe fundamental questions of DNA conductivity. Reprinted with permission from *50*.

Structural features essential for DNA-mediated charge transport

The ability for DNA to mediate charge transport correlates with the extent of base stacking. The different base pair stacking of A-, B-, and Z-form DNA leads to different conductivities through these structures. (17) These duplex polymorphisms are illustrated in figure 1.2. The A-form duplex has the largest overlap of adjacent bases as well as the most efficient DNA CT. The B-form follows next, with the second best overlap. The Z-form is a significantly worse charge transport path than either of these, and also has the worst π-stacking of typical duplex structures. And single stranded DNA, if present in an unstacked conformation which does not have an ordered π-stacked structure, does not facilitate efficient charge transport. This has been confirmed with electrochemical, photooxidation, and direct conductivity studies. (16,17,18)

The sequence of DNA can have a significant role in the macromolecular structure that is being tested. The complementary pairings of $(dA\text{-}dT)_n$ with $(dA\text{-}dT)_n$ and $(dG\text{-}dC)_n$ with $(dG\text{-}dC)_n$ have the same purine-pyrimidine alternating sequence but they have access to different polymorphisms, with only the $(dG\text{-}dC)_n$ able to transition from B-form to Z-form under high salt conditions. (5,6) Even DNA with the same nucleotide composition in a different order can lead to significant changes in the accessible structures. Aqueous solutions of $(dG)_n$ with annealed with $(dC)_n$ results in A-form duplex but annealing $(dG\text{-}dC)_n$ with $(dG\text{-}dC)_n$ result in a B-form duplex. (20,21) Careful consideration of the annealing process should be taken when annealing different sequences of DNA, because the melting temperature of sequences will change as well as

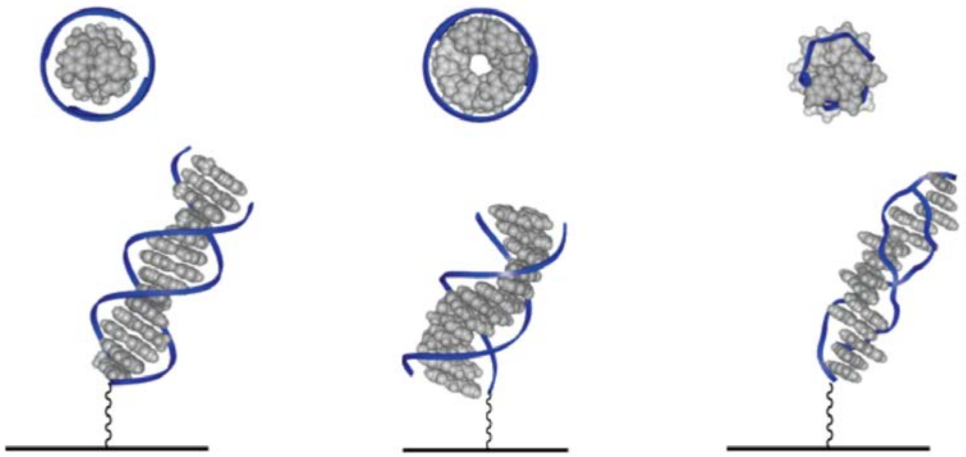

B-form DNA duplex

A-form DNA duplex:
DNA/RNA hybrid

Z-form DNA duplex:
5’-(^{m}CG)$_8$-3’

Figure 1.2. Illustration of A-, B-, and Z-form DNA duplexes tethered to electrode surfaces. Also shown are views looking directly towards the helical axis. Note the significantly different organization of nucleotides, which changes the overlap of π-orbitals from adjacent heterocycles. Reprinted with permission from *17*.

the favorability of non-duplex structures such as hairpins. To minimize structural differences caused by annealing, and to maximize the formation of duplex DNA, complementary DNA strands should be heated to well above the expected duplex melting temperature and then decreased slowly to a temperature where the duplex form is stable and other structures are not.

Disruption of the π-stacking will diminish the efficiency of DNA CT through that region. The presence of mismatches lowers the rate and yield of DNA CT in a way that correlates with base pair lifetime. (22) This disruption occurs even though mismatched base pairs do not cause major structural changes. (23) Abasic sites and destabilizing lesions, such as 8-oxoguanine, diminish DNA CT. (24,25) Significant kinks to DNA caused by protein binding, such as the TATA-binding protein, or chemical interactions with molecules such as cisplatin, will also disrupt DNA CT. (26,27)

Not all modifications to DNA structure diminish DNA CT. A dephosphorylation of the backbone does not have a measurable effect on yield or efficiency. (28,29). Some mismatches, such as G containing mismatches that are fairly stable, do not have a significant effect on DNA CT. (25) Some changes in structure, such as methylation to generate 5-methylcytosine, do not significantly influence DNA CT. (25)

The importance of the π-orbitals' overlap is also essential for charge to move to and from acceptor and donor molecules that are associated with a duplex. Intercalative redox probes such as methylene blue that are able to insert themselves into the π-orbital stack undergo efficient DNA-mediated charge transport. (30) Other molecules, like the positively charged ruthenium hexammine, associate electrostatically to the phosphate backbone and are unable to access DNA-mediated charge transport. (31) In some cases, like with methylene blue, different DNA binding modes are available. At low concentrations methylene blue primarily intercalates into DNA where it can undergo efficient DNA CT, but at higher concentrations it can bind electrostatically where it cannot utilize DNA CT. (30) Screening these electrostatic interactions with increased salt concentrations will promote primarily intercalative binding.

The DNA environment can change the duplex structure

DNA’s access to different conformations can be taken advantage of by experiments, but unknown conformational changes can also confound the interpretation of results. The ability for DNA to change between conformations with different charge transport properties makes structural confirmation of duplexes essential for comparisons to be made between measurements of DNA CT in different systems. Various measurements have been performed since the discovery that DNA conducted charge that have shown all sorts of conflicting properties. (32) In some cases, DNA is said to be insulating or nonconductive and in others it is said to be superconductive. DNA conductivity is reported to be dependent on the sequence, hydration, length, temperature, and hybridization in some experiments but not in others. These differences can be largely reconciled by assessing the preparation of samples and methodology used, because small changes in DNA’s handling can enhance, eliminate, or disrupt the internal π-stacked structure and have dramatic effects on its ability to conduct charge. (32)

Dehydration or exposure to nonaqueous solvents can eliminate efficient DNA-mediated charge transport. DNA is stabilized by a variety of hydrophobic and hydrophilic interactions; changing these interactions can significantly change the resulting structure. (1) The precise structural changes caused by dehydration or exposure to most nonaqueous solvents are not very well characterized, but it is clear that the equilibrium conformation of DNA is changed. (1,32,33) Many solvents that dissolve DNA do not retain the duplex structure and it is not clear that returning to an aqueous environment restores the duplex. (34) For example, drying duplex DNA then redissolving it in aqueous solution results in the generation of single stranded hairpin structures and other changes. (35) The influence of hydration is so important that changing the humidity of DNA can also significantly change the structure of DNA with the same sequence. Poly(dA-dT) duplexes exist exclusively in the B form above 70% relative humidity, but at lower humidity transform into a metastable A form which disproportionates into a triple-stranded complex with A-type conformation. (36) These data show that the dehydration or exposure to nonaqueous solvents can eliminate the π-stacked duplex structure, which is why they impede efficient DNA CT, but in most cases it is unclear what the structure of DNA actually is after exposure to nonaqueous conditions.

Some experiments conducted under nonaqueous conditions show efficient DNA CT or conductivity. Scanning tunneling microscope studies describing DNA conductivity are generally performed under vacuum to intentionally remove water that can make such experiments difficult, (37) though some scanning tunneling microscope studies have been conducted in humid environments with different results. (38) Other measurements, including many conductive atomic force microscopy experiments, have shown varying degrees of conductivity after rehydrating DNA that was deposited in vacuum or washed with apolar solvents. (32,39) Chemistry mediated by DNA CT in hydrated ionic liquids has also been reported with careful consideration of the influence this environment has on the duplex structure. (40) In these extreme conditions the structure of DNA is unclear so it is difficult to make claims regarding DNA-mediated charge transport that are clearly deconvolved from other aspects of the experiment. For example, ionic conduction through water may be what is measured instead of DNA-mediated CT. (32,41,32) So, to properly understand the structure that is being tested it is essential to keep DNA hydrated during all steps of preparation and experiment, characterize the DNA after procedures that may change the structure, and verify that the charge transport is DNA-mediated.

Verification of DNA-mediated charge transport

There are many different ways to verify that charge transport is DNA-mediated. Ideally, controls will disrupt DNA CT in a way that is recoverable or in a way that minimizes other differences in the experiment. The significant influence that small structural changes have on the yield of DNA CT allows for the design of experiments that can verify charge transport is mediated by the DNA. Larger scale structural changes such as dehybridization or melting of the duplex may provide necessary confirmation in some context. Careful use of multiple redox probes, including some that are able to undergo DNA CT and others that are unable to undergo DNA CT, can also be used to confirm a DNA-mediated signal.

One of the strongest confirmations that charge transport is DNA by the inclusion of a single base mismatch or abasic site that will disrupt the π-stacking, illustrated in figure 1.3. (32) The main benefit of this method is that it changes very little about the DNA structure that may influence other parts of the experiment, but should have a

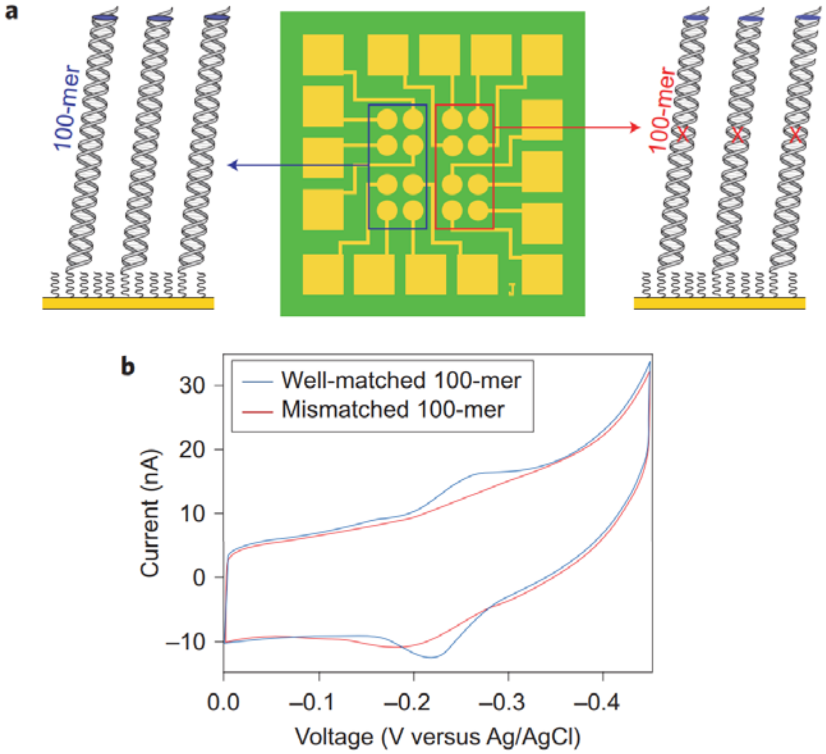

Figure 1.3 Electrochemistry of a 100 base pair duplex with and without a single base mismatch. **a**, The multiplexed electrode and layout of DNA-modified electrodes used to compare DNA duplex monolayers formed under similar conditions. The duplex with the mismatch only differs from the other duplex in that a C was substituted for a T to generate a CA mismatch 69 bases from the electrode surface. **b**, Each duplex was modified with a Nile Blue redox probe that showed greatly diminished charge transport yield for the duplex containing the CA mismatch. Reprinted with permission from *48*.

dramatic effect on charge transport that is mediated by the π-stack of the duplex. Incorporation of a particularly ruinous mismatch, such as CC or CA, will result in a significant decrease in the yield of DNA CT. (25) G-containing mismatches tend to be poor choices for this confirmation because they don't have attenuate CT as dramatically. (25) An abasic site will have a more significant effect, but it is also a larger structural change. If the experiments are run at relatively high temperatures an abasic site is a better choice than a mismatch, because increasing the temperature decreases the attenuation caused by a mismatch and potentiates the attenuation caused by an abasic site. (43,44)

In hydrated experiments it is possible to take advantage of more dramatic structural changes to verify that charge transport is DNA-mediated. Enzymatic cleavage by proteins can be used to release a region of DNA with a bound redox reporter, effectively eliminating the DNA-mediated path. (45) Protein binding to their specific binding substrate, whether it is a particular sequence or structure (such as single stranded regions, overhangs, etc.), can also be used to verify the structure. (46) Solution conditions can be used to induce changes, such as switching from B-to-Z form DNA, that will reversibly change the charge transport properties. (47) It may also be useful to dehybridize duplexes in solution followed by rehybridizing DNA with or without lesions (16).

Careful selection of redox active molecules can also be used to confirm DNA-mediated charge transport. DNA-mediated charge transport will only occur efficiently with redox active molecules that couple to the π-stack. Probing the same DNA construct with molecules that do and do not couple to the π-stack should show a significant difference in yield, if the charge transport is DNA-mediated. (47) Using covalently tethered probes can also allow for specific selection of a region that the redox probe is attached to, which can then be removed through enzymatic digestion. (48) It is also possible to use redox probes that selectively target mismatches or abasic sites, which should only show a DNA-mediated signal if that mismatch or abasic site is present in a duplex form. (49)

It is more complicated to verify charge transport is mediated by the DNA π-stack in dried samples and DNA in other conditions that do not have known structures. Ideally the use of sequences that vary by containing a mismatch can be used to see whether the measured conduction is only caused by charge transport mediated by the π-stack. The access to conformational changes is severely limited, and it is unclear what structures are often tested, which makes data measuring charge transport through dried samples susceptible to misinterpretation.

Summary

DNA-mediated charge transport is fascinating chemistry that relies on the π-stacked structure present in some DNA conformations. Disrupting the π-stack inhibits efficient charge transport. Thus, it is important that measurements of DNA CT have an understanding of the DNA structures that are being measured. Making small changes to the structure of a DNA duplex can have dramatic inhibition of CT yield. Thus, experiments that measure DNA CT must pay careful attention to the structure, keep DNA hydrated during all steps of preparation and experiment, characterize the DNA after procedures that may change the structure, and verify that the charge transport is DNA-mediated.

References

1) W. Saenger, *Principles of nucleic acid structure.*, Springer-Verlag, New York, **1984**
2) W. Fuller, M.H.F. Wilkins, H.R. Wilson, and L.D. Hamilton, *J. Mol. Biol*, **1965**, *12*, 60-80
3) R. Langridge, D.A. Marvin, W.E. Seeds, H.R. Wilson, C.W. Hooper, M.H.F. Wilkins, and L.D. Hamilton, *J. Mol. Biol.* **1960**, *2,* 38-64
4) D.A. Marvin, M. Spencer, M.H.F. Wilkins, and L.D. Hamilton, *J. Mol. Biol.* **1961**, *3*, 547-565
5) S. Arnott, R. Chandrasekaran, D.L. Birdsall, A.G.W. Leslie, and R.L. Ratcliff, *Nature,* **1980**, *283*, 743-745
6) S. Arnott, R. Chandrasekaran, D.W.L. Hukins, P.J.C. Smith, and L. Watts, *J. Mol. Biol.* **1974**, *88*, 523-533
7) S.O. Kelley, J.K. Barton, *Science* **1999**, *283*, 375
8) L. Valis, Q. Wang, M. Raytchev, I Buchvarov, H.-A. Wagenknecht, T. Fiebig, *Proc. Natl. Acad. Sci. U.S.A.* **2006**, *103*, 10192
9) S. Delaney, M. Pascaly, P.K. Bhattacharya, K. Han, J.K. Barton, *Inorg. Chem.* **2002**, *41*, 1966
10) E. Boon, N. M. Jackson, M.D. Wrightman, S.O. Kelley M.G. Hill, J.K. Barton, *J. Phys. Chem. B* **2003**, *107*, 11805

11) A.A. Gorodetsky, J.K. Barton, *Langmuir*, **2006**, *22*, 7917-7922

12) J.D. Slinker, N.B. Muren, A.A. Gorodetsky, and J.K. Barton, *J. Am. Chem. Soc.* **2010**, *132*, 2769-2774

13) C.G. Pheeney, J.K. Barton, *J. Am. Chem. Soc.* **2013**, *135*, 14944

14) Z. Xie, T.Z. Markus, S.R. Cohen, Z. Vager, R. Gutierrez, R. Naaman, *Nano. Lett.* **2011**, *11*, 4652-5644

15) N. Kang, A. Erbe, E. Scheer *New J. Phys.* **2008**, *10*, 023030

16) X. Guo, A.A. Gorodetsky, J. Hone, J.K. Barton, and C. Nuckolls, *Nat. Nanotech.* **2008**, *3*, 163-167

17) E.M. Boon, and J.K. Barton, *Bioconjugate Chem.* **2003**, *14*, 1140-1147

18) M.A. O'Neill, H.C. Becker, C. Wan, J.K. Baron, A.H. Zewail, *Angew. Chem. Int. Ed.* **2003**, *42*, 5896

19) E.M. Boon, D.M. Ceres, T.G. Drummond, M.G. Hill, J.K. Barton, *Nat. Biotechnol.* **2000**, *18*, 1096

20) A.G.W. Leslie, S. Arnott, R. Chandrasekaran, and R. L.Ratlif, *J. Mol. Biol.* **1980**, *143*, 49-72

21) S. Arnott, E. Selsing, *J. Mol. Biol.* **1974**, *88*, 551-552

22) P.K. Bhattacharya, J. Cha, J.K. Barton *Nucl. Acids. Res.* **2002**, *30*, 4740

23) W.N. Hunter, T. Brown, O. Kennard, *Nucl. Acids. Res.* **1987**, *15*, 6589

24) M.C. Buzzeo, J.K. Barton, *Bioconjugate Chem.* **2008**, *19*, 2110

25) A.K. Boal, J.K. Barton, *Bioconjugate Chem.* **2005**, *16*, 312

26) E.M. Boon, J.E. Salas, J.K. Barton, *Nat. Biotechnol.* **2002**, *20*, 282

27) A.A. Gorodetsky, A. Ebrahim, J.K. Barton, *J. Am. Chem. Soc.* **2008**, *130*, 2924

28) T. Liu, J.K. Barton, *J. Am. Chem. Soc.* **2005**, *127*, 10160

29) Y. Osakada, K. Kawai, M. Fujitsuka, T. Majima, *Chem. Commun.* **2008**, *23*, 2656

30) E.M. Boon, N.M. Jackson, M.D. Wrightman, S.O. Kelley, M.G. Hill, J.K. Barton, *J. Phys. Chem. B* **2003**, *107*, 11805

31) H.-Z. Yu, C.-Y. Luo, C.G. Sankar, D. Sen, *Anal. Chem.* **2003**, *75*, 3902

32) J.G. Genereux, J.K. Barton *Chem. Rev.* **2010**, *110*, 1642-1662

33) C.R. Calladine, H.R. Drew, B.F. Luisi, A.A. Travers, *Understanding DNA: The Molecule and How It Works*, **2004**, Elsevier Academic Press: San Diego

34) G. Bonner, A.M. Klibanov, *Biotech. Bioeng.* **2000**, *68*, 339-344

35) J. Svaren, S. Inagami, E. Lovegren, R. Chalkley, *Nucl. Acid. Res.* **1987**, *15*, 8379-8754

36) S. Arnott, E. Selsing, *J. Mol. Biol.* **1974**, *88*, 509-521

37) M.S. Xu, S. Tsukamoto, S. Ishida, M. Kimatura, Y. Arakawa, R.G. Endres, M. Shimoda *Appl. Phys. Lett.* **2005**, *87*, 083902

38) I. Kratochvilova, K. Kral, M. Buncek, A. Viskova, S. Nespurek, A. Kochalska, T. Todorciuc, M. Weiter, B. Schneider, *Biophys. Chem.* **2008**, *138*, 3-10

39) Z. Xie, T.Z. Markus, S.R. Cohen, Z. Vager, R. Gutierrez, R. Naaman, *Nano Lett.* **2011**, *11*, 4652

40) S. Xuan, Z. Meng, X. Wu, J.-R. Wong, G. Devi, E.K.L. Yeow, F. Shao *ACS Sustainable Chem. Eng.* **2016**, *4*, 6703-6711

41) H.W. Fink, C. Schoenberger, *Nature*, **1999**, *398*, 407

42) K.-H. Yoo, D.H. Ha, J.-O. Lee, J.W. Park, J. Kim, J.J. Kim, H.-Y. Lee, T. Kawaii, H.Y. Choi, *Phys. Rev. Lett.* **2011**, *87*, 198102

43) C.H. Wohlgamuth, M.W. McWilliams, and J.D. Slinker *Anal. Chem.* **2013**, *85*, 1462

44) M.A. McWilliams, R. Bhui, D.W. Taylor, J.D. Slinker *J. Am Chem .Soc.* **2015**, *137*, 11150

45) J.D. Slinker, N.B. Muren, S.E. Renfrew, J.K. Barton, *Nature Chem.* **2011**, *3*, 228

46) M.A. Grodick, H.M. Segal, T.J. Zwang, J.K. Barton, *J. Am. Chem. Soc.* **2014**, *136*, 6470-6478

47) T.J. Zwang, S. Hurlimann, M.G. Hill, J.K. Barton, *J. Am. Chem. Soc.* **2016**, *138*, 15551-15554

48) J.D. Slinker, N.B. Muren, S.E. Renfrew, J.K. Barton, *Nature Chem.* **2011**, *3*, 228

49) J.M. Abendroth, N. Nakatsuka, M. Ye, D. Kim, E. Fullerton, A.M. Andrews, P.S. Weiss, *ACS Nano* **2017** *Just accepted* DOI: 10.1021/acsnano.7b04165

50) N.B. Muren, E.D. Olmon, J.K. Barton, *Phys. Chem. Chem. Phys.* **2012**, *14*, 13754-13771

Chapter 2

Helix-Dependent Spin Filtering through the DNA Duplex

Adapted from Zwang, T.J., Hurlimann, S., Hill, M.G., and Barton, J.K. *J. Am. Chem. Soc.*, **2016**, *138* (48), 15551-15554

T.J. Zwang prepared and characterized DNA, assembled electrodes, and performed electrochemistry experiments. S. Hurlimann assisted with electrochemistry experiments.

Introduction

DNA-mediated charge transport (DNA CT) is well established in both ground and excited state systems (1). Although theoretical models are still being developed, it is clear that the integrity of the extended π-stack of the aromatic heterocycles, the nucleic acid bases, plays a critical role:(2-4) electron donors and acceptors must be electronically well coupled into the π-stack, typically via intercalation, and perturbations that distort the π-stack, such as single-base mismatches, abasic sites, base lesions, and protein binding that kinks the double helix, attenuate DNA CT dramatically. This latter characteristic has found practical use in electronic devices and biosensors (5-7).

Recent experimental work in the field of spintronics has raised the intriguing possibility that DNA CT is affected by the inherent spin of the electrons passing through it. The first experiments to show that double stranded DNA (dsDNA) could function as a spin filter were conducted under vacuum, where photoelectrons ejected from a gold surface became spin-polarized after passing through an adsorbed dsDNA monolayer (8). Subsequent conductive AFM measurements showed that the resistance of spin-polarized currents traveling through a thin film of air-dry dsDNA depended on the ratio of spin up versus spin down electrons injected into the film (9). These observations mirror similar experiments that feature other chiral organic molecules within a thin film (10). Because organic molecules display small spin–orbit coupling that would otherwise preclude them from exhibiting spin-selective transport properties, this work has spawned much interest in chirality-induced spin selectivity (CISS) (11-13). Several theories have been offered to account for this effect (14-17). One question of particular interest is whether CISS depends more on the isolated molecular chiral centers or the large-scale macromolecular structures within the films (15).

Owing to its ability to undergo macromolecular conformational changes that affect the helical structure but not the local chirality of the sugar backbone, dsDNA in its native, hydrated state presents a unique opportunity to differentiate between the monomeric and macromolecular parameters of CISS. Of particular interest is the conformational switching between right-handed B-DNA and left-handed Z-DNA. At high salt concentrations, CG-repeat sequences in the right-handed B-form can flip into a left-handed zigzag Z-form helix (18). Notably, both B-DNA and Z-DNA support efficient DNA CT (19).

We have developed an electrochemical assay to investigate dsDNA-promoted CISS under fluid conditions. Following work by others (20), our study employs a nickel working electrode capped with a thin (~10 nm) layer of gold (21). Thiol-modified DNA duplexes are then self-assembled onto these electrodes, and DNA-binding redox-active probes are added to the electrolyte solution. Magnetizing the nickel surface with a permanent neodymium magnet (0.66 T) generates a spin-polarized current when the potential is poised negative of the formal reduction potential of the DNA-bound probe molecules. The sign of the polarization can be switched by changing the direction of the magnetic field, but its magnitude remains the same. Integrating the Faradaic response of probe-molecule reduction using cyclic voltammetry gives the total number of redox probes reduced, which can be used to quantify the yield of DNA CT under different experimental conditions. Importantly, the redox potentials of all of the probes lie well negative of the potential of zero charge of the working electrode (22). As a result, duplexes within the DNA film line up approximately normal to the gold surface with the magnetic field lines essentially collinear with the helical axes.

Materials and Methods

DNA Synthesis and purification. All materials for DNA synthesis were purchased from Glen Research. Oligonucleotides were synthesized on an Applied Biosystems 3400 DNA synthesizer using phosphoramidite chemistry on a controlled-pore glass support. The two strands of a duplex were synthesized separately, purified, stored frozen, and then annealed prior to electrochemical experiments. The 5’- end of one strand was modified with a C6 S-S phosphoramidite that is later reduced before use. The 5’- end of the complementary strand is either unmodified or modified with an NHS-Carboxy-dT phosphoramidite for later coupling with Nile blue. High performance liquid chromatography (HPLC) was performed using a reverse-phase PLRP-S column (Agilent) using a gradient of acetonitrile and 50 mM ammonium acetate (5-35% acetonitrile over 30 minutes).

Unmodified DNA. DNA was synthesized using standard phosphoramidites (dA-CE, dT-CE, dC-CE, dG-CE) starting from phosphoramidites attached to a solid support (3’-dA-CPG, 3’-dT-CPG, 3’-dC-CPG, 3’-dG-CPG). After synthesis, the DNA was lyophilized overnight. It was then cleaved from the solid support by incubation at 60^{o} C with concentrated (28-30%) NH_4OH for 12 hours, filtered using CoStar columns, and then dried. The dried DNA film was resuspended in phosphate buffer (5 mM phosphate, pH 7, 50 mM NaCl) and HPLC-purified. The DMT (4,4'-dimethoxytrityl) group protecting the 5'- end was then removed by incubation with 80% acetic acid for 45 minutes. The reaction mixture was dried and resuspended in phosphate buffer. The DNA was isolated using HPLC. The purified oligonucleotide was desalted using ethanol precipitation, dried, and the mass confirmed with Matrix-assisted laser desorption/ionization- time of flight mass spectrometry (MALDI-TOF). Unmodified oligonucleotides were then stored at -20^{o}C in phosphate buffer until annealing with their complementary strand.

Thiolated DNA. DNA was synthesized using standard phosphoramidites (dA-CE, dT-CE, dC-CE, dG-CE) and reagents, with the exception of a C6 S-S phosphoramidite that was attached to the 5'- end. After synthesis, the DNA was lyophilized overnight. It was then cleaved from the solid support by incubation at 60^{o} C with concentrated (28-30%) NH_4OH for 12 hours, filtered using CoStar columns, then dried. The dried DNA film was resuspended in phosphate buffer (5 mM phosphate, pH 7, 50 mM NaCl) and HPLC-purified. The DMT (4,4'-dimethoxytrityl) group protecting the 5'- end was then removed by incubation with 80% acetic acid for 45 minutes. The reaction mixture was dried and resuspended in phosphate buffer. The DNA was isolated using HPLC. The purified oligonuceotide was desalted using ethanol precipitation, dried, and the mass was confirmed with Matrix-assisted laser desorption/ionization- time of flight mass spectrometry (MALDI-TOF). Within one week of annealing, the dithiolated DNA was reduced by resuspending in 50 mM Tris-HCl, pH 8.4, 50 mM NaCl, 100 mM dithiothreitol (Sigma) for 2 hours. The reduced thiol-modified DNA was then purified by size exclusion chromatography (Nap5 Sephadex, G-25, GE Healthcare) with phosphate buffer as the eluent and subsequently purified using HPLC.

Covalent Coupling of Nile Blue to DNA. DNA was synthesized using ultramild procedures from Glen Research, which mainly involve using different phosphoramidites, Cap A, and bead cleavage reagents to prevent degradation of the NHS-Deoxy-dT phosphoramidite (24). Phophoramidites compatible with ultramild synthesis (dT-CE, Pac-dA-CE, Ac-dC-CE, and iPr-Pac-dG-CE phosphoramidites) were used as well as ultramild Cap A (5% phenoxyacetic anhydride in THF/Pyridine). An NHS-Deoxy-dT phosphoramidite was attached to the 5'- end. After synthesis, the DNA was dried overnight in a lyophilizer. Nile blue perchlorate (Sigma) was then dissolved (15 mg/ml) in anhydrous N,N-dimethylformamide and activated with 10% v/v DIEA (N,N-Diisopropylethylamine). This Nile blue solution was then incubated with the DNA overnight with gentle shaking. At least 18 hours later, the DNA solid support beads were rinsed with N,N-dimethylformamide and then dichloromethane. The DNA was then cleaved from the solid support by incubating with 0.05 M potassium carbonate in methanol for 4 hours at ambient temperature. The DNA was then dried, resuspended in phosphate buffer, and the oligonucleotide isolated with HPLC. The purified oligonucleotide was desalted using ethanol precipitation, dried, and the mass confirmed with MALDI-TOF. Nile blue-modified strands were then stored in the dark at -20^{o}C in phosphate buffer until annealing with their complementary strand.

Synthesis of 3’-Dabcyl-DNA. DNA was synthesized using standard phosphoramidites and reagents, with the exception of 3’-Dabcyl modified controlled pore glass (CPG) beads. After synthesis, the DNA was lyophilized overnight. It was then cleaved from the solid support by incubation at ambient temperature with concentrated (28-30%) NH_4OH for 2 hours, spin filtered to remove the solid support beads, and then dried. The oligonucleotide was resuspended in phosphate buffer and HPLC-purified. The DMT (4,4’-dimethoxytrityl) group protecting the 5’- end was then removed by incubation with 80% acetic acid for 45 minutes, dried, resuspended in phosphate buffer, and re-purified using HPLC. The purified strand was desalted using ethanol precipitation, dried, and the mass was confirmed with MALDI-TOF.

Annealing Duplex DNA. Duplex DNA for electrochemistry was prepared by first quantifying the complementary strands with UV-Visible spectroscopy, and then mixing equimolar (50 μM) complementary strands in 200 μl phosphate buffer. The DNA solution was then deoxygenated by bubbling argon for at least 5 minutes per ml. Duplex DNA was then annealed on a thermocycler (Beckman Instruments) by initial heating to 90^{o}C followed by slow cooling over 90 minutes.

DNA Sequences:

CG-repeat
3’-GCG CGC GCG CGC GCG C-5’
HS-C_6- 5’-CGC GCG CGC GCG CGC G-3’

C^mG-repeat
3’-GC^mG C^mGC^m GC^mG C^mGC^m GC^mG C^m
HS-C_6- 5’-C^mGC^m GC^mG C^mGC^m GC^mG C^mGC^m G-3’

16bp DNA
3’- TGC AGA GTT GAG TGC A-5’
HS-C_6- 5’-ACG TCT CAA CTC ACG T-3’

30bp DNA (well-matched)
3’-AGA GTT CTT AGC CGT AAT CGA GTT GAC AGT-5’
HS- C_6- 5’- TCT CAA GAA TCG GCA TTA GCT CAA CTG TCA-3’

30bp DNA (C:A mismatch)
3’-AGA GTC CTT AGC CGT AAT CGA GTT GAC AGT-5’
HS- C_6- 5’- TCT CAA GAA TCG GCA TTA GCT CAA CTG TCA-3’

17 bp NB (Well matched)
3’-CGA GTC ATG CTG CAG CT-5’-NB
HS-C_6-5’-GCT CAG TAC GAC GTC GA-3’

17 bp NB (C:A mismatch)
3’-CGA GTC ATG CTG CAG CT-5’-NB
HS-C_6-5’-GCT CAA TAC GAC GTC GA-3’

29 bp NB
3’-CAC CGT CCA GTC AGT ACA TAT GAC GTG AT-5’-NB
HS-C_6-5’-GTG GCA GGT CAG TCA TGT ATA CTG CAC TA-3’

43 bp NB
3’-CGT CAT CCA CTT AGC ACC GTC CAG TCA GTA CAT ATG ACT TGA T-5’-NB
HS-C_6-5’-GCA GTA GGT GAA TCG TGG CAG GTC AGT CAT GTA TAC TGA ACT A-3’

60 bp NB
3’-CAA GTA CTG TAT GCA TGC GTC ATC CAC TTA GCA CCG TCC AGT CAG TAC ATA TGA CTT GAT-5’-NB
HS-C_6-5’-GTT CAT GAC ATA CGT ACG CAG TAG GTG AAT CGT GGC AGG TCA GTC ATG TAT ACT GAA CTA-3’

29 bp Dabcyl
DAB-3’-CAC CGT CCA GTC AGT ACA TAT GAC GTG AT-5’
HS-C_6-5’-GTG GCA GGT CAG TCA TGT ATA CTG CAC TA-3’

The above sequences use the following abbreviations for modifications:
DAB = Dabcyl; NB = Nile Blue; HS-C_6 = hexanethiol linker; C^m = 5-methyl-cytosine

Electrode Fabrication

Single electrode surface fabrication was carried out at UCLA and received as a gift from Paul Weiss and John Abendroth following the general protocol of R. Naaman *et al* (20). P-type oxidized silicon wafers were coated with 25 nm titanium as an adhesive layer, following deposition with 200 nm nickel then 10 nm gold. The surfaces were then cleaved into 1 cm x 1.5 cm rectangles and used following the preparation below (for a total 1 cm^2 exposed surface area for experiments following device assembly).

Multiplexed electrode surfaces were fabricated following a modified version of a published protocol (24) using the gold-capped nickel as the electrode material. In brief, one millimeter thick Si wafers with a 10 000 Å thick oxide layer were purchased from Silicon Quest. First, wafers were cleaned thoroughly in 1165 Remover (Microchem) and vapor primed with hexamethyldisilizane (HMDS). SPR 220 3.0 photoresist (Microchem) was spin-cast at 4000 rpm and baked. The photoresist was patterned with a Karl Suss MA6 contact aligner and a chrome photomask. Following postexposure baking, wafers were developed in AZ 300 MIF developer for 1 min and rinsed thoroughly with deionized water. A 15 Å Ti adhesion layer, a 1000 Å Ni layer, and a 100 Å Au layer were deposited on the chips with a CHA Mark 50 electron beam evaporator. Wafers were then immersed in 1165 Remover overnight and sonicated as needed to complete metal lift-off. Subsequently, the wafers were thoroughly baked and cleaned by UV ozone treatment. SU-8 2002 (Microchem) was spin-cast at 3000 rpm, baked, and photopatterned as above. Wafers were developed in SU-8 Developer (Microchem) for 1 min and baked for a permanent set of the photoresist. The wafers were subsequently diced into 1-in. by 1-in. chips and used for electrochemistry experiments.

DNA-modified electrode preparation

Gold-capped nickel surfaces or multiplexed chips are gently cleaned by rinsing with ultrapure water, acetone, isopropanol, and finally a second rinse with ultrapure water before drying with argon. They are then cleaned with a UVO Cleaner Model 42 (Jelight Co.) for 20 minutes. Immediately after cleaning the surface, a plastic clamp and rubber (BunaN) gasket were affixed to the surface to create a well for liquid and either 50 μM duplex DNA, single stranded DNA, or no DNA in phosphate buffer (pH 7, 5 mM phosphate, 50 mM NaCl, 100 mM $MgCl_2$) to make densely packed films. The DNA was incubated on the surface for 18-24 hours. Once the DNA is on the surface, it cannot be dried without compromising the structure and therefore the measured properties of the film. The solution was then exchanged 5x with 1 μM mercaptohexanol in phosphate buffer (pH 7, 5 mM phosphate, 50 mM NaCl, 5% glycerol) and incubated for 45 minutes. Lastly the surface was rinsed at least 5x with either phosphate buffer (pH 7, 5 mM phosphate, 50 mM NaCl) for most experiments or tris buffer (pH 7.6, 10 mM Tris, 100 mM KCl, 2.5 mM $MgCl_2$, 1 mM $CaCl_2$) for experiments using dabcyl, and electrochemical experiments were performed immediately afterwards.

Electrochemical measurements

The central well around the electrode surface created by the clamp was filled with one of three buffers prior to electrochemical measurements: a phosphate buffer with $MgCl_2$ (pH 7, 5 mM phosphate, 50 mM NaCl, 10 mM $MgCl_2$), a phosphate buffer without $MgCl_2$ (pH 7, 5 mM phosphate, 50 mM NaCl), and a tris buffer (pH 7.6, 10 mM Tris, 100 mM KCl, 2.5 mM $MgCl_2$, 1 mM $CaCl_2$). The phosphate buffer was used for all experiments, except those containing dabcyl. The phosphate buffer without $MgCl_2$ was only used to collect data with experiments comparing methylated and unmethylated dsDNA. The tris buffer is necessary for both the reduction and oxidation of dabcyl to occur within the potential range that we can scan. Our experiments did not show a statistically significant difference in the magnitude of spin selectivity when comparing DNA sequences of the same length in the different buffers, except in the cases where the increased ionic strength helped prevent electrostatic binding of MB to the phosphate backbone. An AgCl/Ag reference electrode (Cypress) was coated with a solidified mixture of 1% agarose and 3M NaCl in water inside a long, thin pipette tip. The tip was cut so that the salt bridge could connect the electrode to the buffer from the top of the well. A platinum wire used as an auxiliary electrode was also submerged in the buffer from the top of the well. The working electrode contacted a dry part of unmodified gold surface. A grounding wire was connected to the metallic base of a ring stand. A CH1620D Electrochemical Analyzer (CH Instruments) was used to control the electrochemical experiments.

Magnetic field experiments were conducted using a 6619 Guass surface strength magnetic field neodymium magnet (K&J Magnetics). Alligator clips were replaced with nonmagnetic stainless steel to minimize magnetic interference. All other parts of the assembly were created using plastic to prevent extraneous objects the magnetic field could influence. Additionally, the strong magnet was waved near the potentiostat during operation, with no obvious change in signal that was apparent, to ensure that the magnet was not interfering with the operation of the potentiostat. Each experiment that was conducted for magnetic field pointing up vs down were done by comparing the same surface in the same solution under these varying field directions in order to minimize variability caused by other factors.

Noncovalent Methylene Blue. Solutions of 1μM or 10μM methylene blue were made in phosphate buffer (pH 7, 5 mM phosphate, 50 mM NaCl, 10 mM $MgCl_2$). Cyclic voltammograms were collected using a scan rate of 0.1, 0.5, 1, 5, 10, and 20 V/s, which scanned from 0V to -0.55V (vs AgCl/Ag) then back to 0V at least 6 times consecutively for each experiment. The magnetic field direction was then switched, scanned, and switched again multiple times. The first reductive and oxidative sweeps were compared because subsequent scans see a diminishing effect. This attenuation is restored upon waiting for approximately 30 seconds between scans.

Ruthenium Hexammine. A concentration of 10 μM $Ru(NH_3)_6{}^{3+}$ was added to the phosphate buffer. Cyclic voltammograms were collected at a scan rate of 0.1 V/s, which scanned from 0V to -0.4V (vs AgCl/Ag) and then back to 0V at least 6 times consecutively for each experiment. The magnetic field direction was then switched, scanned, and switched again multiple times. The first reductive and oxidative sweeps were compared.

B-to-Z DNA Experiments. Experiments were conducted with solutions of 1 μM methylene blue in phosphate buffer with and without 10 mM $MgCl_2$. Cyclic voltammograms were collected at a scan rate of 0.1 V/s, which scanned from 0V to -0.4V (vs AgCl/Ag) then back to 0V at least 6 times consecutively for each experiment. The magnetic field direction was then switched, scanned, and switched again at least 4 times. Following these scans, phosphate buffer with 10 mM $MgCl_2$ was placed in the well by exchanging the solution 5 times. The surfaces were scanned in a similar manner as before, and then the solution was again exchanged 5 times to replace it with a phosphate buffer without magnesium. It was then scanned similarly.

Covalent Nile Blue. Experiments were conducted in phosphate buffer with 4 different lengths of DNA, each with Nile blue covalently tethered at the 5'- end away from the surface. Cyclic voltammograms were collected using a scan rate of 0.1, 0.5, 1, 5, 10, and 20 V/s, which scanned from 0V to -0.55V then back to 0V 20 times consecutively for each experiment. The magnetic field direction was then switched, scanned, and switched again multiple times. The first reductive and oxidative sweeps were compared.

3'-Dabcyl. Experiments were conducted in tris buffer (pH 7.6, 10 mM Tris, 100 mM KCl, 2.5 mM $MgCl_2$, 1 mM $CaCl_2$) with 1μM methylene blue. Due to the relatively slow rate of redox chemistry with azobenzene, cyclic voltammograms were collected using a scan rate of 10 mV/s so the peak splitting allowed for both the reductive and oxidative peaks to lie within the measurable potential range. The experiments scanned from 0V to -0.6V (vs AgCl/Ag) then to 0.5V and repeated scanning between 0.5V and -0.6V 20 times consecutively for each experiment. The magnetic field direction was then switched, scanned, and switched again multiple times. The first reductive and oxidative sweeps were compared.

Calculating the surface concentration of DNA

Surface concentration of DNA was quantified based on the total area of the reductive signal generated from a cyclic voltammogram of electrostatic binding of $Ru(NH_3)_6{}^{3+}$ to the phosphate backbone of dsDNA. This was done under saturation conditions (10 µM $Ru(NH_3)_6{}^{3+}$). The following equation was used to relate the reductive signal (Q_{Ru}) to the surface concentration of DNA (Γ_{DNA}):

$$\Gamma_{DNA} = \frac{Q_{Ru}}{n\,F\,A}\,\frac{z}{m}\;N_A$$

In this equation, *A* is the electrode area in cm^2, *F* is the Faraday constant, *n* is the number of electrons per reduction event, *z* is the charge on the $Ru(NH_3)_6{}^{3+}$, and *m* is the number of base pairs in the duplex DNA. The surface concentration of dilute DNA films was 8±1 pm/cm^2 and dense DNA films was 40±3 pm/cm^2.

Circular Dichroism Spectroscopy

An Aviv 62A DS spectropolarimeter was used to collect circular dichroism (CD) spectra. Data were obtained from samples containing 3 μM d(^{m}CG)$_8$ or 3 μM d(CG)$_8$ dsDNA in phosphate buffer (5 mM phosphate, 50 mM NaCl, pH7) using a 1.0 mm path length cell (Figure 2.1). Scans were conducted with samples that were incubated in the presence or absence of 10 mM $MgCl_2$. Data presented in figures represent the average of three scans. The B-Z transformation is very clearly seen in the CD spectra of the methylated DNA. Upon addition of magnesium ion, there is a large decrease in magnitude of ellipticity at 254 nm and 293 nm with isochromism at 277 nm, which is characteristic of the B-Z transformation. The unmethylated DNA does not show any change in CD spectrum for conditions with and without magnesium ion, which confirms that it remains in the B-form.

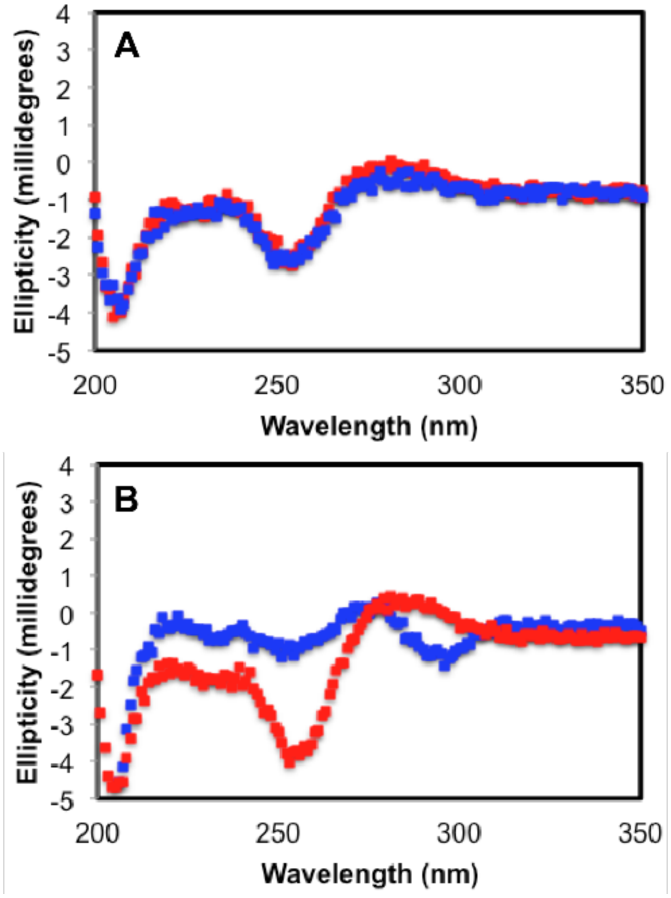

Figure 2.1 Circular dichroism spectra of d(CG)$_8$ DNA. [A] unmethylated d(CG)$_8$ and [B] methylated d(^{m}CG)$_8$ in phosphate buffer with [blue] and without [red] MgCl$_2$.

Spin Polarization Calculations

The spin polarization (S) is defined as:

$$S = \frac{I_+ - I_-}{I_+ + I_-} \tag{1.1}$$

in which I_+ and I_- are the intensities of the signals corresponding to the spin oriented parallel and antiparallel to the electrons' velocity (12). The spin polarization for electrons travelling *through* dsDNA is calculated assuming that the injected spin polarization is 23% which, using equation 1.1, results in the total amount of each spin injected assumed to be 0.615 and 0.385, with the majority spin depending on the magnetization direction (20). The amount of charge transferred to the probe (Q), which is determined by integrating the current under the reductive or oxidative peak in the cyclic voltammograms, can be related to the injected spin polarization by the following equation:

$$Q = I_+(\eta_+) + I_-(\eta_-) \tag{1.2}$$

where η_+ and η_- are the yield for the amount of injected spin oriented parallel and antiparallel, respectively, to the velocity of the electrons that reduce the probe compared to the total amount injected. Therefore the amount of probe reduced can be related as Q = 0.615 (Yield_{Up}) + 0.385 ($\text{Yield}_{\text{Down}}$) for one magnetization and Q = 0.615 ($\text{Yield}_{\text{Down}}$) + 0.385 ($\text{Yield}_{\text{Up}}$) for the other.

Modifying equation 1.1 to solve for the spin polarization through dsDNA gives equation 1.3.

$$S_{DNA} = \frac{\eta_+ - \eta_-}{\eta_+ + \eta_-} \tag{1.3}$$

Solving for η_+ and η_- and placing them into equation 1.3 gives the spin polarization of electrons moving through dsDNA (S_{DNA}).

Results

Figure 2.2 shows the results obtained at a densely packed dsDNA film (16 bp duplexes, ~40 pmol/cm^2) using methylene blue (MB) as the redox probe. We have previously shown that MB binds reversibly to DNA monolayers and undergoes a proton-coupled, DNA-mediated 2e$^-$reduction to leucomethylene blue (LB) at −220 mV versus AgCl/Ag.(23) As can be seen in Figure 2.2, the yield of MB undergoing electrochemical reduction varies regularly with the orientation of the underlying magnetic field, “up” versus “down”. The change in yield measured by cyclic voltammetry is not large, but it is highly reproducible. This effect is fully reversible and can be switched repeatedly by simply flipping over the permanent magnet beneath the nickel surface. The ratio of the integrated reduction peaks of MB varies by 10.9% ± 0.6% upon switching the magnetic field direction (up/down). Increasing the length of the individual DNA helices in these films to 30 bp consistently results in a larger ratio, 15 ± 1%.

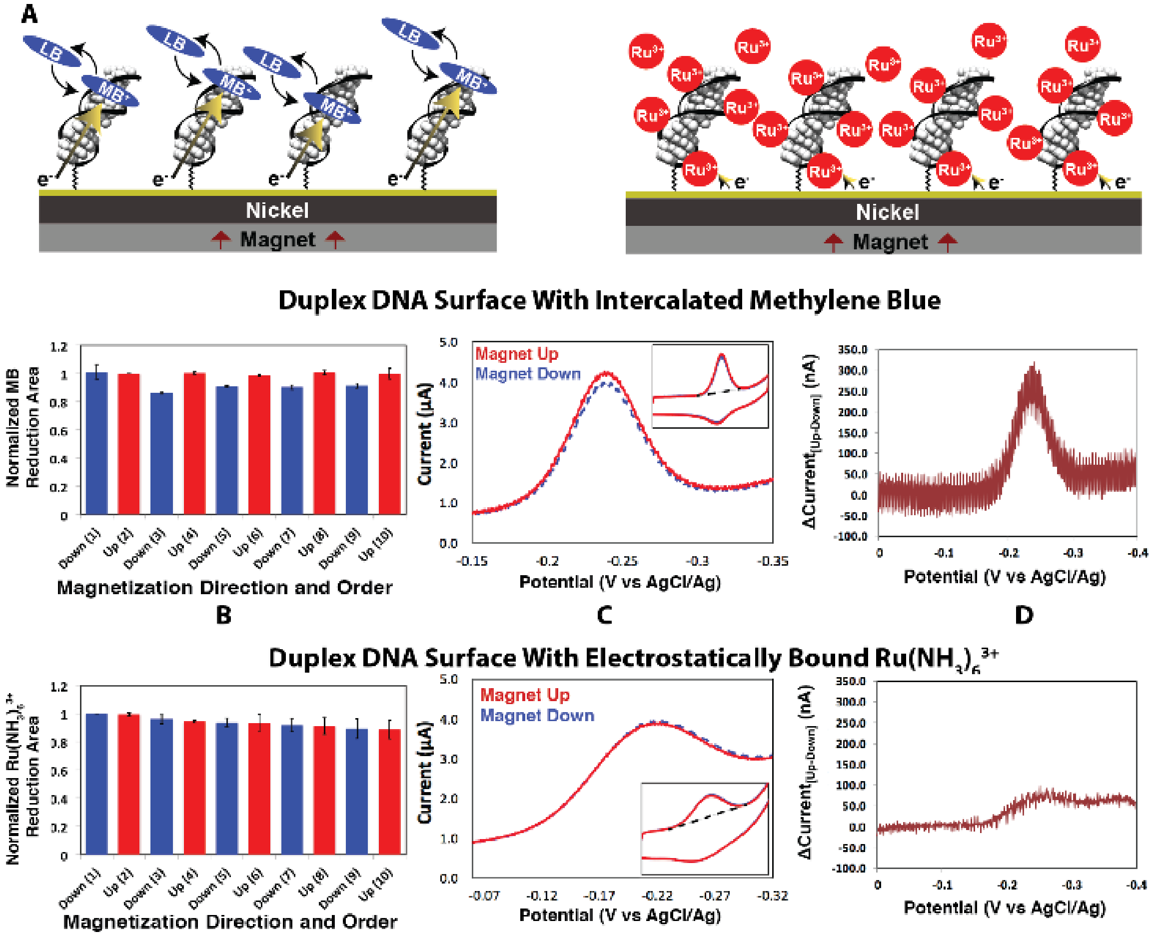

Figure 2.2 Cyclic voltammetry of electrodes modified with 16 bp dsDNA. A. Illustration of the dsDNA modified electrodes with 1 µM MB (left) or 10 µM $Ru(NH_3)_6^{3+}$ (right). MB intercalates into dsDNA and CT is through the helix, while $Ru(NH_3)_6^{3+}$ binds electrostatically to the phosphate backbone and electron transfer is directly from the surface. B. For intercalated MB (above) and electrostatically bound $Ru(NH_3)_6^{3+}$ (below) reduction yield in aqeuous buffer (pH 7, 5 mM phosphate, 50 mM NaCl, and 10 mM $MgCl_2$) upon switching the magnetic field direction. The change in yield is highly reproducible for at least 10 changes in magnetic field direction with the same surface. Data were normalized to the first scan with the magnetic field pointing up. The experiment was repeated 3 times with independently created surfaces and the standard error is plotted. C. Representative cyclic voltammograms scanning methylene blue (above) or $Ru(NH_3)_6^{3+}$ (below) with the magnet up (red, solid) and magnet down (blue, dotted). D. Difference plot for the reduction of methylene blue (above) or $Ru(NH_3)_6^{3+}$ (below) showing the current when the magnetic field is pointing up minus the current when the magnetic field pointing down. The $Ru(NH_3)_6^{3+}$ experiments were typically done following MB experiments on the same surface.

Importantly, the difference in reduction yield is observed regardless of which direction the nickel is magnetized initially, and the difference persists even when taking multiple scans. There is also no discernible change in the magnetic field effect upon varying the scan rate between 10 mV/s and 20 V/s (21).

The magnetic field dependence of DNA CT was also examined using Nile blue (NB) as a redox probe. NB is covalently bound to DNA, and conjugated through a DNA base, and has been used extensively as a covalent redox reporter (Figure 2.3) (24-26). Self-assembled monolayers of 17 bp thiolated dsDNA with tethered NB (~40 pmol/cm^2) show a change in the integrated reduction peaks of 7 ± 1% upon switching the magnetic field direction. The magnitude of this effect increases with increasing length of dsDNA to 12 ± 2% for 29bp, 16 ± 4% for 43bp, and 29 ± 6% for 60bp oligomers (Figure 2.4). These data with NB reveal a clear dependence of the yield of DNA CT on magnetic field orientation.

There is no measurable effect on the charge-transfer rates with a change in magnetic field direction. To test for effects of the magnetic field on the CT rate, we varied the scan rate from 50 mV/s to 20 V/s (Figure 2.5); we see no difference in the cathodic/anodic peak splittings when the magnetic field direction is switched, suggesting that there is no measurable effect on the charge transfer rates with a change in magnetic field direction. We stress, however, that previous work has shown that in these electrochemical experiments the DNA CT rates are limited by tunneling through the alkanethiol linker, not transport through the DNA, so small changes in the inherent

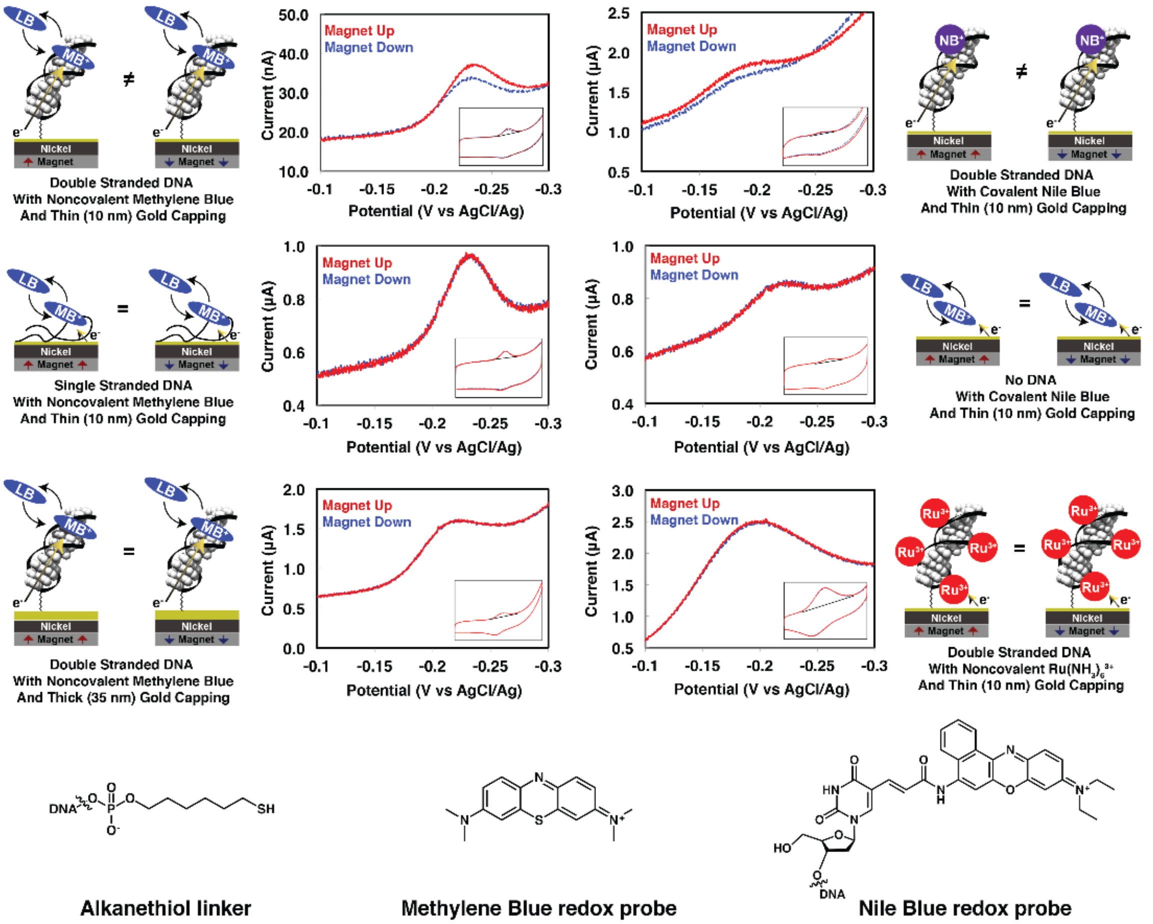

Figure 2.3 Representative cyclic voltammetry data for various assemblies of DNA-modified electrodes. 29 bp dsDNA was tethered to a gold-capped nickel surface with an alkanethiol linker. In all cases the data were obtained at 100 mV/s scan rate in phosphate buffer (5 mM NaH_2PO_4, 50 mM NaCl, pH 7.0). A permanent neodymium magnet with surface field strength of 0.66T was placed 2 mm underneath the surface and flipped to give a magnetic field pointing towards (up, red) or away from (down, blue) the surface. Shown (center) are cyclic voltammograms for 1 μM MB with dsDNA linked to a 10 nm thick gold cap (top left), covalent NB conjugated to dsDNA linked to a 10 nm thick gold cap (top right), 1 μM MB in contact with single stranded DNA adsorbed to a 10 nm thick gold cap (center left), 10 μM MB in contact with a 10 nm thick gold cap without DNA (center right), 1 μM MB with dsDNA linked to a 35 nm thick gold cap (bottom left), 10 μM $Ru(NH_3)_6^{3+}$ with dsDNA linked to a 10 nm thick gold cap (bottom right). Insets display the full cyclic voltammogram, while the larger plot displayed is centered around the reduction peak of the redox probe. Each experiment was conducted a minimum of 3 times per assembly, with at least 3 completely independent assemblies. Below are illustrations of the alkanethiol linker, the MB redox probe, and the NB redox probe.

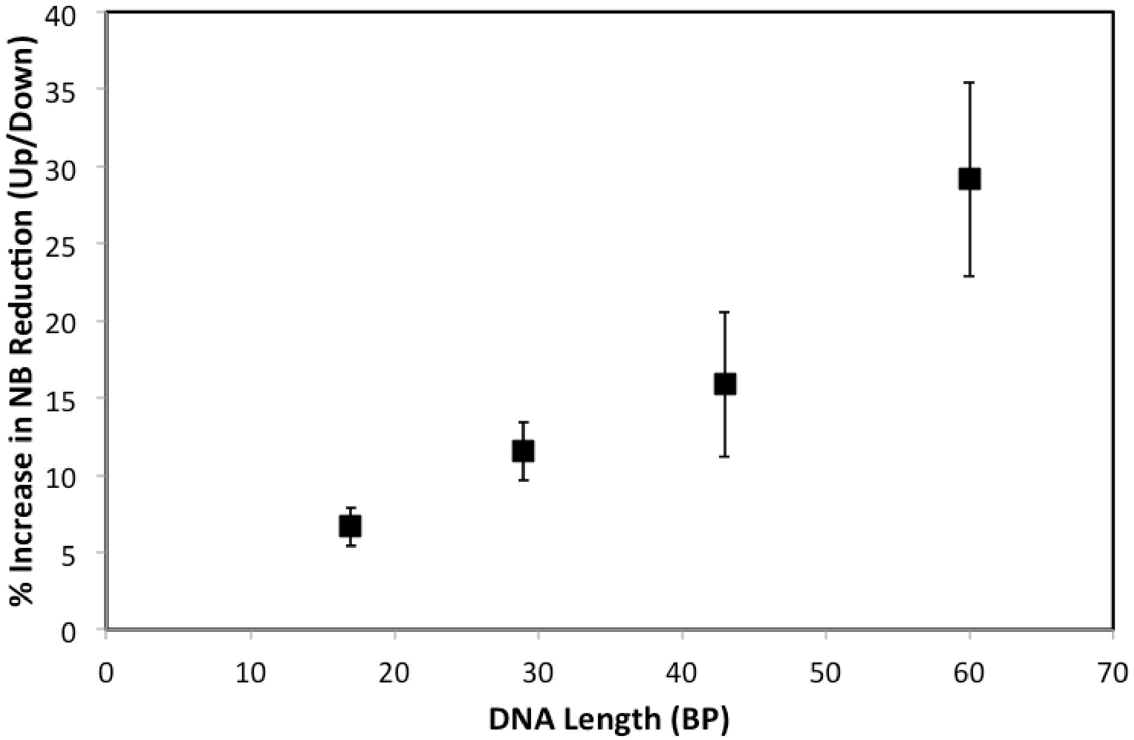

Figure 2.4 Plot of the magnetic field effect observed for DNA with covalently tethered Nile blue at different lengths scanned at 20 V/s in phosphate buffer. Each error bar represents the standard error from at least 3 separate surfaces. ANOVA shows a statistically significant difference for the effect being length dependent with p = 0.017.

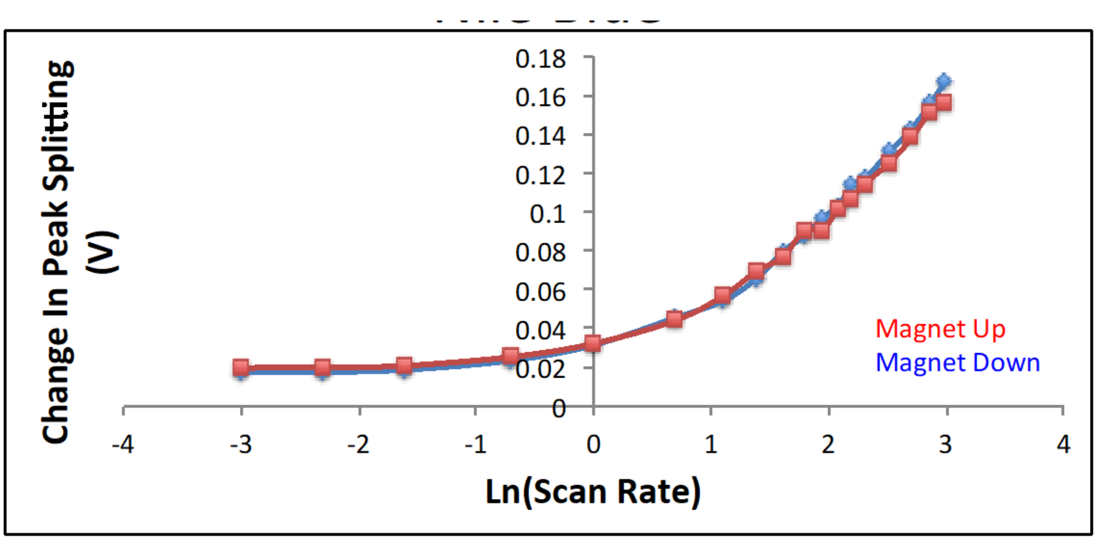

Figure 2.5 Scan Rate dependence of covalently tethered Nile blue reduction through duplex DNA.

tunneling efficiencies of oppositely polarized currents through the π-stack would not be accessible electrochemically (27).

Our data lead to the calculation that electrons traveling through a densely packed monolayer of 16 bp dsDNA to MB must be at least 22.5±1.2% spin polarized at ambient temperature. Charge transport through 60 bp dsDNA to a covalently tethered NB probe must be at least 55±10% spin polarized. It should be evident that decreasing the initial spin polarization will increase the calculated spin polarization through dsDNA; therefore, these calculated values can be considered lower estimates. If the nickel injected 13% spin polarized electrons, then the electrons passing through 60bp dsDNA would be 100% spin polarized, which could be treated as a theoretical maximum.

Given the range of possible etiologies for the observed magnetic field effect on the electrochemistry of MB and NB, we carried out a series of control experiments (Figure 2.3). Monolayers in which MB is adsorbed directly onto the gold-capped nickel electrodes in the absence of DNA show no differences in the reduction yield of MB upon switching the orientation of the magnetic field. Similarly, there is no magnetic field effect on the reduction of MB bound electrostatically to surfaces coated with single stranded DNA. Moreover, capping the nickel electrodes with a thicker (35 nm) gold layer eliminates the magnetic field effects, even for electrodes modified with dsDNA.

Nonintercalative redox probes were also examined for comparison. $Ru(NH_3)_6^{3+}$ binds electrostatically to the phosphate backbone of DNA and undergoes rapid electrochemical reduction to $Ru(NH_3)_6^{2+}$ at dsDNA-modified electrodes

(28). Significantly, we find no magnetic field dependence of the $Ru(NH_3)_6^{3+/2+}$ couple, despite its proximity to the chiral macromolecule and likely helical path (Figure 2.2). We also prepared dsDNA with a covalently bound diazobenzene probe (dabcyl) tethered to the 3′-phosphate near the electrode surface. This arrangement allowed us to monitor simultaneously the direct electrode reduction of dabcyl, which contacts the electrode surface, and the DNA-mediated reduction of MB. There is a significant difference in the up/down yield of MB reduction, but no measurable difference for the dabcyl signal (Figure 2.6).

We examined the effect of an intervening single base mismatch in the film (Figure 2.7). A mismatch incorporated into dsDNA between the surface and the redox probe decreases the yield of CT to either MB or NB, which shows that the DNA duplex mediates the CT (24); charge migrates *through* the DNA base pair stack. Interestingly, the spin selectivity measured through a mismatch mirrors the magnitude of the effect seen in well-matched duplexes of similar length. This result suggests that when charge is successfully transported through dsDNA with a mismatch, it travels through the entire dsDNA to the probe; the attenuation in CT yield with a mismatch leads to an interruption of some of that CT, but has no effect on spin selectivity.

Combined, these results indicate that (i) spin polarized currents induced by the underlying magnetic field are needed for spin selectivity in the DNA electrochemistry, (ii) spin selectivity requires double stranded DNA, and (iii) the magnetic field effects are observed only with probes that undergo CT reactions mediated by the DNA duplex.

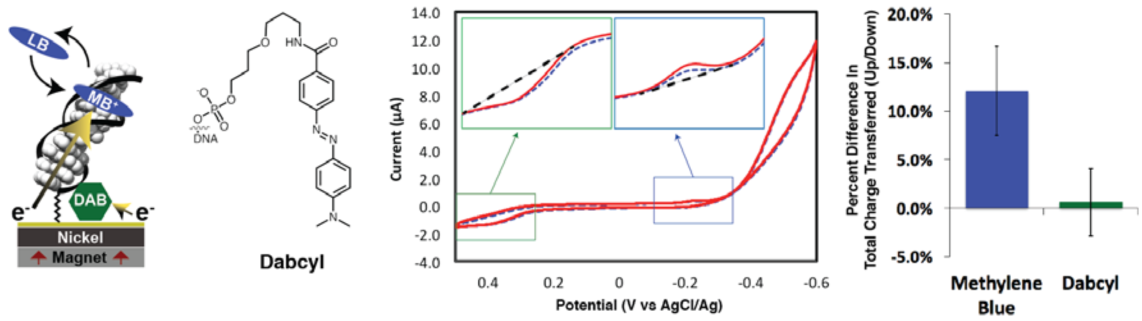

Figure 2.6. Cyclic voltammetry of 29bp dsDNA with covalently tethered dabcyl and noncovalently intercalated MB. (Left) Cartoon representing the DNA tethered to the surface and the paths the electrons take from the surface to their respective redox probes. (Center Left) Illustration of dabcyl molecule. (Center Right) Representative cyclic voltammogram of DNA with 1 μM MB with the magnetic field pointing towards the surface (red, up) or away from the surface (blue, down). The insets show the dabcyl oxidation (green border) and methylene blue reduction (blue border). The signal centered around -0.5V corresponds to the reduction of dabcyl, while its oxidation appears at 0.3 V. Note that scans were carried out at 10 mV/s given the slow proton-coupled redox reaction. (Right) The difference in cyclic voltammetry data for the reduction of MB (blue), and the oxidation of dabcyl (green) between the two magnetic field directions.

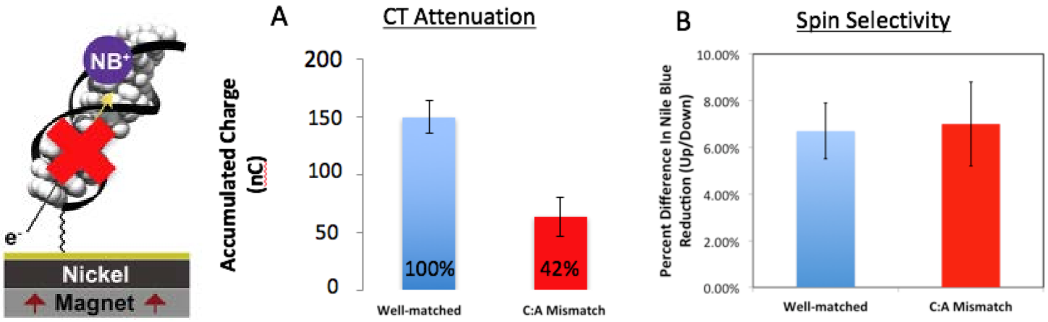

Figure 2.7. Summary of cyclic voltammetry data for 17bp duplex DNA with a C:A mismatch 6 nucleotides from the surface. **A,** A mismatch (red) has decreased total yield of NB reduction when compared to a well-matched duplex (blue) . **B**, The spin selectivity for probe reduction is the same for DNA with (blue) and without (red) a C:A mismatch.

If the helical structure of dsDNA is responsible for the apparent CISS behavior in these films, it follows that reversing the chirality of the helices would switch the sense of the magnetic field effect. Indeed, this is precisely what we find. Both methylated and unmethylated monolayers of 16bp duplexes featuring d(CG)$_8$ repeats were self-assembled onto gold-capped nickel. Circular dichroism confirms that DNA oligomers containing 5-methylcytosine, d(^{m}CG)$_8$, undergo a B-to-Z transition in the presence of 10 mM $MgCl_2$, while the unmethylated analog, d(CG)$_8$, remains in B-form (Figure 2.1); methylated Z-DNA reverts back to B-DNA upon rinsing away the $MgCl_2$ (18, 29, 30). Previous work has shown that MB intercalates into both B- and Z-DNA and undergoes DNA-mediated reduction in the presence of 10 mM $MgCl_2$ (19).

We carried out the electrochemistry to examine B- and Z-form helices on a multiplexed chip (24) consisting of 16 separate gold-capped nickel regions that allowed for the simultaneous comparison of four distinct monolayers under the identical magnetic field (Figure 2.8). In the absence of $MgCl_2$, both methylated and unmethylated DNA films show the same favored magnetization direction for a higher yield of MB reduction (up/down ratio = 18 ± 3%). Upon addition of 10 mM $MgCl_2$, the unmethylated films show no change in behavior, but the methylated films switch which magnetic field direction promotes the higher yield of MB reduction (up/down ratio = −9 ± 2%). Replacing the buffer with one that lacks $MgCl_2$ reverts the structure from Z- to B-form and restores the original characteristics, yielding again an up/down ratio of 18 ± 2% for both films.

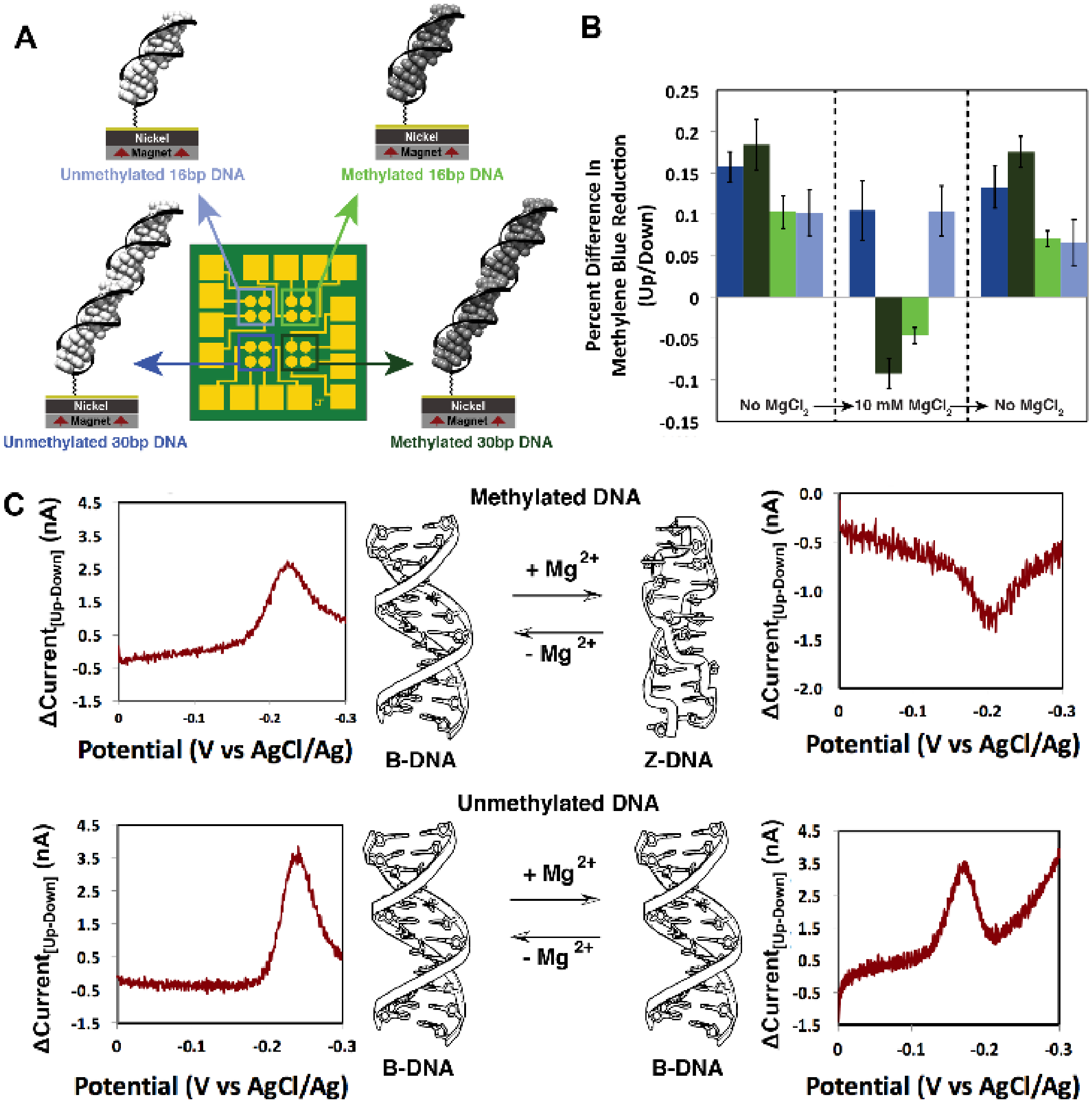

Figure 2.8 Switching of methylated and unmethylated dsDNA measured on a single multiplexed chip. A. A chip with 16 separate gold-capped nickel regions allowed for the comparison of four distinct monolayers made from 16 and 30 bp methylated d(^{m}CG)$_{15}$ and unmethylated d(CG)$_{15}$ dsDNA. The data were obtained at 100 mV/s scan rate with 1 μM MB in phosphate buffer (5 mM NaH_2PO_4, 50 mM NaCl, pH 7.0). B. Summary of cyclic voltammetry data for the two magnetizations were collected for all four quadrants with no $MgCl_2$, then with 10 mM $MgCl_2$, then once washing away the $MgCl_2$. Each bar represents a minimum of 4 separate electrode surfaces with at least 36 separate scans. The standard error is used to represent deviations from the mean. C. Representative example of 30 bp (top) methylated d(^{m}CG)$_{15}$ and (bottom) unmethylated d(CG)$_{15}$ DNA either with 10 mM $MgCl_2$ (right) or with no $MgCl_2$ (left) from two electrodes on the same surface. Data are plotted as the difference in current for a reductive sweep when the magnetic field is pointing up minus the current when the magnetic field pointing down.

DNA Sequence	Avg Charge Up/Down	SE	Spin Polarization (%)	SE	N
16MB	1.11	0.01	23	2	3
30MB	1.15	0.01	30	2	3
17NB	1.07	0.01	15	2	3
17NB (Mismatch)	1.07	0.02	15	4	3
29NB	1.12	0.02	25	4	3
43NB	1.16	0.04	32	7	3
60NB	1.29	0.06	55	10	4
30mCG (Before)	1.18	0.03	36	5	6
30mCG (Mg)	0.91	0.02	-19	4	6
30mCG (After	1.18	0.02	36	4	6
16mCG (Before)	1.1	0.02	21	4	12
16mCG (Mg)	0.95	0.01	-11	2	12
16mCG (After)	1.07	0.01	15	2	12
30CG (Before)	1.16	0.02	32	4	8
30CG (Mg)	1.1	0.04	21	8	8
30CG (After)	1.13	0.03	27	6	8
16CG (Before)	1.1	0.03	21	6	4
16CG (Mg)	1.1	0.03	21	6	4
16CG (After)	1.09	0.01	19	2	4
29DAB (MB)	1.18	0.07	36	11	7
29DAB (Dabcyl)	1.05	0.08	10	16	7

Table 2.1 Summary of all spin polarization data. Data shown are the average amount of charge up/down and its corresponding standard error (SE), the calculated spin polarization and its corresponding SE, and the number of independent sets of scans, N. Data were collected using cyclic voltammetry as described above. Spin polarization calculations were performed using equations 1.1-1.3 described above.

In addition to functioning as a magnetic field diode, switching between B- and Z-form dsDNA gives a difference in the magnitude of DNA CISS; normalized to the yield of electrochemically active MB and with the assumption that 10 mM $MgCl_2$ results in complete conversion of surface-bound DNA to Z-form, B-DNA appears to have an approximately 50% larger spin selectivity than Z-DNA. This change in magnitude of spin selectivity correlates well with the change in pitch between B-DNA and Z-DNA (3.32 and 4.56 nm respectively) but may result from other differences between the two forms (such as the greater π-stacking in the B- versus Z-form) (18, 29, 30). These data suggest that the charge is moving through the duplex along a helical path, because a charge moving in a fully delocalized π-stacked column would not be able to interact with the handedness of the macromolecule; helical transport among delocalized domains of a few base pairs is possible.

The CISS measured in these experiments is significantly larger than expected for molecules that lack large spin–orbit coupling. Calculating the energy difference between the two electron spins at the surface of fully magnetized nickel (~0.6 T) yields a gap ($\mu_B gB \approx 1\ \text{cm}^{-1}$) far lower than k_bT at ambient temperature. Several theoretical models have been proffered to rationalize the large CISS exhibited by chiral organic films (16, 17, 31-35). Aspects of each of these models can be used to understand our data. In addition, it is worthwhile to consider other factors not currently included in these models that are important in the context of DNA CT, such as the large polarizability of the π-stack in dsDNA(36) or the delocalization of domains across multiple adjacent nucleotides(37, 38).

Summary and Conclusions

Our experiments thus demonstrate that magnetic fields can affect the flow of electrons through native, hydrated dsDNA. Significantly, our data show that electrochemically generated DNA CISS is observed only at films containing duplex DNA and with redox probes intercalated into the π-stack that undergo DNA-mediated CT. Magnetic field effects are not observed with redox reporters bound electrostatically to the DNA duplex nor with tethered reporters that contact the surface directly. It is not simply the electrostatic helical field that is responsible for the spin selectivity. Nor is it simply the chiral centers on the DNA; redox reporters bound to single stranded DNA do not show magnetic field effects. As with DNA CT, the extended π-stack appears to play a crucial role: reversing the handedness of the helix in the films generates a diode-like spin-filtering response. It is interesting to consider how conformational changes such as that between B- and Z-DNA might be utilized as a diode in organic spintronics, indeed, how this spin filtering might be applied in practical devices. Finally, it is intriguing to consider whether Nature exploits this helix-dependent spin selectivity of DNA in some context.

References

(1) Genereux, J. C.; Barton, J. K. *Chem. Rev*. **2010**, 110, 1642−1662.

(2) Guo, X.; Gorodetsky, A. A.; Hone, J.; Barton, J. K.; Nuckolls, C. *Nat. Nanotechnol*. **2008**, 3, 163−167.

(3) Muren, N. B.; Olmon, E. D.; Barton, J. K. *Phys. Chem. Chem. Phys*. **2012**, 14, 13754−13771.

(4) Berlin, Y. A.; Voityuk, A. A.; Ratner, M. A. *ACS Nano* **2012**, 6, 8216.

(5) Porath, D.; Cuniberti, G.; Felice, R. D. *Top. Curr. Chem*. **2004**, 237, 183.

(6) Drummond, T. G.; Hill, M. G.; Barton, J. K. *Nat. Biotechnol*. **2003**, 21, 6475.

(7) Barton, J. K.; Furst, A. L.; Grodick, M. A. In *DNA in Supramolecular Chemistry and Nanotechnology*, Stulz, E., Clever, G. H, Eds.; Wiley: West Sussex, U.K., **2015**.

(8) Gohler, B.; Hamelbeck, V.; Markus, T. Z.; Kettner, M.; Hanne, G. F.; Vager, Z.; Naaman, R.; Zacharias, H. *Science* **2011**, 331, 894.

(9) Xie, Z.; Markus, T. Z.; Cohen, S. R.; Vager, Z.; Gutierrez, R.; Naaman, R. *Nano Lett.* **2011**, 11, 4652−5644.

(10) Sun, D.; Ehrenfreund, E.; Varedny, Z. V. *Chem. Commun*. **2014**, 50, 1781−1793.

(11) Michaeli, K.; Kantor-Uriel, N.; Naaman, R.; Waldeck, D. H. *Chem. Soc. Rev*. **2016**, DOI: 10.1039/C6CS00369A

(12) Mondal, P. C.; Kantor-Uriel, N.; Mathew, S. P.; Tassinari, F.; Fontanesi, C.; Naaman, R. *Adv. Mater*. **2015**, 27, 1924−1927.

(13) Dor, O. B.; Yochelis, S.; Mathew, S. P.; Naaman, R.; Paltiel, Y. *Nat. Commun*. **2013**, 4, 2256.

(14) Gutierrez, R.; Diaz, E.; Naaman, R.; Cuniberti, G. *Phys. Rev. B: Condens. Matter Mater. Phys.* **2012**, 85, 081404.

(15) Naaman, R.; Waldeck, D. H. *Annu. Rev. Phys. Chem*. **2015**, 66, 263.

(16) Guo, A.-M.; Sun, Q.-F. *Phys. Rev. Lett*. **2012**, 108, 218102.

(17) Medina, E.; Lopez, F.; Ratner, M. A.; Mujica, V. *Eur. Phys. Lett*. **2012**, 99, 17006.

(18) Saenger, W. *Principles of nucleic acid structure*; Springer-Verlag: New York, **1984**.

(19) Boon, E. M.; Barton, J. K. *Bioconjugate Chem*. **2003**, 14, 1140− 1147.

(20) Mondal, P. C.; Fontanesi, C.; Waldeck, D. H.; Naaman, R. *ACS Nano* **2015**, 9, 3377−3384.

(22) Kelley, S. O.; Barton, J. K.; Jackson, N. M.; McPherson, L. D.; Potter, A. B.; Spain, E. M.; Allen, M. J.; Hill, M. G. *Langmuir* **1998**, 14, 6781.

(23) Kelley, S. O.; Barton, J. K.; Jackson, N.; Hill, M. G. *Bioconjugate Chem*. **1997**, 8, 31−37.

(24) Slinker, J. D.; Muren, N. B.; Renfrew, S. E.; Barton, J. K. *Nat. Chem*. **2011**, 3, 230−233.

(25) Gorodetsky, A. A.; Hammond, W. J.; Hill, M. G.; Slowinski, K.; Barton, J. K. *Langmuir* **2008**, 24, 14282−14288.

(26) Muren, N. B.; Barton, J. K. *J. Am. Chem. Soc.* **2013**, 135, 16632− 40.

(27) Drummond, T. G.; Hill, M. G.; Barton, J. K. *J. Am. Chem. Soc*. **2004**, 126, 15010.

(28) Yu, H.-Z.; Luo, C.-Y.; Sankar, C. G.; Sen, D. *Anal. Chem.* **2003**, 75, 3902.

(29) Hartmann, B.; Lavery, R. Q. *Rev. Biophys.* **1996**, 29, 309−368.

(30) Wang, A. H.-J.; Quigley, G. J.; Kolpak, F. J.; Crawford, J. L.; Van Boom, J. H.; Van Der Marel, G. A.; Rich, A. *Nature* **1979**, 282, 680−686.

(31) Gutierrez, R.; Diaz, E.; Naaman, R.; Cuniberti, G. *Phys. Rev. B: Condens. Matter Mater. Phys*. **2012**, 85, 081404.

(32) Gutierrez, R.; Diaz, E.; Gaul, C.; Brumme, T.; Dominguez-Adame, F.; Cuniberti, G. *J. Phys. Chem. C* **2013**, 117, 22276−22284.

(33) Guo, A. M.; Sun, Q. F. *Proc. Natl. Acad. Sci*. **2014**, 111, 11658−11662.

(34) Gersten, J.; Kaasbjerg, K.; Nitzan, A. *J. Chem. Phys.* **2013**, 139, 114111.

(35) Michaeli, K.; Naaman, R. *arXiv*, **2016**, 1512.03435v2.

(36) Williams, T. T.; Barton, J. K. *J. Am. Chem. Soc*. **2002**, 124, 1840− 1841.

(37) O'Neil, M. A.; Barton, J. K. *J. Am. Chem. Soc*. **2004**, 126, 11471.

(38) Xiang, L.; Palma, J. L.; Bruot, C.; Mujica, V.; Ratner, M. A.; Tao, N. *Nat. Chem*. **2015**, 7, 221−226.

Chapter 3

A Compass at weak Magnetic Fields using Thymine Dimer Repair by Photolyase

T.J. Zwang designed and performed all experiments except for protein purification and SQUID measurements.

Introduction

Migratory birds and other animals can detect Earth's magnetic field as a sensor for navigation, though the mechanisms underlying this magnetic sensing are unclear (1). The two mechanisms proposed to explain the phenomenon of avian magnetoreception are not mutually exclusive and involve sensing using (i) magnetically sensitive radical pairs or (ii) magnetic iron-containing nanoparticles (2), but neither have been demonstrated. Photolyases are enzymes that repair UV-induced lesions and contain a highly conserved core structure that could be involved in such magnetosensitive radical pair chemistry. The conserved photolyase homology region contains a redox-active flavin adenine dinucleotide cofactor (FAD), which absorbs blue light, that can access lesions via a cavity in the center of a positively charged groove where DNA binds (3). Photoreduction of FAD to FADH- is mediated by three consecutive electron transfers along a conserved triad of tryptophan residues to give a flavosemiquinone radical (FAD$^{\bullet}$-) and a radical (TrpH*+) that has been shown through transient absorption spectroscopy to be sensitive to weak applied magnetic fields (in the range of 30-390 Gauss) that are still much stronger than the earth's magnetic field (0.25-0.65 Gauss) (4).

Here we explore how a magnetic field affects DNA repair by photolyase. We employ DNA-modified electrodes immersed in aqueous buffer to monitor photolyase from *Escherichia coli* with respect to binding and repair of its substrate, a cyclobutane pyrimidine dimer (CPD). CPD repair can be monitored electrically since the CPD lesion within a DNA duplex disrupts the internal stacking of the duplex DNA, thereby inhibiting efficient charge transfer through the DNA duplex between the electrode and the flavin cofactor (5). DNA-mediated charge transport (DNA CT) relies on charge moving *through* the internal base pair stack of the DNA duplex (6). In this chemistry, the efficiency of DNA CT is extremely sensitive to disruptions in base stacking such as arise with an abasic site or lesion. CPD lesions form as a result of a photoinduced [2+2] cycloaddition between two adjacent pyrimidines, typically thymines, on the same DNA strand and significantly kink duplex DNA (5). *E. coli* photolyase repairs CPD lesions in a reductive catalytic cycle upon irradiation of the fully reduced flavin cofactor ($FADH^-$) with blue light (7). Upon repair of the CPD by photolyase, DNA regains its well stacked structure and is able to support efficient DNA CT to the flavin cofactor (5). As a result, the repair of CPD lesions by photolyase is monitored as an increase in electrochemical response, because the repair directly improves the yield of DNA-mediated CT between the electrode and flavin.

Materials and Methods

DNA Synthesis

All materials for DNA synthesis were purchased from Glen Research. Oligonucleotides were synthesized on an Applied Biosystems 3400 DNA synthesizer using phosphoramidite chemistry on a controlled-pore glass support. The two strands of a duplex are synthesized separately, purified, stored frozen, and then annealed prior to electrochemical experiments. The 5’- end of one strand is modified with a C6 S-S phosphoramidite that is later reduced before use. The 5’- end of the complementary strand is either unmodified or modified with an NHS-Carboxy-dT phosphoramidite for later coupling with Nile blue. High pressure liquid chromatography (HPLC) was performed using a reverse-phase PLRP-S column (Agilent) using a gradient of acetonitrile and 50 mM ammonium acetate (5-15% ammonium acetate over 35 minutes).

Unmodified DNA. DNA was synthesized using standard phosphoramidites and reagents. After synthesis, the DNA was lyophilized overnight. It was then cleaved from the solid support by incubation at 60^o C with concentrated (28-30%) NH_4OH for 12 hours, filtered using CoStar columns, and then dried. The dried DNA film was resuspended in phosphate buffer (5 mM phosphate, pH 7, 50 mM NaCl) and HPLC-purified. The DMT (4,4'-dimethoxytrityl) group protecting the 5'- end was then removed by incubation with 80% acetic acid for 45 minutes. The reaction mixture was dried and resuspended in phosphate buffer. The DNA was isolated using HPLC. The purified oligonucleotide was desalted using ethanol precipitation, dried, and the mass confirmed with Matrix-assisted laser desorption/ionization- time of flight mass spectrometry (MALDI-TOF). Unmodified oligonucleotides were then stored at -20^oC in phosphate buffer until annealing with their complementary strand.

Cyclobutane pyrimidine dimer generation. Single stranded DNA (1 ml of 100-200 µM) with a single TT, UU, TU, or UT was suspended in aqueous buffer containing 1 mM acetophenone, 5 mM NaH_2PO_4, 50 mM NaCl, pH 7.5 and degassed with argon in a glass container. The container was sealed and irradiated with a solar simulator (Oriel instruments) or 302 nm UV light (spectroline transilluminator model TR-302) for 10 minutes. Following irradiation the DNA was purified using high performance liquid chromatography (HPLC) using a reverse-phase PLRP-S column (Agilent) using a gradient of acetonitrile and 20 mM ammonium acetate (2-3% acetonitrile over 10 minutes, then 3-4% over the next 30 minutes) at 80°C and a flow rate of 0.8 ml/min to separate the CPD from undimerized ssDNA. Both 16 and 29 bp ssDNA show a separation with CPD compared to without a CPD of approximately 4 minutes with the CPD containing strand eluting first.

Thiolated DNA. DNA was synthesized using standard phosphoramidites and reagents, with the exception of a C6 S-S phosphoramidite that was attached to the 5'-end. After synthesis, the DNA was lyophilized overnight. It was then cleaved from the solid support by incubation at 60° C with concentrated (28-30%) NH_4OH for 12 hours, filtered using CoStar columns, then dried. The dried DNA film was resuspended in phosphate buffer (5 mM phosphate, pH 7, 50 mM NaCl) and HPLC-purified. The DMT (4,4'-dimethoxytrityl) group protecting the 5'- end was then removed by incubation with 80% acetic acid for 45 minutes. The reaction mixture was dried and resuspended in phosphate buffer. The DNA was isolated using HPLC as described above. The purified oligonuceotide was desalted using ethanol precipitation, dried, and the mass confirmed with Matrix-assisted laser desorption/ionization- time of flight mass spectrometry (MALDI-TOF). Within one week of annealing, the dithiolated DNA was reduced by resuspending in 50 mM Tris-HCl, pH 8.4, 50 mM NaCl, 100 mM dithiothreitol (Sigma) for 2 hours. The reduced thiol-modified DNA was then purified by size exclusion chromatography (Nap5 Sephadex, G-25, GE Healthcare) with phosphate buffer as the eluent and subsequently purified using HPLC.

Annealing Duplex DNA. Duplex DNA for electrochemistry was prepared by first quantifying the complementary strands with UV-Visible spectroscopy, and then mixing equimolar (50 μM) complementary strands in 200 μl phosphate buffer. The DNA solution was then deoxygenated by bubbling argon for at least 5 minutes per ml. Duplex DNA was then annealed on a thermocycler (Beckman Instruments) by initial heating to 90°C followed by slow cooling over 90 minutes.

DNA Sequences:

16 bp DNA (with or without UV generated dimer)
5'-ACG TGA G<u>TT</u> GAG ACG T-3'
3'-TGC ACT CAA CTC TGC A-5' - SH
Thymine Dimer with CA mismatch near surface
5'-ACG TGA G<u>TT</u> GAA ACG T-3'
3'-TGC ACT CAA CTC TGC A-5' - SH

29 bp DNA (with or without UV generated dimer)
3'-ATC ACG TCA TAT GAA CTG ACT GGA CGG TG- 5' -SH
5'-TAG TGC AGT ATA CTT GAC TGA CCT GCC AC-3'

The above sequences use the following abbreviations for modifications:

HS-C_6 = hexanethiol linker; <u>TT</u> = Pyrimidine Dimer

Photolyase Preparation

Escherichia coli photolyase (*ec*PL) wild type and mutants N378C, M345A, E274A, as well as truncated *Arabidopsis Thaliana* cryptochrome 1 (*at*CRY1ΔC) without its C-terminal domain were provided by Prof. Donging Zhong (Ohio State University). Proteins were received at 180-300 μM in a buffer containing 100 nM NaCl, 50 mM Tris-

HCl at pH 7.5, 1 mM EDTA and 50% (v/v) glycerol. It is essential that these buffers do not contain dithiothretol or other sulfur compounds that are typically used to keep the proteins' flavin reduced because they may disrupt thiolated monolayers used in electrochemistry. Due of this, the proteins were generally received with a partially or fully oxidized flavin that needed to be photoreduced for enzymatic activity.

E. coli photolyase without the antenna cofactor was prepared as described previously (10, 17). The mutant plasmids were constructed using QuikChange II XL kit (Stratagene) based on the plasmid of wild-type enzyme. All mutated plasmids were sequenced to confirm the mutations.

The preparation of MBP-tag fused AtCry1 with depletion of the C-terminal tail (AtCRY1-DC) was as described elsewhere with some modifications (18). The AtCRY1-DC gene was cloned into the pMal-c2 vector (New England Biolabs) to obtain a construct that expresses AtCRY1-DC fused to the C-terminus of maltose binding protein (MBP). The MBP-tagged AtCRY1-DC was expressed in E. coli UNC523 and purified by affinity chromatography on amylose resin.

All proteins were obtained with stoichiometric flavin cofactor after purification and exchanged to a buffer containing 50 mM Tris at pH 7.5, 100 mM NaCl,1 mM EDTA, and 50% (v/v) glycerol for further use.

Before experiments 50 uM *ec*PL or *at*CRY1ΔC were placed in tris buffer (50 mM Tris-HCl, 50 mM KCl, 1 mM EDTA, 10% glycerol, pH 7.5) and irradiated with blue light (405 +/- 10 nm, <30 mW) from a diode laser pointer (Tmart) in an anaerobic chamber to photoreduce the flavin to its active form (Figure 3.1). All solutions containing photolyase were degassed to remove oxygen and kept in an anaerobic chamber (95% N_2, 5% H_2, <1 ppm O_2) to prevent oxidation of the flavin. During experiments with photolyase the protein was kept under constant blue light irradiation. If the flavin was not fully photoreduced, or if oxygen was able to access the flavin and oxidize it, the oxidized flavin peak would appear in cyclic voltammetry experiments centered around -420 mV vs AgCl/Ag. Further irradiation with blue light in anaerobic conditions remove this peak. The presence of this peak did not appear to have a significant effect on measurements of total charge transferred at later time points when it was removed by reduction of the flavin with blue light.

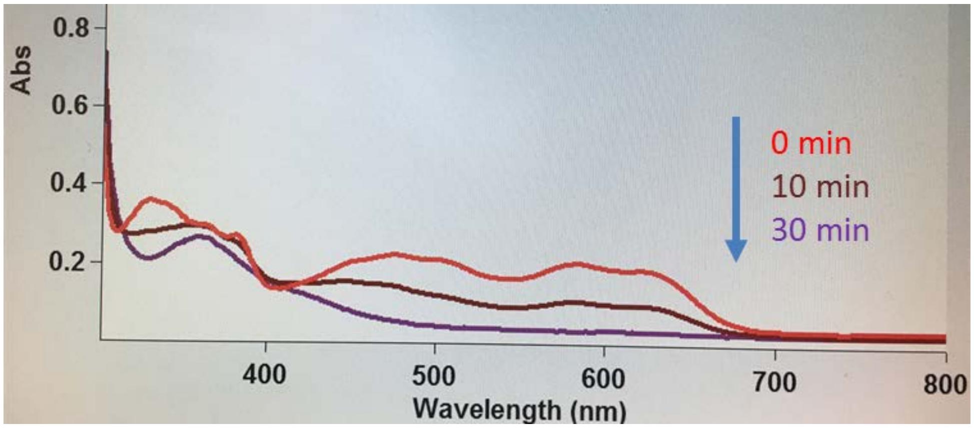

Figure 3.1 Typical photoreduction measurement of WT photolyase by blue light blue light (405 +/- 10 nm, <30 mW) from a diode laser pointer. Photoreduction was carried out anaerobically and then transferred to a UV/Vis spectrophotometer in an air-tight cuvette.

Electrode Fabrication

Multiplexed electrode surfaces were fabricated following the protocol outlined in chapter 2 except here the top of the electrode had a 1000 Å thick gold layer and there was no nickel layer (8).

DNA-modified electrode preparation

Multiplexed chips are gently cleaned by sonicating with acetone and then isopropanol before drying with argon. They are then cleaned with UV/Ozone for 20 minutes. Immediately after cleaning the surface, a plastic clamp and rubber (BunaN) gasket are affixed to the surface to create a well for liquid and 50 μM duplex DNA in phosphate buffer (pH 7, 5 mM phosphate, 50 mM NaCl to make dsDNA films. The dsDNA was incubated on the surface for 18-24 hours. Once the dsDNA is on the surface, it cannot be dried without compromising the structure and therefore the measured properties of the film. The solution was then exchanged 5x with 1 mM mercaptohexanol in phosphate buffer (pH 7, 5 mM phosphate, 50 mM NaCl, 5% glycerol) and incubated for 45 minutes. Lastly the surface was rinsed at least 5x with tris buffer (50 mM Tris-HCl, 50 mM KCl, 1 mM EDTA, 10% glycerol, pH 7.5).

Electrochemical measurements

The central well around the electrode surface created by the clamp was filled with aqueous buffer containing 50 mM Tris-HCl, 50 mM KCl, 1 mM EDTA, 10% glycerol, pH 7.5. An AgCl/Ag reference electrode (Cypress) was coated with a solidified mixture of 1% agarose and 3M NaCl in water inside a long, thin pipette tip. The tip was cut so that the salt bridge could connect the electrode to the buffer from the top of the well. A platinum wire used as an auxiliary electrode was also submerged in the buffer from the top of the well. The working electrode contacted a dry part of unmodified gold surface. A CH1620D Electrochemical Analyzer (CH Instruments) was used to control the electrochemical experiments.

Magnetic field measurements

Magnetic field experiments were conducted using 462 Gauss, 918 Gauss, 1803 Gauss, and 6619 Guass surface strength magnetic field neodymium magnet (K&J Magnetics). Alligator clips were replaced with nonmagnetic stainless steel to minimize magnetic interference. All other parts of the assembly were created using plastic to prevent extraneous objects the magnetic field could influence. Additionally, the strong magnet was waved near the potentiostat during operation, with no obvious change in signal that was apparent, to ensure that the magnet was not interfering with the operation of the potentiostat. Each experiment that was conducted using a magnetic field was compared to a similar quadrant on the same chip that was not tested under a magnetic field and when compared to other experiments was normalized using this data. Generally there was little variation seen when using the same dsDNA on different surfaces; however, using dsDNA made at different times could result in different maximum values for repair, possibly due to slight differences in surface packing, purity, or efficiency of thymine dimer generation. Background magnetic field strength and applied magnetic field strength were tested by measuring the x,y,z coordinates of the magnetic field at the surface of the electrode using a gauss meter (F.W. Bell, 5100 series).

SQUID measurements

SQUID measurements were performed by Jennifer Buz in Joseph Kirschvink's laboratory using a 2G Enterprise SQUID magnetometer. Electrode surface was incubated with DNA and protein then dried. A strong magnet (6619 Gauss) was waved near the surface, and then the surface was scanned with maximum sensitivity to detect magnetite or other dipoles present on the surface. Some contamination was observed on sample edges, but no magnetite was present on the electrode surfaces.

Results and Discussion

Figure 3.2 illustrates this electrical monitoring of repair through the cyclic voltammogram (CV) taken from one set of gold electrodes modified with duplex DNA containing a CPD, bound by photolyase and irradiated. When bound to the CPD, the redox-active flavin is apparent at -80 mV versus NHE. The signal, however, is small owing to the presence of the intervening CPD. Upon irradiation, the signal increases, as photolyase repairs the intervening CPD.

Multiplexed chips consisting of 16 separate DNA-modified gold electrodes allow for the simultaneous or sequential comparison of four distinct monolayers created under identical conditions with four-fold redundancy. This platform is essential for accurate comparisons of similar monolayers under conditions where the only variable is the magnetic field strength and/or direction. Figure 3.3 shows representative data from a single multiplexed chip where the two quadrants were incubated with the same thiolated duplex DNA containing a thymine dimer, one quadrant contains duplex DNA with a C:A mismatch intervening between the thymine dimer and the gold surface, and the last quadrant contains duplex DNA with no dimer or mismatches. When photolyase is added to a monolayer of duplex DNA, each containing a TT dimer (29 bp duplexes, ~8 pmol/ cm^2) in the absence of an applied magnetic field, irradiation with blue light leads to the increase in current for the FAD redox couple, as illustrated above. Shining light on an identical monolayer in the presence of an applied magnetic field, however, leads to a significant reduction in the yield of charge transferred over the same period of time. The lack of signal on the electrode modified with DNA but without the thymine dimer shows that the photolyase is binding only to its substrate CPD lesion. Furthermore, incorporating a single mismatch significantly decreases the yield of charge transferred to the flavin, indicating that the flavin is reduced and oxidized by charge transferred *through* the DNA duplex; perturbations to the base stack as occurs with a mismatch are sufficient to decrease DNA CT.

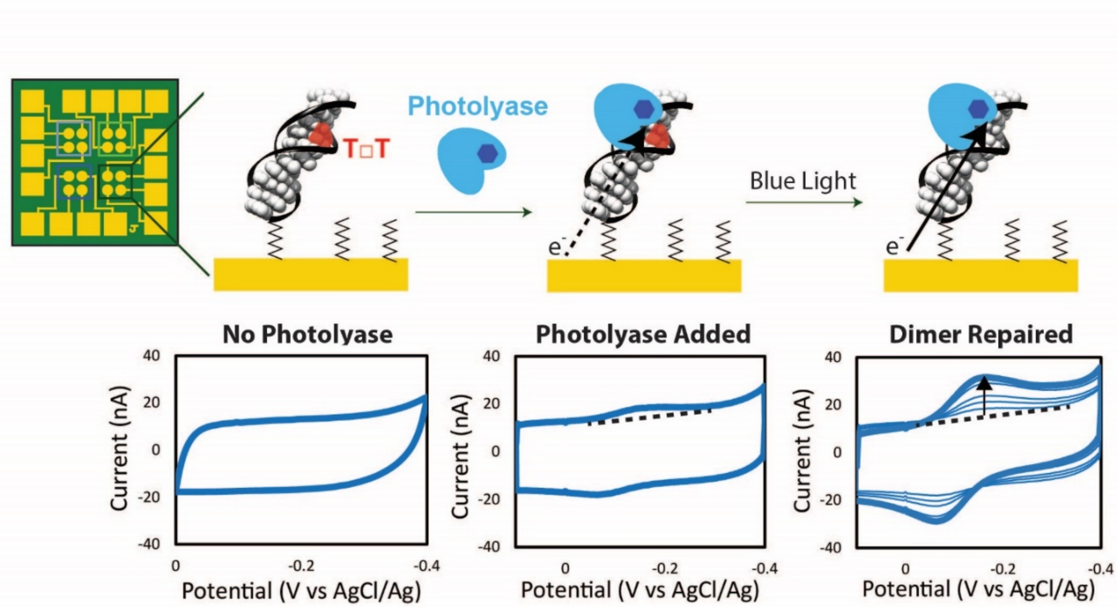

Figure 3.2 Cyclic voltammetry of photolyase on multiplexed chip electrodes modified with 29 bp dsDNA and backfilled with mercaptohexanol. (Left) Monolayer of duplex DNA, each with a single thymine dimer (T□T). (Middle) Addition of *E coli* photolyase shows a small flavin redox peak centered around -100 mV vs AgCl/Ag, which is consistent with the fully reduced flavin. (Right) Irradiation with blue light repairs the thymine dimer over time and increases the yield of charge transferred through the DNA duplex to and from the flavin. After subtracting the background current (dotted line) the area under the reductive peak can be integrated to give the total charge transferred to the flavin.

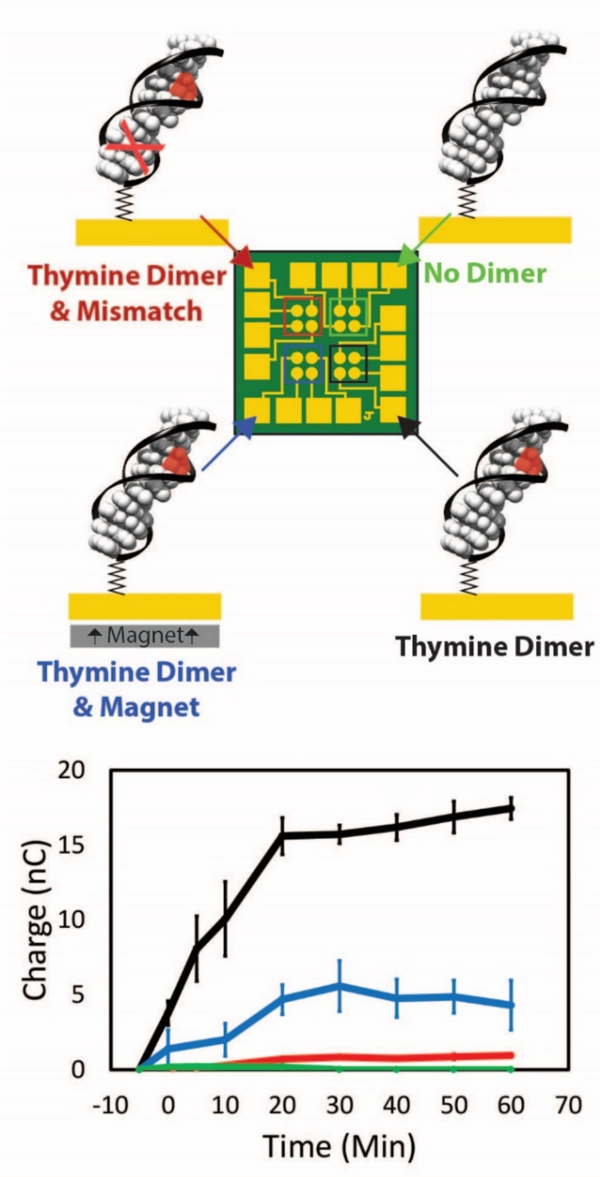

Figure 3.3 Integrated cyclic voltammetry measurements of photolyase on a representative multiplexed chip over time. (Top) Representation of the multiplexed chip and the different duplex DNA monolayers and experimental conditions that were tested. (Bottom) Plot of the area under the reductive peak was integrated to give the total charge transferred to the flavin. In each case 50 µM photolyase was added and irradiated with blue light at t=0. In the green quadrant the 29 bp dsDNA contained no thymine dimer. In the red quadrant the 29 bp dsDNA contained a thymine dimer and a C:A mismatch between the dimer and the electrode surface. In the black quadrant the 29 bp dsDNA contained a thymine dimer. In the blue quadrant the same 29 bp dsDNA containing a thymine dimer was used as was tested in the black quadrant, but the entire experiment was conducted with a 560 Gauss magnetic field pointing perpendicularly up, intersecting the plane of the electrode.

Control experiments show that the protein is still active after multiple hours of incubation and that the protein is able to access CPD-containing duplex DNA added to the solution above the electrode surface (Figure 3.4). There is also no distinguishable difference when adding this CPD-containing duplex DNA in the presence or absence of a magnetic field, suggesting that the magnetic field does not cause a significant change in photolyase affinity for CPD. Experiments with a SQUID magnetometer show that there is no magnetite on the surface that is influencing this chemistry (Figure 3.5).

The magnetic field influence on yield of DNA CT depends upon when the magnetic field is applied during the reaction. The presence or absence of an externally applied magnetic field during photoreduction, before the incubation of the protein with the duplex DNA substrate, does not influence the signal during repair (Figure 3.6). Importantly, removing the magnetic field during repair restores the yield of charge transfer as though the magnetic field were never present (Figure 3.7). After repair has been completed, adding a magnetic field has no influence on the yield of charge transferred. Together, these data indicate that the presence of the magnetic field directly influences the efficiency of repair.

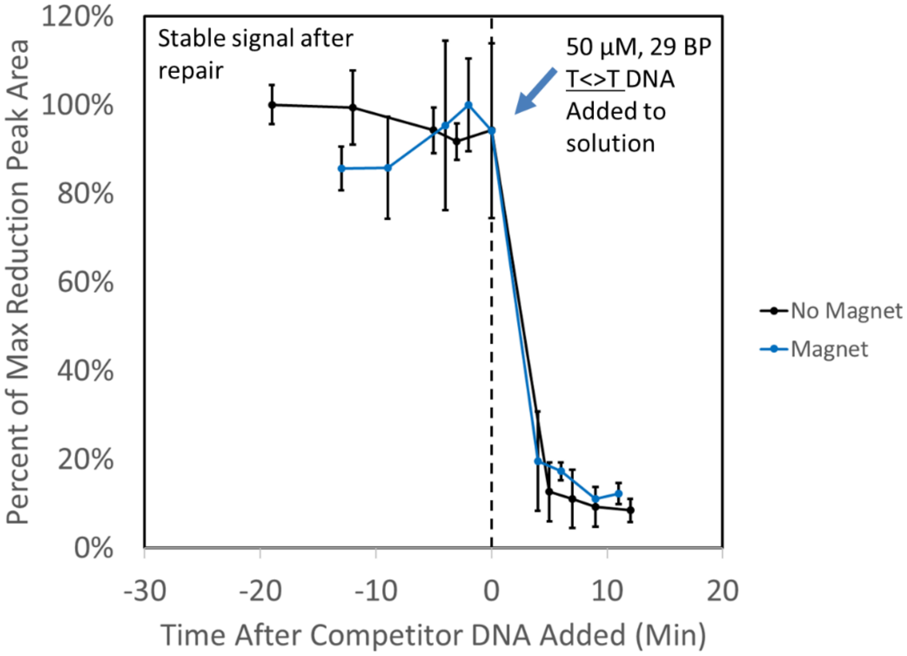

Figure 3.4 Plot of the reductive peak area from cyclic voltammetry of photolyase before and after the addition of competitor DNA. The addition of competitor dsDNA with a thymine dimer to a surface that has saturated the photolyase repair signal results in a significant decrease in signal indicative of the photolyase dissociating from the surface and binding the competitor dsDNA in solution. There is no observable difference with or without a magnetic field for the signal decrease.

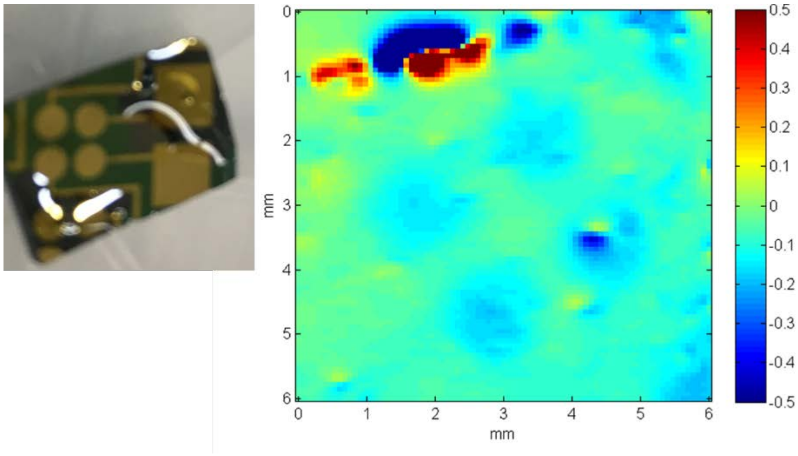

Figure 3.5 Measurement of multiplexed chip sample using SQUID magnetometer. Surface was incubated with dsDNA and photolyase as would be used in an experiment, then dried to make compatible with SQUID measurement. The surface was then magnetized by placing near a 6619 Gauss surface neodymium magnet to align any dipoles. The magnet did not come into contact with the surface for fear of contamination. Note that this is the only experiment with dried DNA because the duplex structure is unimportant here. The y-axis is in volts and the color scale represents 3 nT/V. This shows that there is no magnetite present on the multiplexed chip either due to the substrate or biological samples. A small contamination was observed on the edge of the chip likely due to mishandling of the sample, but even if these were assumed to be present in experiments the dipoles present are still too small to influence the experiments at the field strengths we used.

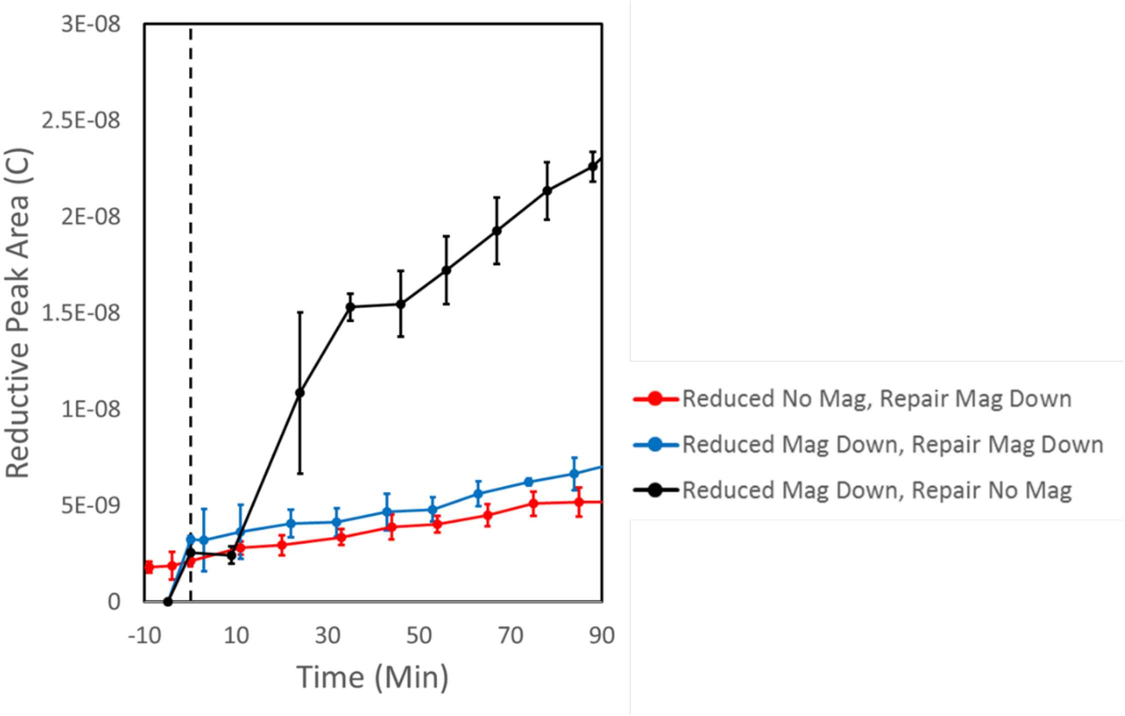

Figure 3.6 Plot of the reductive peak area from cyclic voltammetry of photolyase on a 29 bp T□T dsDNA modified electrode under different magnetic field conditions. The presence of absence of an applied field during the reduction of photolyase did not have any measurable effect on the amount of charge transferred at later time points. The presence or absence of a magnetic field when the photolyase is incubated with the dsDNA surface is what determines the magnitude of the yield.

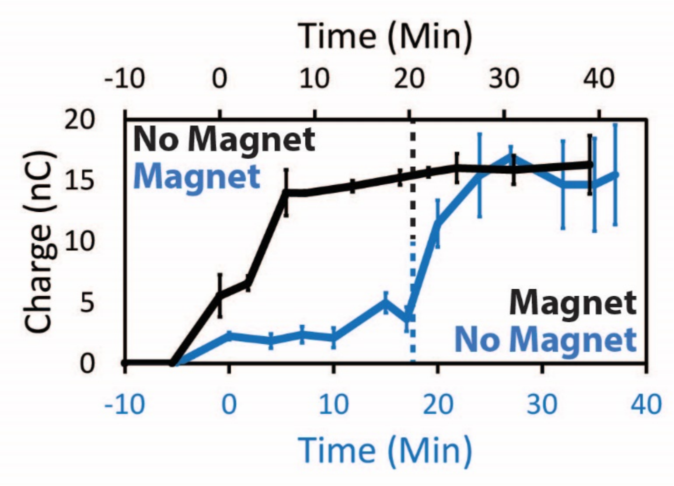

Figure 3.7 Total amount of charge transferred over time with varying magnetic field conditions. First, 50 µM photolyase was added to a monolayer of 29 bp dsDNA with T□T and irradiated with blue light (t=0) in the absence (black) or presence (blue) of a 30 Gauss magnetic field applied perpendicularly up intersecting the plane of the electrode. At the time indicated by the dotted line the magnetic field was either applied (black) or removed (blue) to switch the magnetic field conditions in a given experiment. The time was plotted differently on the two x-axis so this switch is visually aligned for the two experiments.

Figure 3.8 illustrates how the repair efficiency varies with magnetic field strength and angle. Significantly, at low magnetic fields, the magnetic field strength plays an important role in the efficiency of dimer repair. The background magnetic field during our experiments was measured to be 0.4 G and resulted in the highest yield of repair. However, applying an additional magnetic field perpendicular to the surface as weak as 0.2 G results in diminished yield. Increasing the field strength further decreases the yield but eventually the effect is saturated; applied fields of 30 G and 6000 G fields result in the same magnitude decrease in yield.

Moreover, the angle of the magnetic field relative to the plane of the electrode significantly influences the yield. A magnetic field perpendicular to the plane of the electrode exhibits the largest effect. Changing the angle of inclination to 45 degrees diminishes the effect, as does applying a field parallel to the plane of the surface. Interestingly, there is no difference in yield observed for a magnetic field pointing perpendicularly up versus perpendicularly down (Figure 3.9), which suggests that only the angle of the field and not the polarity direction of the field is important. The redox potential of the flavin lies negative of the potential of zero charge of the working electrode. At this potential the duplexes line up approximately normal to the electrode surface, meaning that the thymine dimers are approximately parallel to the surface (16). The largest magnetic field effect occurs when the field intersects the dimer perpendicular to the plane of the bases and the weakest effect occurs when the field is parallel to the plane of the bases.

These results clearly illustrate that the CPD reaction is sensitive to low magnetic fields and field direction. These results are reminiscent of experiments carried out by

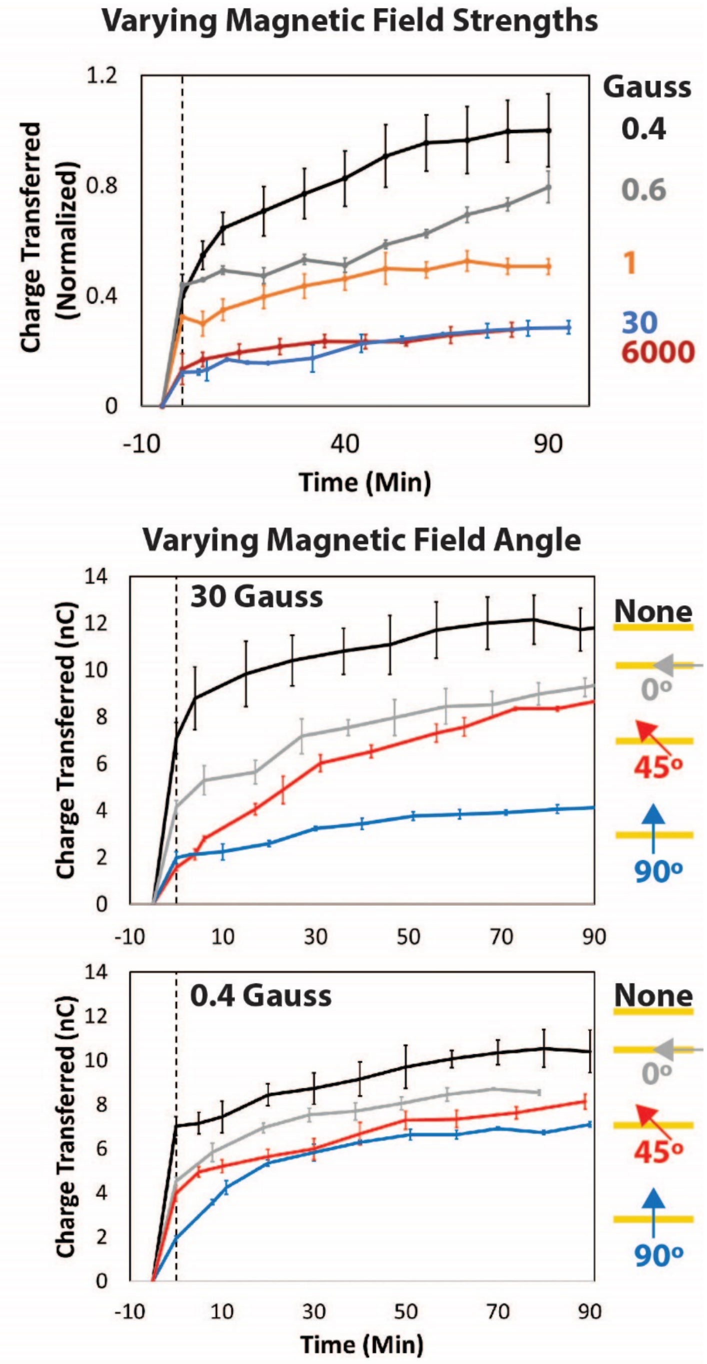

Figure 3.8 Total amount of charge transferred over time with varying magnetic field strengths (top) and angles (bottom) with photolyase bound to DNA-modified electrodes and irradiated with blue light. 50 µM photolyase was added to a monolayer of 29 bp dsDNA with T□T and irradiated with blue light (t=0). (Top) The background magnetic field with none applied was 0.4 Gauss, and the applied field was added to this to give the total field strength listed to the right of the plot. The magnetic field was applied perpendicularly up intersecting the plane of the electrode surface. The magnetic field angle was varied by applying a 30 Gauss field (middle) or 0.4 Gauss field (bottom) at either a 0°, 45°, or 90° angle relative to the plane of the electrode surface.

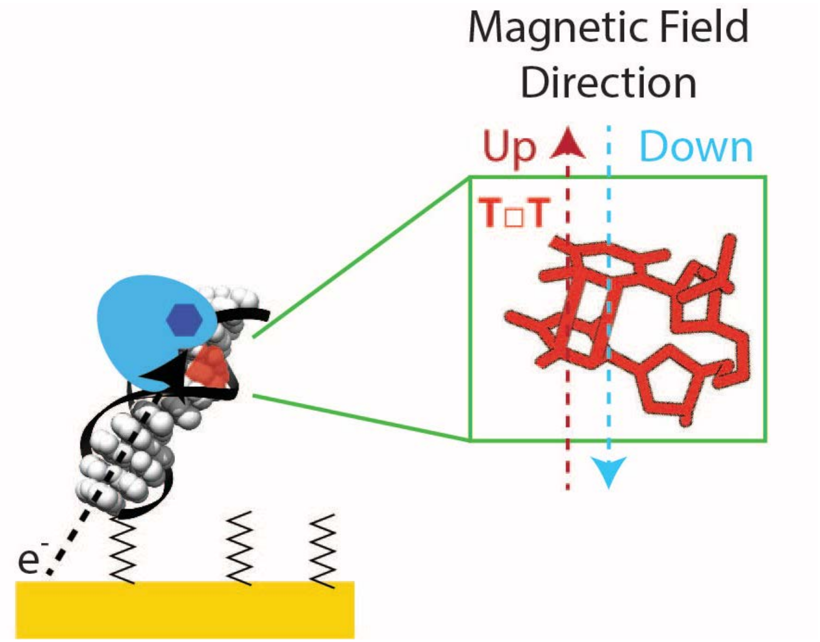

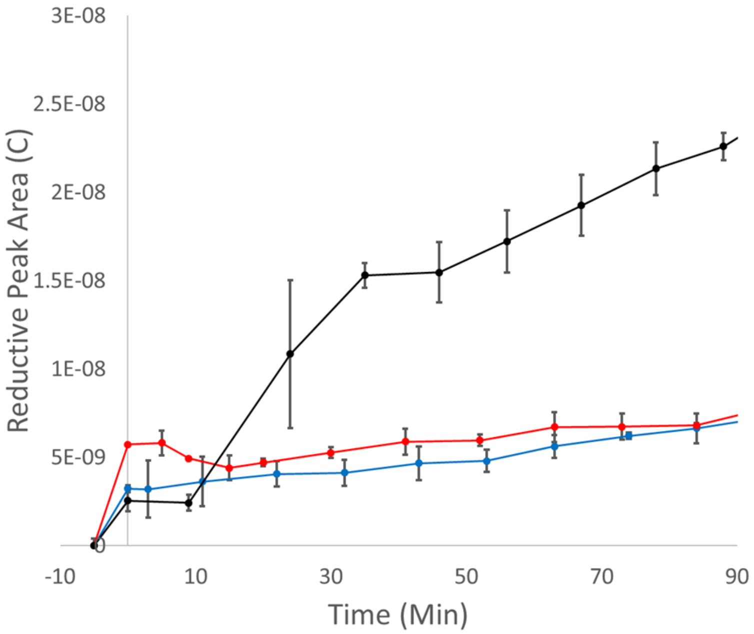

Figure 3.9 Effect of a magnetic field intersecting the electrode surface with the same angle and opposite polar direction. (Top) Cartoon showing the magnetic field that is applied perpendicular to the electrode surface and how it is expected to intersect the thymine dimer. (Bottom) Applying a magnetic field of 30 Gauss perpendicularly up (red) or down (blue) intersecting the plane of the electrode did not have a measurable difference from one another. In both cases the magnetic field decreased the signal compared to a control with no applied field (black).

N.J. Turro, who established conditions critical for observation of striking effects in the presence of weak magnetic fields. What is required is a competition between two processes: one that is magnetic field-dependent, the other is magnetic field-independent (9). Figure 3.10 illustrates the CPD repair reaction carried out by photolyase. Here there are magnetic field-independent and dependent pathways in competition in photolyase repair of CPDs, which allows a magnetic field to change how much of CPD is repaired or left intact.

To examine this competition in more detail, we tested mutants of photolyase that perturb internal electron transfer pathways. In particular, we would expect steps that affect the lifetime of the CPD radical pair, which should be highly sensitive to the presence of a magnetic field, to be most perturbed. Multiple photolyase active site mutants were previously characterized using ultrafast spectroscopy to determine the rates of electron transfer and bond breaking steps in CPD repair in the absence of a magnetic field (10). The mutant N378C interacts with the flavin and displays slow forward electron transfer from the flavin to the dimer and only slightly reduced electron return from the thymine radical to the flavin. M345A interacts with both the dimer and the flavin and shows increased rates for forward electron transfer and electron return. E274A also interacts with both the flavin and the dimer and has faster electron return but slower forward electron transfer. Shown in Figure 3.11, we find that both of the mutations near the dimer eliminate magnetosensitivity. In contrast, the N378C mutant retains magnetosensitivity despite having a destabilized flavin radical, which has its redox potential shifted -100 mV relative to WT (Figure 3.12). The magnetosensitivity of these

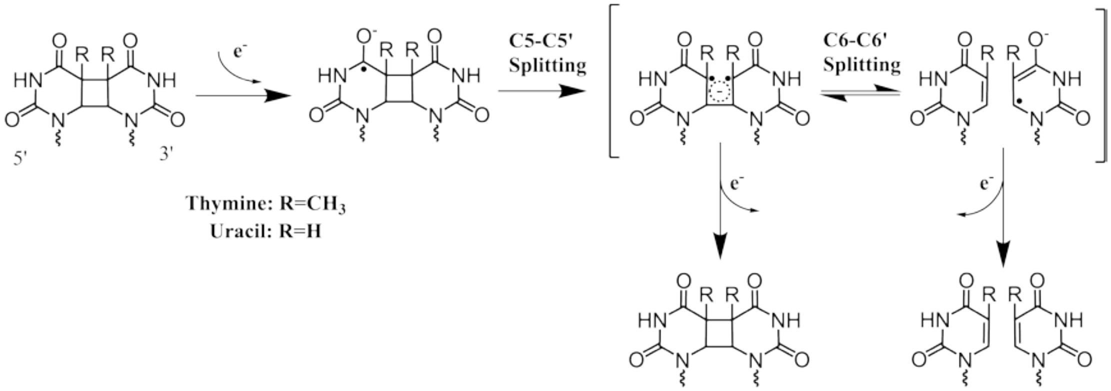

Figure 3.10 Radical repair scheme for cyclobutane pyrimidine dimers (CPD). Forward electron transfer from the fully reduced flavin results in a radical residing on the CPD. First the C5-C5' bond splits, followed by either C6-C6' bond splitting or futile back electron transfer to the CPD state. Following bond splitting the radical residing on the pyrimidine can either undergo electron return to the flavin, resulting in the completion of the repair process, or the radical can facilitate CPD formation and undergo futile back electron transfer.

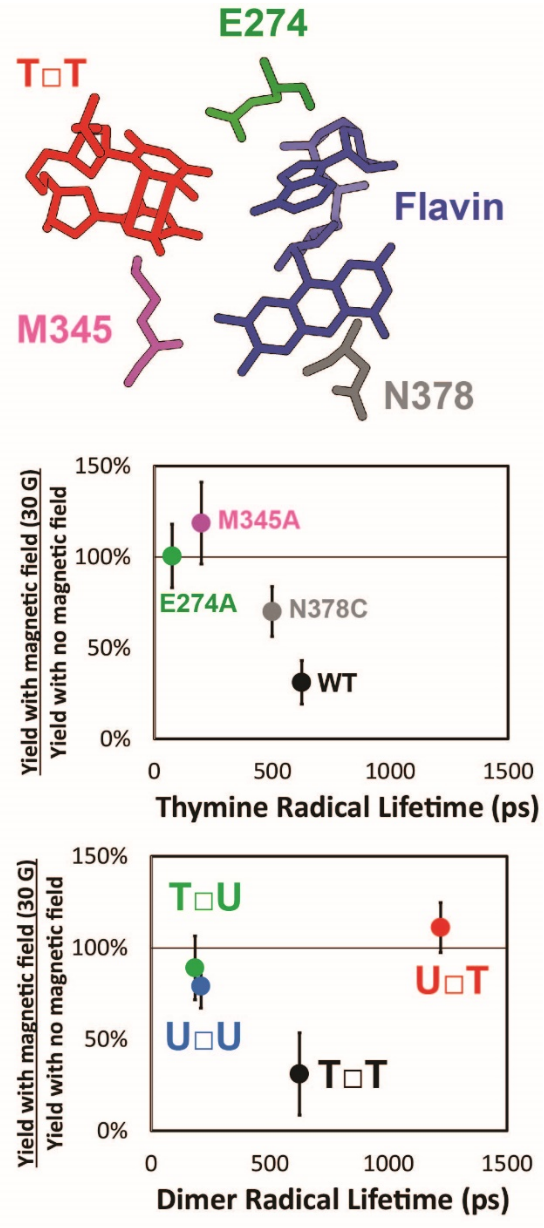

Figure 3.11 Effect of structural perturbations on magnetosensitivity of photolyase. (Top) Cartoon showing placement of thymine dimer relative to flavin cofactor and three active site residues in photolyase. (Middle) Comparison of the yield of charge transferred to different active site mutants with and without 30 Gauss magnetic field perpendicularly intersecting the plane of the electrode surface after 60 minutes of irradiation with blue light. (Bottom) Comparison of the yield of charge transferred to different cyclobutane pyrimidine dimers with and without 30 Gauss magnetic field perpendicularly intersecting the plane of the electrode surface after 60 minutes of irradiation with blue light. For these dimers U=uracil, T=thymine, and the 5' position is listed first with the 3' position second. These data suggest that the lifetime of the thymine dimer radical is tuned to be properly influenced by a magnetic field and that the lifetime is not too long like the UT, or too short like with TU and UU. Lifetimes of mutant radicals were obtained from (*10*) and dimer radical lifetimes were obtained from (*11*)

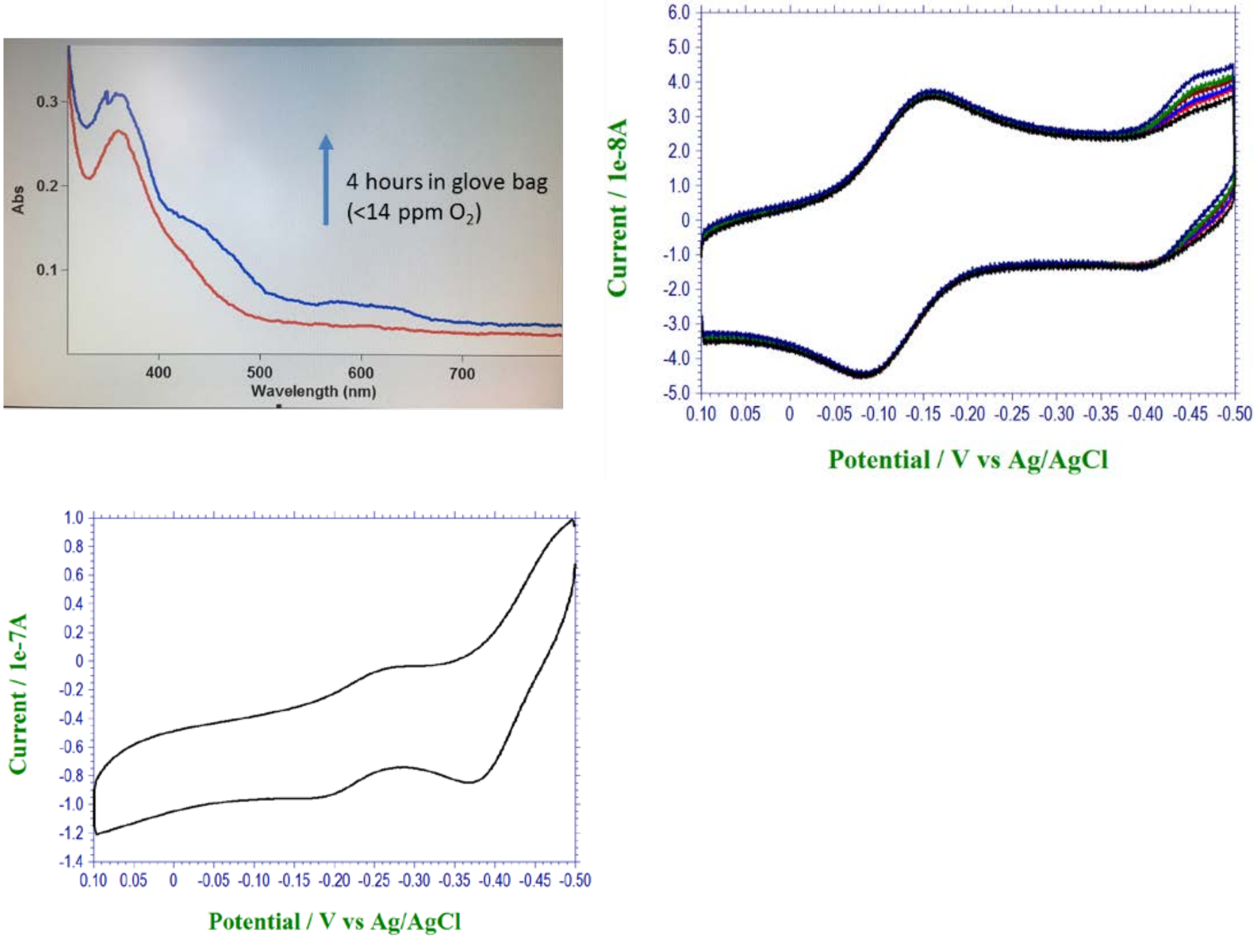

Figure 3.12 Ultraviolet/visible wavelength spectra and cyclic voltammetry of photolyase upon oxidation. Small amounts of oxygen resulted in oxidation of the flavin in the photolyase. (Top left) This oxidation could be measured by observing the change in UV/Vis spectra. (Top right) The oxidized, deprotonated flavin also had a corresponding redox peak associated with it that formed centered around -420 mV vs AgCl/Ag. All photolyase mutants had similar redox potentials as the WT protein except for N378C (bottom left), which had a negatively shifted fully reduced state centered around -220 mV, and a slightly positively shifted deprotonated state.

mutants correlates with slower electron return and does not correlate with forward electron transfer or quantum yield of CPD repair.

Repair of uracil-containing dimers further reveal the underlying cause of magnetosensitivity. In these experiments the repair of T□T, U□T, T□U, and U□U dimers were monitored with and without an applied magnetic field and are presented in figure 3.11. The U□U dimer has diminished but significant magnetosensitivity. Both the U□T and T□U dimers show no observable magnetosensitivity, despite the T□U having a radical life time on par with the U□U and the U□T having a longer radical lifetime than any of the other CPD. Together these data argue that perturbation in the uracil/thymine radical pairs most affect the magnetosensitivity of CPD repair.

These data thus allow us to pinpoint the likely source of magnetosensitivity in photolyase repair: the pyrimidine dimer. Active site mutations near the CPD as well as changes in the CPD structure eliminate magnetosensitivity, but the N378C mutation near the flavin and away from the CPD retains magnetosensitivity. The crucial condition for observation of magnetic field effects is a competition between two processes, and the magnetic field changes their relative favorability (9). Illustrated in Figure 3.10, our data show the competition to either maintain or repair the CPD that is shifted towards maintenance with an externally applied magnetic field. The magnetosensitive chemistry likely occurs after the C5-C5’ splitting, because there is a competition between C6-C6’ splitting that results in repaired CPD and futile back electron transfer that maintains the CPD (10). Rapid singlet-triplet interconversion, as has been observed in biradical species, could change the favorability of bond cleavage versus reformation and lead to a magnetic field maintaining the CPD (11b). A second competition occurs after the C6-C6’ splitting because the radical resides on one of the pyrimidines long enough that it may recreate the dimer before it safely returns to the flavin (10,12). However, the limited influence of the N378C mutant on magnetosensitivity suggests this second process is unlikely to be the relevant source of competition.

The extraordinary magnetosensitivity of CPD repair by photolyase has intriguing relevance to magnetoreception by cryptochromes, which are viewed as candidates for radical-pair magnetoreceptors, and are structurally quite similar to photolyase (1,13). Many features of the photolyase homology region (PHR) are conserved in both photolyase and cryptochrome; however cryptochromes are generally classified by their inability to repair CPD lesions (13). Explanations for this discrepancy range from structural differences in the domains to the possibility that their inability to repair CPD is reliant on special conditions (13). In cryptochromes, the presence of C-terminal extensions block the DNA binding pocket and could prevent observation of CPD repair except under conditions where they are released (14). No crystal structure of cryptochromes that are involved in magnetosensitive behavior exist; however both a crystal structure of Arabidopsis CRY1 PHR domain and a model of Arabidopsis CRY2 PHR show partial conservation of the positively charged groove of photolyase that could allow for DNA to associate with the active site if the C-terminal extension were released from this region (15). It is important to note also that Arabidopsis CRY2-GFP fusion proteins bind to chromosomes within mitotic cells (10).

Truncated Arabidopsis thaliana cryptochrome 1 without the C-terminal extension (*at*CRY1ΔC) was tested for DNA binding and CPD repair in the presence and absence of an applied magnetic field. First *at*CRY1ΔC was incubated with dsDNA containing T□T and irradiated with blue light in aqueous solution. HPLC of the DNA before and after incubation show that *at*CRY1ΔC repairs T□T similar to *ec*PL (Figure 3.13). When the cryptochrome is added to a monolayer of duplex DNA, each containing a TT dimer in the absence of an applied magnetic field, irradiation with blue light leads to the increase in current for the FAD redox couple (Figure 3.14). Shining light on an identical monolayer in the presence of an applied magnetic field, however, leads to a significant reduction in the yield of charge transferred over the same period of time, consistent with the change observed for photolyase. The diminished signal on the electrode modified with DNA without thymine dimers shows that *at*CRY1ΔC is preferentially binding to the CPD lesion. Consistent with the experiments on photolyase, the angle of the magnetic field relative to the plane of the electrode significantly influences the yield of repair by cryptochrome (Figure 3.15). A magnetic field perpendicular to the plane of the electrode exhibits the largest effect. Changing the angle of inclination to 45 degrees diminishes the effect, as does applying a field parallel to the plane of the surface.

These experiments illustrate how nature can design a magnetic field compass that functions at weak field strengths. Weak magnetic fields significantly affect the repair of CPD lesions by *E. coli* photolyase and *A Thaliana* cryptochrome. This magnetosensitivity is dependent on the magnetic field strength and direction. Experiments with photolyase active site mutants and uracil-containing lesions show that the chemistry involved in the repair of CPD is the likely source of magnetosensitivity that we observe.

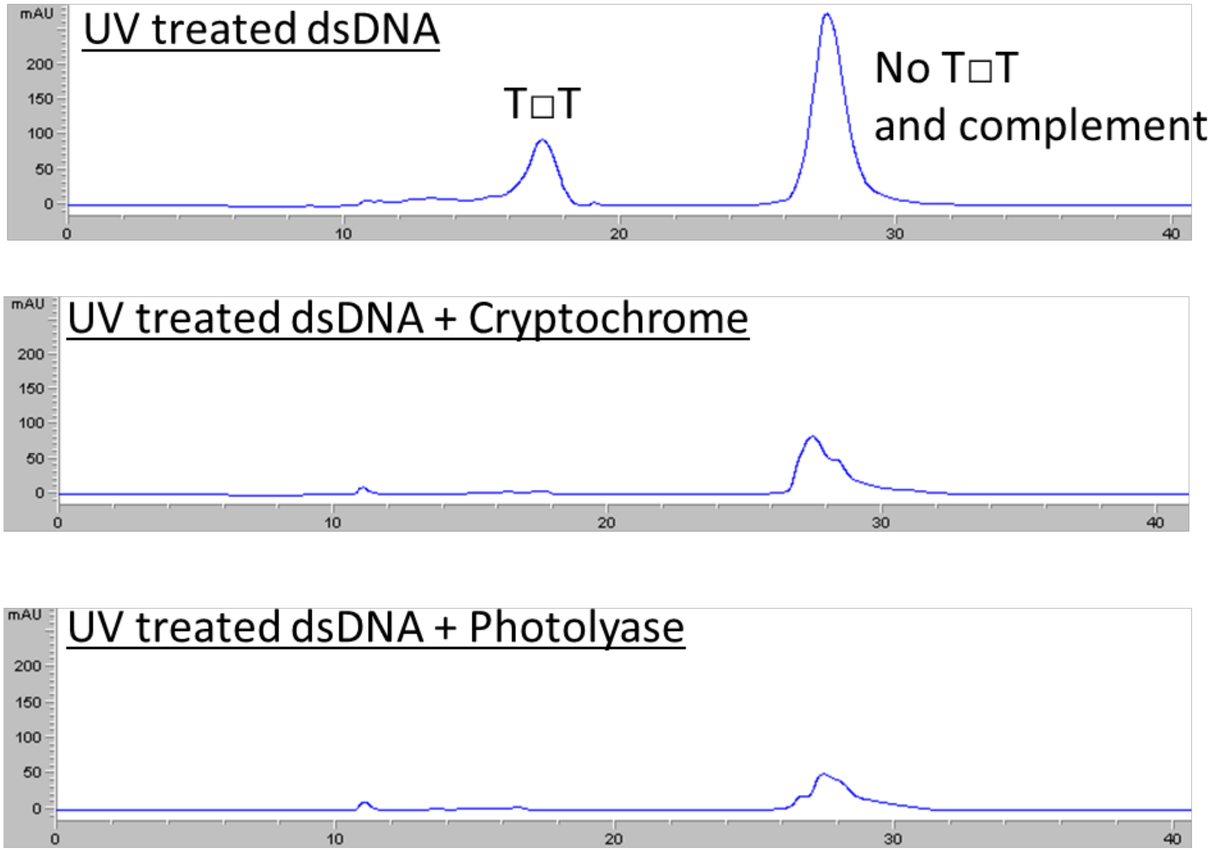

Figure 3.13 High pressure liquid chromatography traces of duplex DNA eluted at high temperature. Three different samples were eluted: duplex DNA containing a thymine dimer before (top) and after incubation with cryptochrome (mid) and photolyase (bottom). The column was kept at 80^{o}C to dehybridize the two strands. The strand containing the thymine dimer , T□T, elutes at 17 minutes. The strand with the repaired dimer as well as the complementary strand elute at 27-28 minutes. Irradiating 50 µM cryptochrome or 50 µM photolyase for 1 hour with 35 µM duplex DNA leads to a complete loss of the peak with the thymine dimer as well as the presence of a new peak that co-elutes with the complement, together indicating that the thymine dimer is being repaired.

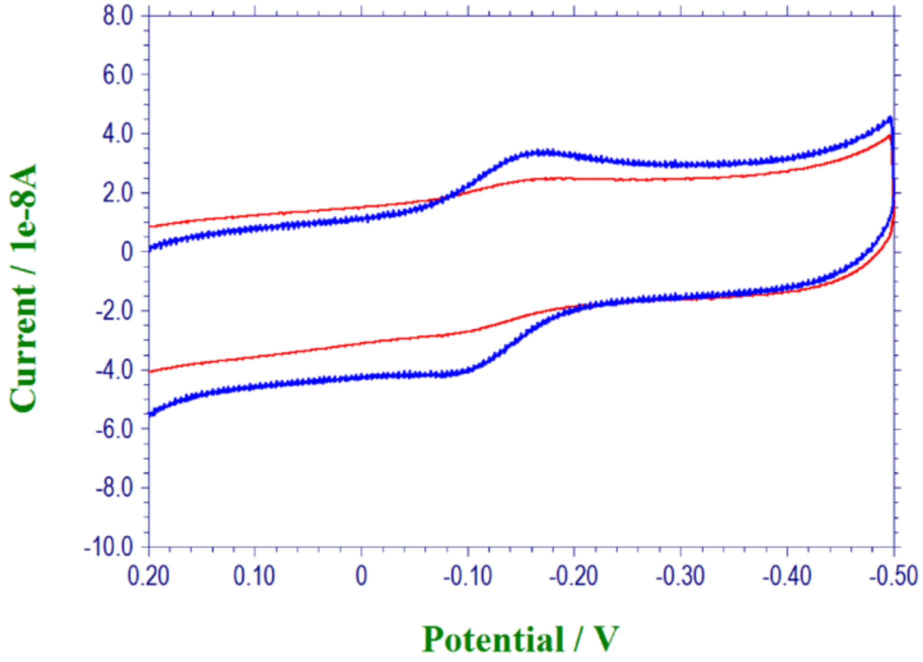

Figure 3.14 Cyclic voltammogram of cryptochrome incubated in a duplex DNA-modified electrode. 50 µM cryptochrome was incubated on a duplex DNA-modified electrode with (blue) and without (red) a single thymine dimer. In both cases the cryptochrome was irradiated with blue light (405 +/- 10 nm, <30 mW) from a diode laser pointer for one hour before addition to a 29 bp dsDNA monolayer. The above cyclic voltammogram was taken after 90 minutes' incubation of cryptochrome on the DNA-modified electrode with constant blue light irradiation.

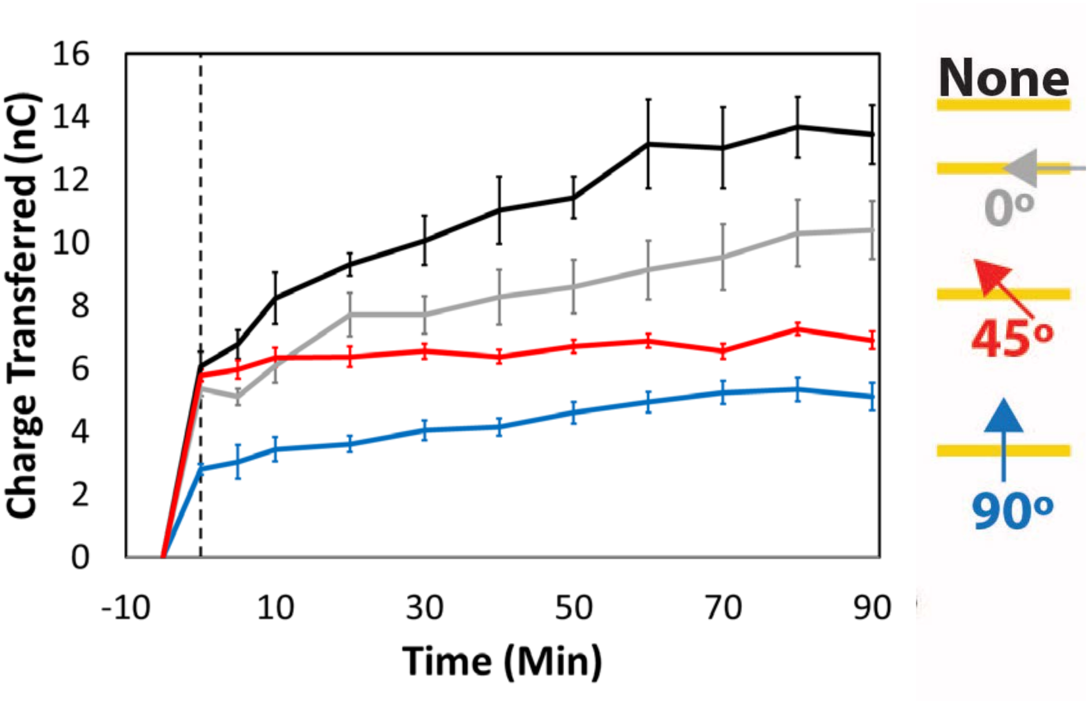

Figure 3.15 Total amount of charge transferred to the flavin of cryptochrome over time with varying magnetic field angles. 50 µM cryptochrome was added to a monolayer of 29 bp dsDNA with T□T and irradiated with blue light (t=0). An increase in total amount of charge transferred indicates the repair of the T□T, which allows for more efficient charge transport to the cryptochrome flavin. The background magnetic field with none applied was 0.4 Gauss, and the applied field was added to this to give the total field strength of 30 Gauss. The magnetic field angle was varied by applying the magnetic field at either a 0^{o}, 45^{o}, or 90^{o} angle relative to the plane of the electrode surface.

These data suggest that the PHR active site is able to facilitate a delicately balanced competition between two reaction pathways that can be influenced by weak magnetic fields. It is intriguing to consider how this chemistry may be used *in vivo* to inform magnetoreceptive behavior.

References

1)W. Wiltschko, R. Wiltschko "Magnetic orientation and magnetoreception in birds and other animals" *J Comp Physiol A Neuroethol Sens Neural Behav Physiol.* **2005**, 191(8), 675-693.

2) P.J. Hore, H. Mouritsen "The Radical-Pair Mechanism of Magnetoreception" *Annu. Rev. Biophys.* **2016**, 45, 299-344.

3) S. Weber "Light-driven enzymatic catalysis of DNA repair: a review of recent biophysical studies on photolyase" *Biochim. Biophys. Acta* **2005**, 1707, 1-23.

4) K. Maeda, A.J. Robinson, K.B. Henbest, H.J. Hogben, T. Biskup, M. Ahmad, E. Schleicher, S. Weber, C. R. Timmel, P.J. Hore "Magnetically sensitive light-induced reactions in cryptochrome are consistent with its proposed role as a magnetoreceptor" *Proc. Nat. Acad. Sci.* **2012**, 109, 4774-4779.

5) M.C. DeRosa, A. Sancar, J.K. Barton "Electrically monitoring DNA repair by photolyase" *Proc. Nat. Acad. Sci.* **2005**, 102, 10788-10792.

6) J.C. Genereux, J.K. Barton "Mechanisms for DNA Charge Transport" *Chem. Rev.* **2010**, 110 (3), 1642-1662.

7) A. Sancar "Structure and function of DNA photolyase and cryptochrome blue-light photoreceptors" *Chem. Rev.* **2003**, 103 (6), 2203-2238.

8) J. D. Slinker, N. B. Muren, A. A. Gorodetsky, and J. K. Barton "Multiplexed DNA-Modified Electrodes" *J. Am .Chem. Soc.,* **2010**, *132* (8), 2769-2774

9) I.R. Gould, N.J. Turro, M.B. Zimmt "Magnetic field and magnetic isotope effects on the products of organic reactions" *Adv. Phys. Org. Chem.* **1984**, 20, 1-53.

10) C. Tan, Z. Liu, J. Li, X. Guo, L. Wang, A. Sancar, D. Zhong "The molecular origin of high DNA-repair efficiency by photolyase" *Nat. Comm.* **2015**, 6, 7302.

11) Z. Liu, L. Wang, D. Zhong "Dynamics and mechanisms of DNA repair by photolyase" *Phys. Chem. Chem. Phys.* **2015**, 17, 11933

11b) A. G. Griesbeck, H.M. Mauder, S. Stadtmuller "Intersystem crossing in triplet 1,4-biradicals: conformational memory effects on the stereoselectivity of photocycloaddition reactions" *Acc. Chem. Res.* **1994**, 27, 70-75.

12) M.A. Huels, B. Boudaiffa, P. Cloutier, D. Hunting. L. Sanche."*Single, double, and multiple double strand breaks induced in DNA by 3-100 eV electrons*." *J. Am. Chem. Soc.***2003**, 125, 4467–4477.

13) M. Müller, T. Carell "Structural biology of DNA photolyases and cryptochromes" *Curr. Opin. Struct. Biol.* **2009**, 19 (3), 277-285.

14) N. Ozturk, C. P. Selby, D. Zhong, A. Sancar "Mechanism of photosignaling by drosophila cryptochrome" *J. Biol. Chem.* **2014**, 289 (8), 4634-4642.

15) X. Yu, H. Liu, J. Klejnot, C. Lin "The cryptochrome blue light receptors" *Arabidopsis Book* **2010**, 8, e0135.

16) S.O. Kelley, J.K. Barton, N.M. Jackson, L.D. McPherson, A.B. Potter, E.M. Spain, M.J. Allen, M.G. Hill "Orienting DNA helices on gold using applied electric fields" *Langmuir* **1998**, 14, 6781.

17) P.F. Heelis, G. Payne, A. Sancar, "Photochemical properties of Escherichia coli DNA photolyase: selective photodecomposition of the second chromophore" *Biochemistry* **1987,** *26*, 4634-4640.

18) N. Ozturk, Y.-T. Kao, C. P. Selby, I. H. Kavakli, C. L. Partch, D. Zhong and A. Sancar. "Purification and characterization of a type III photolyase from *Caulobacter crescentus*." *Biochemistry* **2008**, *47*, 10255.

Chapter 4

DNA-mediated signaling by proteins with 4Fe-4S clusters studied by electrochemistry and atomic force microscopy

Partially adapted from Grodick, M.A.; Segal, H.M.; Zwang, T.J.; and Barton, J.K. *J. Am. Chem. Soc.* **2014**, *136* (17), 6470-6478

M.A. Grodick isolated DinG and EndoIII and performed electrochemistry experiments. T.J. Zwang performed atomic force microscopy experiments, modeling, and analysis.

Introduction

Iron-sulfur clusters are increasingly being found in proteins that are tasked with maintaining the fidelity of the genome (1-3). These clusters were first observed in DNA-binding proteins in the base excision repair (BER) glycosylase, Endonuclease III (EndoIII) (4). More recently, 4Fe-4S clusters have been found in a range of DNA repair and DNA-processing enzymes including helicases, DNA polymerases, RNA polymerases, DNA helicase-nucleases, and DNA primases from across the phylogeny (2, 4-13). Many of the enzymes that have been shown to contain these clusters are genetically linked to human diseases, such as early onset breast cancer and Fanconi's anemia, yet the proteins perform immensely different functions. The clusters do not participate in catalysis in these proteins (2,3,5), though DNA binding may be affected by perturbing the cluster (14). Recently, studies focusing on the biogenesis of iron-sulfur clusters have revealed that disruption of iron-sulfur cluster assembly proteins in eukaryotic cells leads to nuclear genomic instability and defects in DNA metabolism, replication, and repair (15-17). The ubiquity of these complex cofactors suggests an essential and shared role for their presence in DNA processing enzymes.

We have considered that the 4Fe-4S clusters in DNA repair enzymes may serve as redox cofactors, much as 4Fe-4S clusters do in other enzymes within the cell (1,18). Most of our work has focused on EndoIII from *Escherichia coli*, where the 4Fe-4S cluster was first found. Although a redox role for the cluster was considered (4), the 4Fe-4S cluster in EndoIII is redox-inactive at typical cellular potentials. We showed, however, that DNA binding shifts the redox potential of the cluster -200 mV to 80 mV vs. the normal hydrogen electrode (NHE), moving the 3+/2+ redox couple into the physiological regime

(19). Strikingly, we have now seen that 4Fe-4S clusters in other repair proteins share this DNA-bound potential of ~80 mV versus NHE (20, 21). We have proposed that these clusters are utilized for DNA-mediated charge transport (CT) chemistry as a first step in the search for DNA lesions to repair (18, 22). Indeed we have explored how EndoIII and another BER glycosylase with a 4Fe-4S cluster, MutY, may use DNA CT cooperatively as a first step in repair (22). Here we explore how DNA CT may be utilized more generally in *E. coli* for inter-protein signaling between repair pathways to maintain the integrity of the genome.

The chemistry of DNA CT offers a powerful tool to probe the integrity of duplex DNA. It has now been well documented that DNA can conduct charge through the π-stacked base pairs within the helix (23). Subtle perturbations to the DNA base stack, including the presence of base pair mismatches, abasic sites, or even DNA lesions, such as those that are substrates for DNA glycosylases, attenuate DNA CT (18,24). Protein binding can also interrupt DNA CT if it disrupts base stacking, as seen with enzymes that flip DNA bases out of the helix (25). This CT chemistry has been used to develop electrochemical sensors that detect base lesions, mismatches, and DNA-binding proteins on DNA-modified electrodes (18, 25-27). Charge can be transported through DNA over long molecular distances, and the distance dependence of CT is quite shallow (23). In fact, charge can be efficiently transported through at least 100 base pairs, and over this distance the rate is still limited by transport through the linker rather than the DNA base stack (28,29). Given that DNA CT can occur over long molecular distances and can be modulated by DNA-binding proteins, does DNA-mediated CT play a general role within the cell?

Recently DinG, a DNA damage response helicase from *E. coli*, was shown to contain a 4Fe-4S cluster (30). DinG is part of the SOS response, which is activated by DNA damaging agents and cellular stressors. DinG shares homology with the nucleotide excision repair protein XPD as well as with a host of Superfamily 2 helicases from archaea and eukaryotes that are linked to human disease and share a conserved 4Fe-4S domain (5). DinG unwinds DNA that has single-stranded overhangs with a 5′ to 3′ polarity (31). DNA-RNA hybrid duplexes that form within a DNA bubble, termed R-loops, represent a unique substrate that DinG has been shown to unwind *in vitro* (32). Importantly, DinG is required to unwind R-loops *in vivo* in order to resolve stalled replication forks and thus to maintain the integrity of the genome (33). Here we examine the DNA-bound redox properties of DinG and explore more generally crosstalk among redox-active DNA-processing enzymes in *E. coli* via 4Fe-4S clusters.

Materials and methods

Expression and Purification of DinG. The *dinG* gene was amplified from *E. coli* and was inserted into a pET-28 b (+) vector (Novagen) as described previously (30). After the vector was isolated, the cloned *dinG* gene was sequenced (Laragen) using the primers listed in Table 4.1. An aliquot of BL21(DE3) competent cells (Invitrogen) was then transformed with the pET28b-*dinG* vector. The constructed pET28b-*dinG* vector encodes for DinG with a C-terminal hexahistidine affinity tag.

To express DinG, six liters of LB, which had been inoculated with an overnight culture of BL21(DE3) cells harboring the pET28b-*dinG* vector, were shaken at 37 °C. After the cultures reached an O.D. of ~0.6-0.8, enough IPTG (Research Products

International Corp.) was added to bring the concentration of IPTG in each flask to 150 µM. The flasks were then returned to the incubator, which had been cooled to ~22 ° C. After ~16 hours of IPTG induction at ~22° C, the cells were collected by centrifugation at 5,500 rpm for 15 minutes. The cell pellets were frozen at -80 ºC.

To purify DinG, the cell pellets were resuspended in 300 mL buffer A (20 mM Tris-HCl, 8.0 pH at 4 ºC, 0.5 M NaCl, and 20% glycerol) with added DNaseI from bovine pancreas (10 kU, Sigma) and Complete Protease Inhibitor Cocktail Tablets (Roche). The cells were lysed using microfluidization. The lysate was centrifuged at 12,000 rpm for 45 minutes, and the supernatant from the cell lysate was filtered and loaded onto a 5 mL Histrap HP (GE healthcare) nickel-affinity column that had been equilibrated with buffer A. The column was then connected to an ÄKTA FPLC (fast protein liquid chromatography, GE healthcare) and was washed with 3-5 column volumes (CV) of buffer A. The protein was eluted using a linear gradient from 0-20% buffer B (20 mM Tris-HCl, 8.0 pH at 4 ºC, 0.5 M NaCl, 500 mM imidazole, and 20% glycerol) over 10 CV, followed by a linear gradient from 20-30% buffer B over 10 CV. Fractions containing the desired protein, which were yellow and eluted at ~150 mM imidazole, were desalted into buffer C using a Hiprep 26/10 desalting column (GE healthcare). The collected protein was then concentrated down to 10-13 mL using an Amicon Ultra-15 centrifigual filter unit (Millipore) and was loaded onto a Hiload Superdex 200 26/600 pg (GE healthcare) that had been equilibrated with buffer C. The protein eluted after ~180 mL of buffer C (20 mM Tris-HCl, 8.0 pH at 25 ºC, 0.5 M NaCl, and 20% glycerol) had passed over the column. The purity of the protein was confirmed using SDS-PAGE

(Figure 4.1). A helicase activity assay for DinG, modified from previously published procedures, was used to show that the protein is active after purification (30,32).

DNA-modified DinG Electrochemistry. The DNA substrate used for the electrochemical characterization of DinG was either a well-matched 20-mer DNA oligomer with a 15-mer 5′ to 3′ single-stranded overhang or the same substrate with the exception of an abasic site being placed on the complementary strand four base pairs from the bottom of the duplex (Table 4.1). A 20-mer strand of DNA with a terminal thiol and 6-carbon linker at the 5′ end of the strand was annealed to a 35-mer unmodified strand of DNA to yield the electrochemical substrate. The electrochemical substrate was designed to be competent to unwind by DinG in a helicase reaction. Single-stranded DNA stimulates the ATPase activity of DinG, which requires at least a 15-mer single-stranded 5′ to 3′ overhang in order to unwind DNA substrates *in vitro* (32). In the electrochemical cell, the DNA substrate is covalently tethered to the gold surface via a gold-thiol bond.

The thiol-modified strand was synthesized on a 3400 Applied Biosystems DNA synthesizer using standard phosphoramidite chemistry. The complementary strands were purchased from IDT. All phosphoramidites, including the terminal phosphoramidite containing a 6-carbon disulfide linker were purchased from Glen Research. The thiol-modified and complementary strands were purified by HPLC using an analytical C-18 column (Agilent). DNA strands were characterized by MALDI mass-spectroscopy. The DNA was quantified by UV-Visible absorbance and equimolar amounts were annealed, yielding the duplex substrate.

Figure 4.1 SDS-PAGE gel for purification of DinG. Lanes are referred to as 1 to 8 from left to right. The lanes contain an SDS-PAGE weight standard-low range (Biorad) (Lane 1), the supernatant from the cell lysate (lane 2), the pellet from the cell lysate (lane 3), the filtered cell lysate (lane 4), the the Histrap HP column flow-through (lane 5), the collected fractions from the Histrap HP column (lane 6), the collected fractions from the Superdex 200 column (lane 7), and a 10x dilution of the stored protein after thawing (lane 8). Corresponding molecular weights for each of the six bands in the weight standard lane are designated to the left of the image.

Table 4.1 Oligonucleotides for electrochemistry substrates, gene replacements, sequencing or colony PCR, and site-directed mutagenesis

Note: All oligonucleotides except for the modified strand for electrochemistry were purchased from IDT

Designation and use	**Sequence (5' to 3')** (bases highlighted in red yield the point mutation after SDM)
Primer for cloning *dinG* forward	GGTTTTCCCATGGCATTAACCGCC
Primer for cloning *dinG* reverse	CATCATTAAAGCTTCCGACGGCGT
pET28b-*dinG* insert sequencing forward 1	T7 promoter primer
pET28b-*dinG* insert sequencing forward 2 (within gene)	ACTGACGCCGAACAATCAGGA
pET28b-*dinG* insert sequencing reverse 1	T7 terminator primer
pET28b-*dinG* insert sequencing reverse 2 (within gene)	TTCGGCAAATGACTGTAAGCCCAC
Substrate for electrochemistry – 20-mer thiolated modified strand	HS-C6-GTGCTGCAACGTGTCTGCGC (annealed with either the well-matched complement or abasic complement to yield the substrate used in experiments)
Substrate for electrochemistry – 35- mer complementary strand for well-matched substrate	AGACTGCAGACGAGAGCGCAGACACGTTGCAGCAC
Substrate for electrochemistry – 35- mer complementary strand for abasic substrate	AGACTGCAGACGAGAGCGCAGACACGTTGCA-_CAC ("_" represents an abasic site)
AFM substrates	3.8 kb long strands and 1.6 or 2.2 kb shorts strands were prepared as described previously (22, 35)
Δ*dinG*::cm^{R}, forward primer	CCGAAAAATGCCACAATATTGGCTGTTTATACAGTATTTCAGGTTTTCTCGTGTAGGCTGGAGCTGCTTC
Δ*dinG*::cm^{R}, reverse primer	CCGAAAAATGCCACAATATTGGCTGTTTATACAGTATTTCAGGTTTTCTCGTGTAGGCTGGAGCTGCTTC
Δ*dinG*::cm^{R}, sequencing forward	GATGGTGTCTTGCATGACGTG
Δ*dinG*::cm^{R}, sequencing reverse	TCAATACGCCGCCCAACTCA
SDM reverse primer for generation of pBBR1-MCS4 *nth* Y82A	CGATTGGGCTTGCTAACAGCAAAGCAGAAAATATCATCAAAACCTGC
pBBR1MCS-4-*nth* sequencing forward	GGTGCTGATGCCGCTGGCGATTCAG
pBBR1MCS-4-*nth* sequencing reverse	TGTGCTGCAAGGCGATTAAGTTGG
Genomic *nth* region check forward 1	GAGATCCGCATTCCCATTTA
Genomic *nth* region check reverse 1	GGCTTAACGGCGATATGTTC

Table 4.2: Plasmids used in this study

Plasmid Designation	Description	Source, reference, or method to construct
pBBR1MCS-4 or p(empty)	pBBR1MCS-4, a vector for the constitutive expression of genes placed in the MCS (multiple cloning site)	(22)
pBBR1MCS-4-*nth* or p(WT EndoIII)	pBBR1MCS-4 carrying the *nth* gene in the MCS, constitutively expresses WT EndoIII	(22)
pBBR1MCS-4-*nth* D138A or p(EndoIII D138A)	pBBR1-MCS4 carrying the *nth* D138A gene in the MCS, constitutively expresses EndoIII D138A	Site-directed mutagenesis of pBBR1MCS-4-*nth*
pBBR1MCS-4-*nth* Y82A or p(EndoIII Y82A)	pBBR322-MCS4 carrying the *nth* Y82A gene in the MCS, constitutively expresses EndoIII Y82A	Site-directed mutagenesis of pBBR1MCS-4-*nth* using Y82A forward and reverse primers
pET-28b-*dinG*	Overexpresses DinG in presence of IPTG	Insertion of *dinG* amplicon into pET-28b(+) (Novagen) as described above (30)

To prepare DNA-modified single electrodes, a 50 µM solution of the DNA substrate was incubated overnight at ambient temperature on a bare gold on mica surface (Agilent) in an electrochemical cell with a capacity of 50 µL. Following incubation with the DNA solution, the surface was rinsed and backfilled by incubating the electrode with 1 mM 6-mercapto-1-hexanol for 45 minutes at room temperature. Multiplex chip electrodes were prepared as described previously (29, 34). The well-matched electrochemistry substrate was used for all single electrode experiments. For experiments with multiplex chip electrodes, the well-matched and abasic-site substrates were laid down side-by-side in separate quadrants on a single chip (29, 34).

After backfilling, the DNA-modified electrodes were rinsed with the electrochemistry buffer (4 mM spermidine, 4 mM $MgCl_2$, 0.25 mM EDTA, 20% glycerol, 250 mM NaCl, 20 mM tris-HCl, pH ~8.5). Protein concentration was measured by UV-Visible absorbance using an extinction coefficient at 410 nm of 17,000 M^{-1} cm^{-1} (22). An aliquot of 20 µM DinG was flash-thawed by incubating it in a room temperature water-bath. The protein's buffer was exchanged for the electrochemistry buffer by diluting the protein 2-fold into 2x spermidine buffer (8 mM spermidine, 8 mM $MgCl_2$, 1 mM EDTA, 20 mM tris-HCl, pH ~9.0).

Electrochemical measurements were made using a CHI620D Electrochemical Analyzer. For cyclic voltammetry, sweeps within a window from -0.4 V vs. Ag/AgCl to 0.1 or 0.2 V were carried out at a scan rate of 50 mV/s for several hours. For electrochemistry measurements on single electrodes with ATP, 1 mM ATP or 1 mM ATPγS (Sigma) was added after the electrochemical signal grew in to an appreciable size (>20 nA). Cyclic voltammetry was then used to scan the electrode over several hours.

Atomic Force Microscopy Redistribution (AFM) Assay. AFM experiments were performed using a protocol similar to that reported previously with the following modifications (22, 35). The long and short strands of DNA have an identical sequence as they were both amplified off of the pUC19 plasmid with primers containing a 2′ *O*-methyl residue to generate 1.8 and 2.2 kb strands of DNA with 14-mer single-stranded overhangs, so that the two could be subsequently ligated. For well-matched long strands of DNA, the two PCR products were annealed with complementary 14 bp overhangs. For the mismatched long strands of DNA, the strands were annealed in the same way except one of the PCR products contained a 14 bp overhang with a single base changed to yield a C:A mismatch upon the annealing of the 2 strands. Prior to deposition, the protein and DNA solution was incubated at 4 °C for 2 hours. The sample was then deposited (5–10 μL) onto a freshly cleaved mica surface for 2 min, rinsed with 2 mL of water, and dried under argon. The concentration of DinG was 60 nM for AFM experiments with DinG. For AFM experiments with mixtures of DinG and EndoIII or DinG and EndoIII Y82A, the concentration of each protein was 30 nM.

Images of protein and DNA mixtures that had been deposited on dry mica surfaces were gathered using a Bruker Dimension Icon AFM (Beckman Institute MMRC). Images were captured in air with scan areas of $2 \times 2\ \mu m^2$ or $3 \times 3\ \mu m^2$ in soft tapping mode, and a scan rate of 3.00 Hz. RFESPA silicon AFM probes with reflective aluminum backing (Bruker), with a spring constant of 3 N⁄m and a resonance frequency of 69-81 kHz, were used for gathering images.

Bruker nanoscope analysis software was used to measure general DNA contour lengths and height profiles of the proteins. For each dataset, images from at least three independently prepared surfaces were analyzed. At least 50 images were analyzed for both the mismatched DNA-protein samples and the well-matched samples. The binding density ratio, r, is defined as the ratio of the density of proteins bound on the long strands of DNA divided by the density of proteins bound on the short strands of DNA. The density of proteins on each strand is found by dividing the number of proteins by the length of the DNA strands, 3.8 kb pairs for the long strand and 1.9 kb pairs, which is the average length of the short strands, for short strands. Error represents SEM ($n \geq 3$) for each experiment. Distinguishable strands and bound proteins were counted by hand. In order to control for bias, for each experiment, images were randomly assigned identification numbers. The images were then scored blindly. The number of long strands, proteins on long strands, short strands, and proteins on short strands was collected for each image. This was then converted to a binding density ratio for each image.

Binding density ratios can also be calculated for each individual image, which are treated as replicates, to obtain the average binding density ratio for each sample. The binding density ratios were plotted as a histogram (Figure 4.2), which show that the binding density ratios for the two sets of data follow a normal distribution around the mean, allowing for statistical analysis with a two-tailed t-test.

All mutant EndoIII plasmids, which were derived from pBBR1MCS-4 (37) were generated using a QuikChange II Site Directed Mutagenesis kit (Agilent). The pBBR1MCS-4, pBBR1MCS-4-*nth*, The pBBR1MCS-4-*nth* D138A, and pBBR1MCS-4-*nth* Y82A plasmids encode and constitutively express no protein, WT EndoIII, EndoIII D138A, and EndoIII Y82A respectively. The pBBR1MCS-4 derived plasmids are

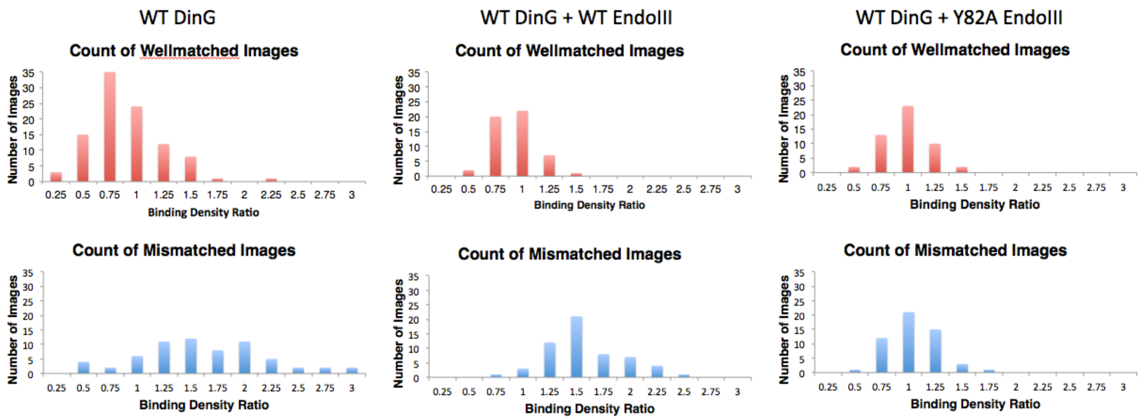

Figure 4.2 Statistical data for the AFM experiments. Histograms showing the distribution of binding density ratios within the population of sample images. The value on the x-axis is the upper range of a .25 unit wide separation, meaning that the column plotted above “1” is the number of images with a binding density ratio between 0.75 and 1.

referred to as p(empty), p(WT EndoIII), p(EndoIII D138A), and p(EndoIII Y82A) respectively throughout the text as indicated in Table 4.2. The p(WT EndoIII) plasmid that was used as the template for the site-directed mutagenesis reactions was previously constructed in our laboratory (35). The primers outlined in Table 4.1 were used to make the p(EndoIII Y82A) and p(EndoIII D138A) mutant plasmids. The isolated plasmids were sequenced (Laragen) using the forward and reverse pBBR1MCS-4-*nth* sequencing primers (Table 4.1) to verify that the desired mutation had been made in the *nth* gene.

Results

DNA binding activates DinG towards reduction and oxidation at cellular redox potentials. DNA-modified electrodes were utilized to explore the DNA-bound redox chemistry of DinG. Cyclic voltammetry of the protein on gold electrodes modified with a 20-mer duplexed DNA oligomer appended with a 15-base 5′ single-stranded overhang displays a reversible redox potential for DinG of 80 mV vs. NHE (Figure 4.3). This DNA-bound potential differs from the midpoint redox potential of ~ -390 mV vs. NHE assigned to the $[4Fe\text{-}4S]^{2+/1+}$ couple of the cluster observed in the absence of DNA as measured by titrations with redox mediators (30). Cyclic voltammetry of DinG on multiplexed electrodes reveals that a single abasic site placed in the DNA duplex attenuates the current by 12 ± 3%, consistent with the signal being DNA-mediated (23, 34). Moreover, upon addition of ATP to DinG bound to DNA-modified electrodes, the reductive and oxidative peak currents markedly increase; ATPγS, which is poorly hydrolyzed, does not yield a significant increase in current (Figure 4.3). Thus, it appears that the ATPase activity of DinG can be monitored electrically, even though ATP hydrolysis is a redox-independent process. Similar results were seen earlier with *S.*

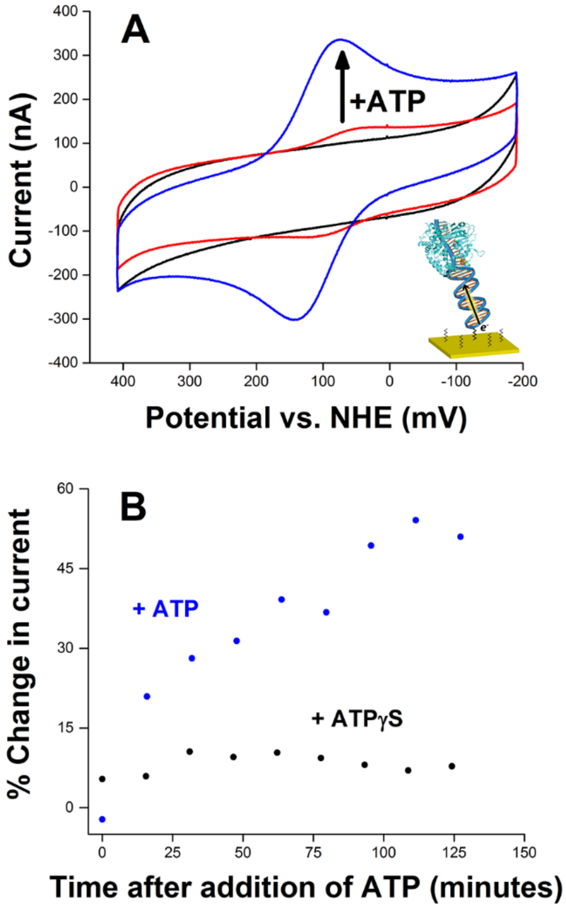

Figure 4.3 Electrochemistry of DinG on DNA-modified electrodes. (A) Cyclic voltammogram of 10 μM DinG (red), DinG after the addition of 5 mM ATP (blue), and buffer only (black) after incubation for three hours. Inset: Cartoon representation of a protein bound to DNA on a DNA-modified electrode. (B) Percent change in current after the addition of 1 mM ATP (blue) or 1 mM ATPγs (black). Percent change in current is the percent increase in the measured current compared to the predicted current, based on the linear growth of the signal with respect to time for the incubation of DinG before the addition of ATP.

acidocaldarius XPD (SaXPD), also an ATP-dependent helicase (21). It is interesting to consider that this electronic signaling of activity may be used within a biological context.

EndoIII and DinG use DNA CT to redistribute to sites of DNA damage.

Given that DinG displays a DNA-bound potential similar to that of EndoIII of ~ 80 mV vs. NHE, we sought to test whether EndoIII and DinG can signal to one another via DNA CT *in vitro* to aid one another in finding lesions that disrupt CT. It is noteworthy that both repair proteins are involved in finding lesions that interrupt DNA CT. Using atomic force microscopy (AFM), we examined whether the DinG helicase would redistribute onto 3.8 kilobase (kb) DNA strands containing a single base mismatch, which interrupts DNA CT, rather than remaining bound to well-matched DNA strands. Our model for how repair proteins utilize DNA CT predicts such a redistribution as a first step in repair (*vide infra*), and this assay provides direct support for the model. If proteins of similar potential carry out DNA CT on well matched DNA strands and dissociate from DNA upon reduction, they should preferentially redistribute onto DNA strands where DNA CT is inhibited by an intervening mismatch. Note that, while a single base mismatch inhibits DNA CT, it is not a substrate for either DinG or EndoIII binding. We have utilized this AFM assay previously to test EndoIII redistribution as a first step in finding damage (22). We have also utilized this assay to test CT signaling between EndoIII and SaXPD, which also contains a 4Fe-4S cluster with a DNA-bound potential of ~ 80 mV vs. NHE, in locating DNA damage (21, 35); these proteins are present in completely distinct organisms, but based on their shared DNA-bound potential are able to signal one another using DNA CT.

In this AFM assay, DNA-protein mixtures are deposited onto a dry mica surface on which single molecules of both free and protein-bound DNA can be visualized (22, 35). Duplexes of DNA that contain a single C:A mismatch located in the middle of the strand are mixed with fully matched DNA. These strands can be distinguished in the AFM by their difference in length: the mismatched strands are ~3.8 kb pairs long while the matched strands on average contain ~1.9 kb pairs (Figure 4.4). They share DNA sequence since the 3.8 kb strands are prepared by ligation of the two shorter strands (22, 35). For mixtures of mismatched long strands and well-matched short strands that are incubated with DinG alone, we find an average of 2.60 ± 0.22 proteins bound per mismatched strand compared to 0.90 ± 0.17 proteins per well-matched strand. We calculate the binding density on the mismatched and matched strands for each independent trial ($n \geq 3$ for each experiment) by normalizing the number of proteins bound by the strand length, to obtain a binding density ratio of 1.44 ± 0.08 favoring the mismatched strand. Thus, even though DinG does not bind preferentially to a mismatch, DNA CT by DinG favors its redistribution onto the strand containing the single base mismatch.

Signaling between EndoIII and DinG was also tested by AFM. In 1:1 mixtures of DinG and wild-type (WT) EndoIII, a binding density ratio of 1.32 ± 0.04 favoring the mismatched strand is observed (Figure 4.4). But does this redistribution depend upon DNA CT?

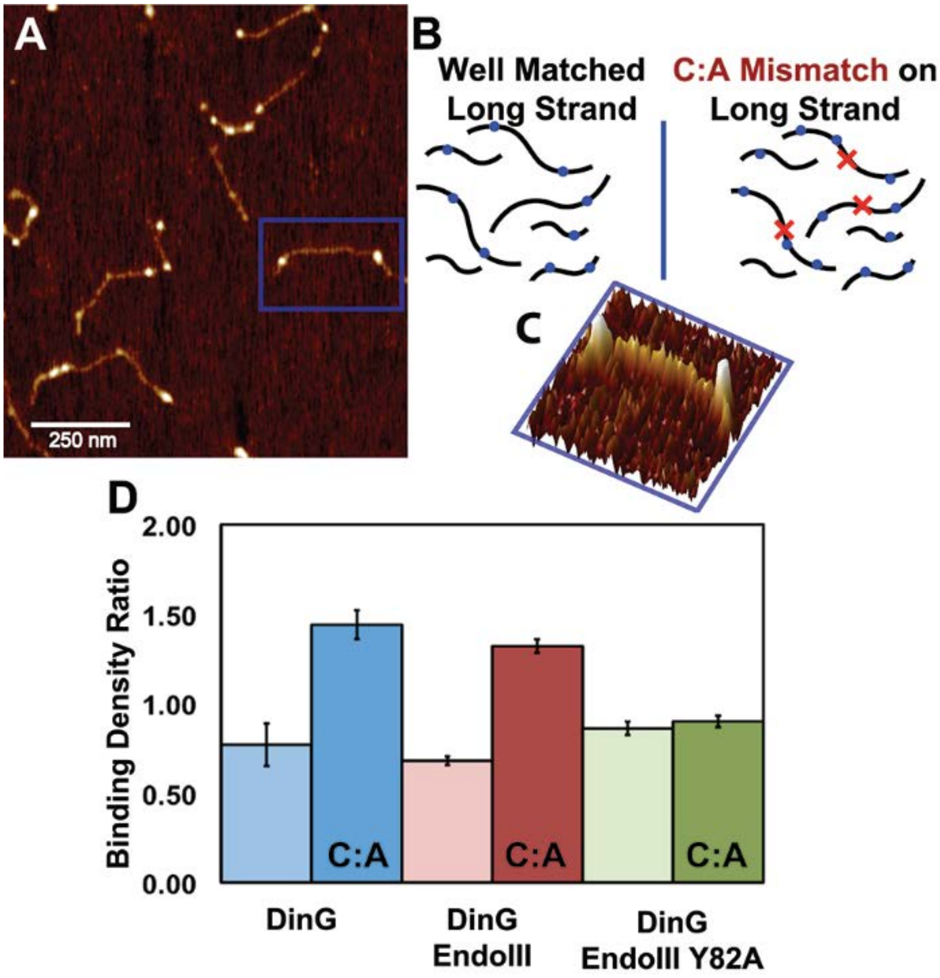

Figure 4.4 AFM redistribution assay. (A) A flattened image (Bruker nanoscope analysis software) for tapping-mode AFM topography of DinG-bound DNA adsorbed on mica. (B) Schematic representation of the redistribution assay. At equilibrium, repair proteins (blue) are preferentially localized on strands of DNA (black) with a C:A mismatch (red X). (C) 3-dimensional rendering of the blue-bordered region of the AFM image in A that shows a strand of DNA bound by two DinG proteins. (D) Measured binding density ratios, the density of proteins on long strands divided by the density of proteins on short strands, for proteins bound to mixtures of long and short strands of DNA with and without a mismatch (C:A) in the middle of the long strand. Three separate mixtures of protein and DNA were deposited onto individual surfaces and at least fifty images were analyzed for each DinG (blue), a mixture of DinG and EndoIII (red), and a mixture of DinG and a CT-deficient mutant, Y82A EndoIII (green). ± SEM using a single image as a data point.

In 1:1 mixtures of DinG and EndoIII Y82A, a mutant protein that is defective in DNA-mediated CT (22, 35), a binding density ratio of 0.90 ± 0.03 is found (Figure 4.4); there is no preference for the mismatched strand, note that EndoIII does not bind preferentially to a mismatch (22).This binding density ratio is comparable to what is observed for DinG alone when both strands are fully matched (Figure 4.4); when the proteins cannot carry out DNA CT, they cannot redistribute onto the strand containing the lesion. Since DinG can redistribute in the absence of EndoIII, and DinG and EndoIII can redistribute when mixed only if EndoIII is effective in signaling by DNA CT, these observations support the need for effective signaling between EndoIII and DinG in finding the damaged strand. We have seen comparable results earlier in mixtures of SaXPD and EndoIII (35).

An alternative way to calculate the binding density ratio is to treat each individual image as a sample, to plot them as a histogram (Figure 4.2) and to find the mean of the normal distribution. Using this methodology, instead of treating each surface as an individual experiment, a binding density ratio of 1.61 ± 0.08 is found for DinG with mismatched DNA. A binding density ratio of 1.40 ± 0.05 is found for DinG mixed with EndoIII and mismatched DNA. Finally a binding density ratio of 0.91 ± 0.04 is found for DinG mixed with EndoIII Y82A.

Because the AFM images are snapshots of the system near equilibrium, the number of bound proteins on strands reflects the apparent non-specific binding affinity of the proteins for DNA. As such, another way to analyze the data would be to analyze the apparent binding affinity of each protein in the different experiments by visualizing the occupancy of the DNA, i.e., the percent of DNA with a minimum of 1, 2, 3, or 4 proteins on a strand of DNA. Since DNA-binding proteins with 4Fe-4S clusters have a lower

DNA binding affinity when the cluster in the reduced vs. oxidized (19), in a collection of proteins, some reduced and some oxidized, CT between proteins should affect the overall effective binding affinity for DNA. Conversely, if only one protein is bound to DNA, its affinity would not be affected by DNA CT. This was observed for mixtures of DNA and DinG (Figure 4.5), which also indicates that DinG does not preferentially bind a mismatch. The same was observed for mixtures of DinG with WT EndoIII, or with EndoIII Y82A; the percent of long, well-matched strands with one protein bound is the same for DinG/EndoIII and DinG/Y82A mixtures (Figure 4.6). If more than one protein is bound to a given strand, however, each subsequent protein that binds has a probability to transport charge through the DNA and promote another protein's dissociation, in a way that parallels anti-cooperative binding. If a mismatch is present, which attenuates CT, however, this anti-cooperative effect would be lessened as it would if EndoIII Y82A is substituted for EndoIII, decreasing the concentration of signaling partners.

This is precisely what is observed (Figures 4.5 and 4.6). The percentage of long strands with a minimum of 2, 3, or 4 bound DinG proteins is lower for DinG when there is no mismatch, then when there is a mismatch. When DinG is mixed with EndoIII compared to EndoIII Y82A, an anti-cooperative effect is once again observed. There is a decreased percentage of long strands of DNA bound with a minimum of 2, 3, or 4 proteins for DinG and EndoIII compared to DinG and EndoIII Y82A. This observation, especially when considered in conjunction with their similar population of single-bound-protein-DNA complexes, further supports the ability of DinG and EndoIII to cooperate using DNA-mediated CT.

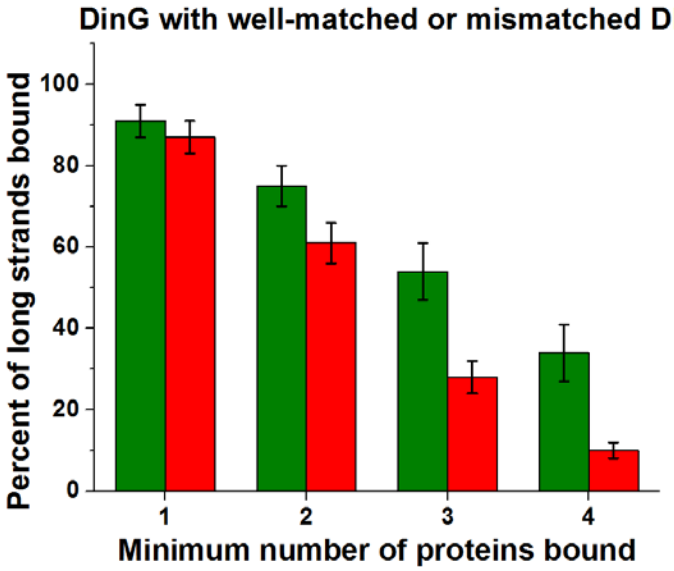

Figure 4.5 Occupancy of DinG on long strands of DNA. The percent of long strands of either well-matched (red) or mismatched (green) DNA is plotted against the minimum number of proteins bound to a strand.

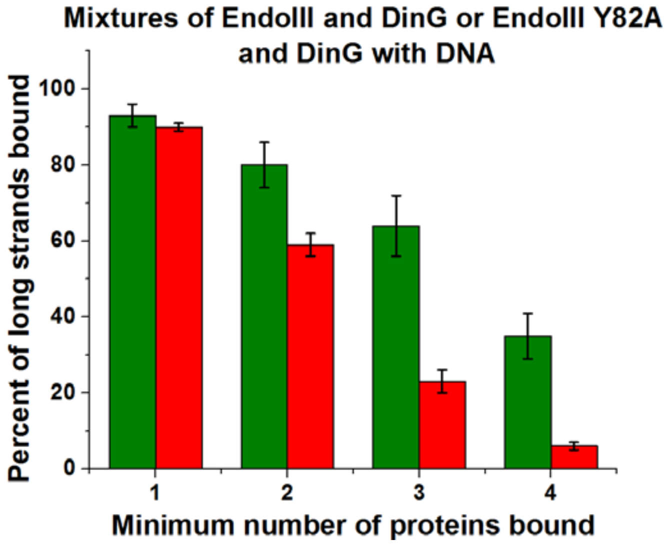

Figure 4.6 Occupancy of either EndoIII and DinG or EndoIII Y82A and DinG on long strands of well-matched DNA. The percent of well-matched long strands of either EndoIII and DinG (green) or EndoIII Y82A (red) DNA is plotted against the minimum number of proteins bound to a strand.

It should be noted that protein loadings on the 3.8 kb strands are on the order of two proteins per strand under these experimental conditions. Therefore assuming that DinG and EndoIII are signaling one another, for approximately half of the strands, signaling must occur between DinG and EndoIII rather than just between DinG partners or between EndoIII partners. Moreover, given a loading of about two proteins per strand, these results are consistent with DNA CT occurring over kilobase distances. The AFM experiments described here could not distinguish the proteins from one another, due to the compressibility of the proteins making their heights indistinguishable. It is also important to note that these proteins show no evidence of co-localizing at DNA sites by AFM. Overall, these data demonstrate that DinG and EndoIII can use DNA-mediated CT at long range to cooperate with one another to localize to regions of damage.

Modeling the influence of DNA CT on protein affinity to DNA

An equilibrium model was made to better understand the data collected by atomic force microscopy. As shown in figure 4.7, there are few observable macrostates for proteins bound to DNA. It is possible to count the number of proteins that are bound to each duplex, and assume that each protein-bound state has its own equilibrium. These equilibria will be influenced by factors that change the protein's effective affinity to DNA such as the redox identity of the [4Fe4S] cluster and the likelihood that the protein will dissociate from DNA via DNA-mediated CT. These factors are not inherently observable and thus may be described as microstates, with all of the possible variations in these characteristics having their own predicted affinity (Figure 4.8). Combining all of the microstate affinities with the probability of those microstate being observed gives the effective affinity of the macrostate.

For a single protein, the equation describing the combination of microstates, shown below, is fairly simple:

$$K_1 = \frac{k_1}{k_{-1}} = N_1(\kappa_1^R + \kappa_1^O) \tag{1}$$

Here K_1 is the effective affinity describing a single protein bound to a DNA duplex. This protein can be either in the reduced (R) or oxidized (O) state, each of which has its own affinity for the DNA duplex. The likelihood of a state being in the reduced or oxidized form must also be considered. Combining these give the terms k_1^R (and k_1^O) which are the percent reduced (and oxidized) protein multiplied by the single base pair affinity of a protein in that oxidation state. The term N_1 is a proportionality term that divides the sum of each microstate by the total number of microstates to get an average affinity for all microstates together. For a single protein there is no possibility for DNA-mediated CT so it does not contribute to the affinity.

Incorporating a second protein becomes significantly more complicated, because now there are combinations of proteins that may have different affinities depending on their location relative to one another as well as their redox identity (Figure 4.8).

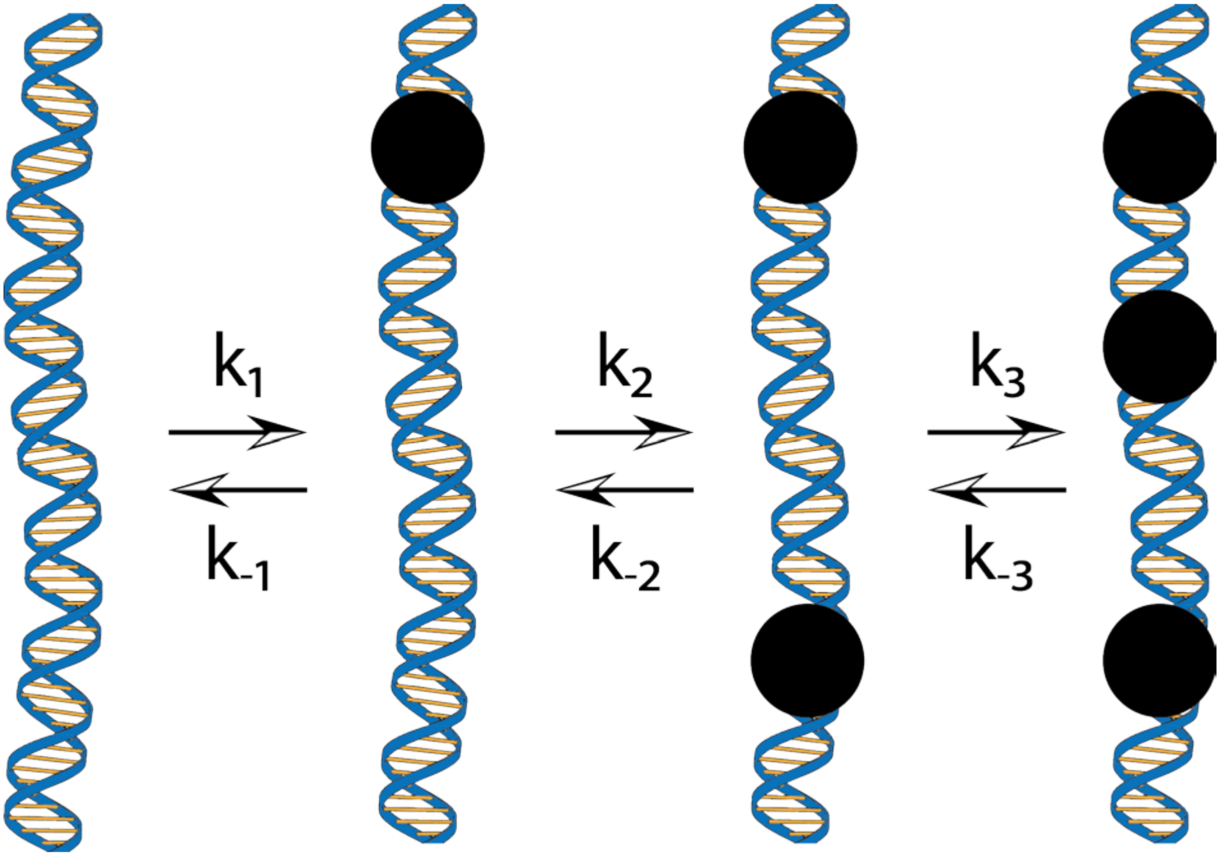

Figure 4.7 Representation of the different macrostates that are observable by atomic force microscopy. These can be described as DNA with no proteins bound, with a single protein bound, with two proteins bound, and with three proteins bound.

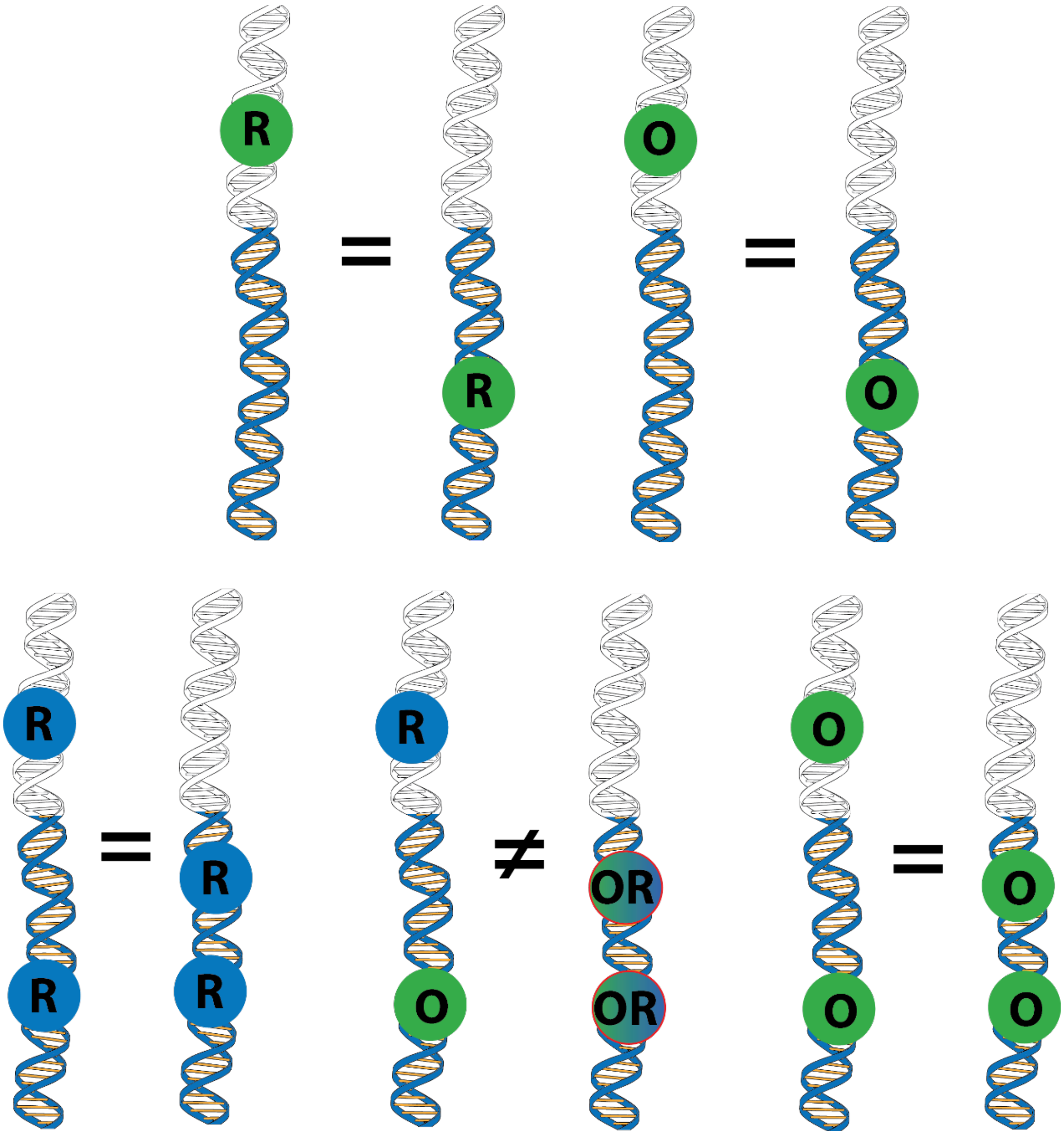

Figure 4.8 Representation of different microstates, in which proteins with reduced (R) or oxidized (O) [4Fe4S] clusters are bound to a DNA duplex. In all cases where only reduced or only oxidized proteins are bound the affinity is expected to be the same regardless of where the proteins bind. However, if a reduced and oxidized protein bind to the same duplex the effective affinity will change depending on whether the two proteins are close enough to exchange an electron via DNA mediated charge transport.

In particular, if two proteins of differing redox state are within DNA-mediated CT distance they will have a decreased effective affinity for the duplex (Figure 4.9). However, the distance that DNA-mediated CT may travel between proteins is unknown. Additionally, the decrease in affinity due to DNA-mediated CT is unknown. Unlike other constants that may be experimentally tested directly, these unknowns present an interesting application of this model in that they may be determined with enough data and fitting to this model. The two protein equation is as follows:

$$K_2 = \frac{k_2}{k_{-2}} = N_{2,1}(\kappa_1^R \kappa_2^R + \kappa_1^O \kappa_2^O) + N_{2,2}(\kappa_1^R \kappa_2^O + \kappa_1^O \kappa_2^R) + N_{2,3}(\kappa_1^{R\bar{O}} \kappa_2^{R\bar{O}}) \qquad (2)$$

with all of the terms having similar definitions as in the first equation. The terms k_1^R (and k_1^O) are the percent reduced (and oxidized) protein multiplied by the single base pair affinity of a protein in that oxidation state. The terms k_2^R and k_2^O represent the affinity of the second protein that binds, though the first and second protein are indistinguishable. The terms k_1^{RO} and k_2^{RO} represent the affinity of the state in which two proteins are within CT distance, which gives them a different effective affinity compared to the case in which the two proteins are not within CT distance. In this equation the three proportionality terms $N_{2,1}$, $N_{2,2}$, and $N_{2,3}$ combine to give an average affinity for all microstates together, but the relative weight for $N_{2,2}$, and $N_{2,3}$ change depending on the length of DNA and the length that DNA CT can occur.

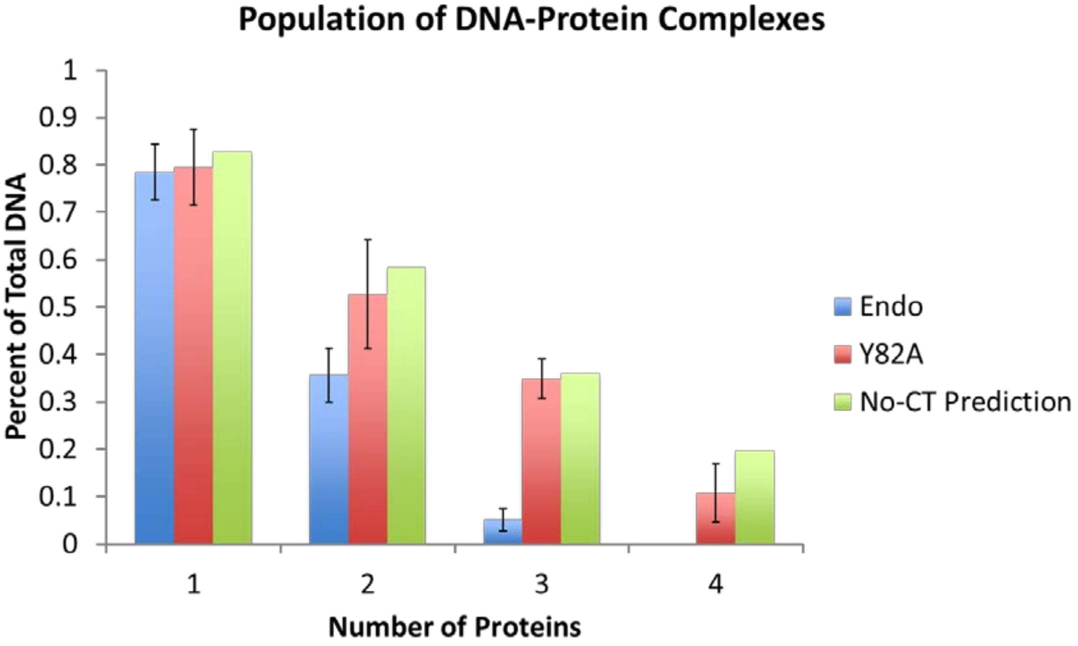

Figure 4.9. The population of 4950 bp linearized plasmid DNA with a given number of proteins for wild type EndoIII, a charge transport deficient mutant Y82A, and a prediction for the number of bound proteins if there were no influence of DNA mediated CT on the affinity. There is no difference in affinity for WT and Y82A with a single protein binding, where DNA CT cannot occur. There is a significant decrease in affinity for WT that is not present for Y82A as the number of proteins increases that correlates to an increased probability of DNA CT upon protein binding. These data strongly support a model where DNA-mediated CT is decreasing the effective affinity of EndoIII.

Finally, the three protein equation becomes significantly more complicated by the many possible identities for proteins as well as the presence of states where three proteins may be able to undergo DNA-mediated CT, or two proteins are able to and one is not. The equation can be described as follows:

$$\begin{aligned} K_3^P = \frac{k_3}{k_{-3}} = {} & N_{3,1}(\kappa_1^R \kappa_2^R \kappa_3^R + \kappa_1^O \kappa_2^O \kappa_3^O) \\ & + N_{3,2}(\kappa_1^R \kappa_2^R \kappa_3^O + \kappa_1^O \kappa_2^O \kappa_3^R + \ldots) \\ & + N_{3,3}(\kappa_1^R \kappa_2^{O\bar{}R} \kappa_3^{O\bar{}R} + \kappa_1^O \kappa_2^{O\bar{}R} \kappa_3^{O\bar{}R}) \\ & + N_{3,4}(\kappa_1^{R\bar{}O} \kappa_2^{R\bar{}O} \kappa_3^R + \kappa_1^{R\bar{}O} \kappa_2^{R\bar{}O} \kappa_3^O) \\ & + N_{3,5}(\kappa_1^{R\bar{O}O} \kappa_2^{R\bar{O}O} \kappa_3^{R\bar{O}O} + \kappa_1^{R\bar{R}O} \kappa_2^{R\bar{R}O} \kappa_3^{R\bar{R}O}) \end{aligned} \qquad (3)$$

The terms k_1^R (and k_1^O) are the percent reduced (and oxidized) protein multiplied by the single base pair affinity of a protein in that oxidation state. The terms k_2^R and k_2^O represent the affinity of the second protein that binds. The terms k_3^R and k_3^O represent the affinity of the third protein that binds, though all three proteins are indistinguishable. The terms k_1^{RO} and k_2^{RO} represent the affinity of the state in which two proteins are within CT distance, which gives them a different effective affinity compared to the case in which the two proteins are not within CT distance. Similarly, the terms k_n^{ROO} and k_n^{RRO} represent the affinity of the state in which three proteins are simultaneously within CT distance. In this equation the proportionality term $N_{3,1}$ is independent of DNA CT length. The terms $N_{3,2}$, $N_{3,3}$, $N_{3,4}$, and $N_{3,5}$ will vary significantly with the length of DNA and the length that DNA CT occurs over.

The proportionality constants were determined either using calculus for the one and two protein cases or with the aid of simulations conducted by Zachery Nicolaou (Caltech graduate student in physics) for the three protein case with the assumption that the length of DNA is greater than the length of CT. The simulations involved the generation of solutions which were then fit in Mathematica to give an approximate solution for $N_{3,1\text{-}5}$. These methods give the values as follows:

$N_1 = n$
$N_{2,1} = \frac{1}{2}(n-1)*n$
$N_{2,2} = \frac{1}{2}(n-c-1)*(n-c)$
$N_{2,3} = -\frac{1}{2}c*(1+c)+c*n$
$N_{3,1} = (1/6)*(n-2)*(n-1)*n$
$N_{3,2} = (1/6)*(n-2-2c)*(n-1-2c)*(n-2c)$
$N_{3,3} = (1/3)*c*(2+7c^2-9c*(n-1)+(3n-6)*n)$
$N_{3,4} = (1/3)*(c-1)*c*(1+c)+(c/2)*(1+c)*(n-2c)$
$N_{3,5} = (1/6)*(c-1)*c*(-2c-2+3n)$

In these equations n represents the total number of base pairs in the length of the duplex and c represents the maximum charge transport distance in base pairs.

These equations do not accurately describe the proportionality constants in all conditions. As the length of DNA CT approaches zero, $N_{2,2}$ approaches its maximum value and $N_{2,3}$ approaches zero. As the length of DNA CT approaches the length of the DNA duplex, $N_{2,2}$ approaches zero and $N_{2,3}$ approaches its maximum value. For all cases where the length of DNA CT is greater than the length of the DNA duplex $N_{2,2}$ is zero. In all cases $N_{2,1}$ is insensitive to the length of DNA CT. Similar claims can be made about the N_3 proportionality terms, but for the sake of simplicity the N_2 terms will be described.

Experimental evidence (Figure 4.9) shows that DNA CT decreases the effective affinity of proteins for DNA, which means that when the length of CT is equal to or greater than the length of the DNA duplex the macrostate affinity value K_2 is its weakest. The effective macrostate affinity will increase as the length of DNA increases beyond the length that DNA CT can traverse. The maximum affinity will occur when the length of DNA CT is so much smaller than the length of DNA that it is effectively zero.

Therefore, for two or more proteins that undergo DNA-mediated CT, a plot of macrostate affinity versus the length of DNA is described by piecewise functions. The affinity calculated by the subfunction on either side of the limit where DNA length equals the length of DNA CT will vary differently with the length of DNA. The macrostate affinity per base pair will remain constant with increasing DNA length when the length of DNA is shorter than the effective length of DNA CT. The macrostate affinity per base pair will increase when the length of DNA is extended longer than the effective length of DNA CT. These interesting characteristics can be used to determine the effective length of DNA CT and its influence on affinity, if data are collected using enough varied lengths of DNA that the data set includes lengths longer and shorter than the effective DNA CT length.

To emphasize the capability of these data to determine the effective DNA CT length, the calculated affinity of the two protein bound DNA state was plotted against DNA length for arbitrary values (Figure 4.10). The affinity for every DNA length 1 to 1000 base pairs long was calculated using arbitrary values for the length of DNA CT, the affinity of a reduced protein, the affinity of an oxidized protein, the affinity change caused by DNA CT, and the proportion of reduced and oxidized protein entered into the equations above in an excel spreadsheet. Due to the lack of direct evidence showing the exact affinity of [4Fe4S] cluster containing proteins in their reduced or oxidized states the oxidized protein was assumed to have an affinity value of 1 and the reduced protein has an affinity 1000 times weaker, because there is electrochemical evidence of a difference in affinity of approximately three orders of magnitude (19). The effective DNA CT length was set to either 200 base pairs or 400 base pairs. The amount of oxidized protein in the sample was assumed to be 0.1% and reduced protein was assumed to be 99.9%. DNA CT was assumed to either reduce the affinity to 1/10 or 1/100 the value that would be observed without CT.

Additional simulated values were plotted in Figure 4.11 to determine how this plot changed with different amounts of oxidized protein. Having no oxidized or reduced protein prevents CT and keeps the affinity per base pair constant for different DNA lengths. Having a small amount of oxidation results in the largest difference between the minimum affinity where DNA CT < DNA length and the maximum affinity where DNA length >> DNA CT length. Increasing the amount of oxidation decreases this difference until it is barely noticeable at extremely large amounts of oxidation.

These simulated plots suggest that the DNA CT length can be determined by measuring the effective affinity of [4Fe4S] containing proteins with different DNA lengths. If enough data were collected for DNA lengths below and above the length of DNA CT a plot should show a length of DNA that corresponds to a sudden increase in the effective affinity of the protein for the duplex. This length of DNA will correspond to the effective DNA CT distance between proteins.

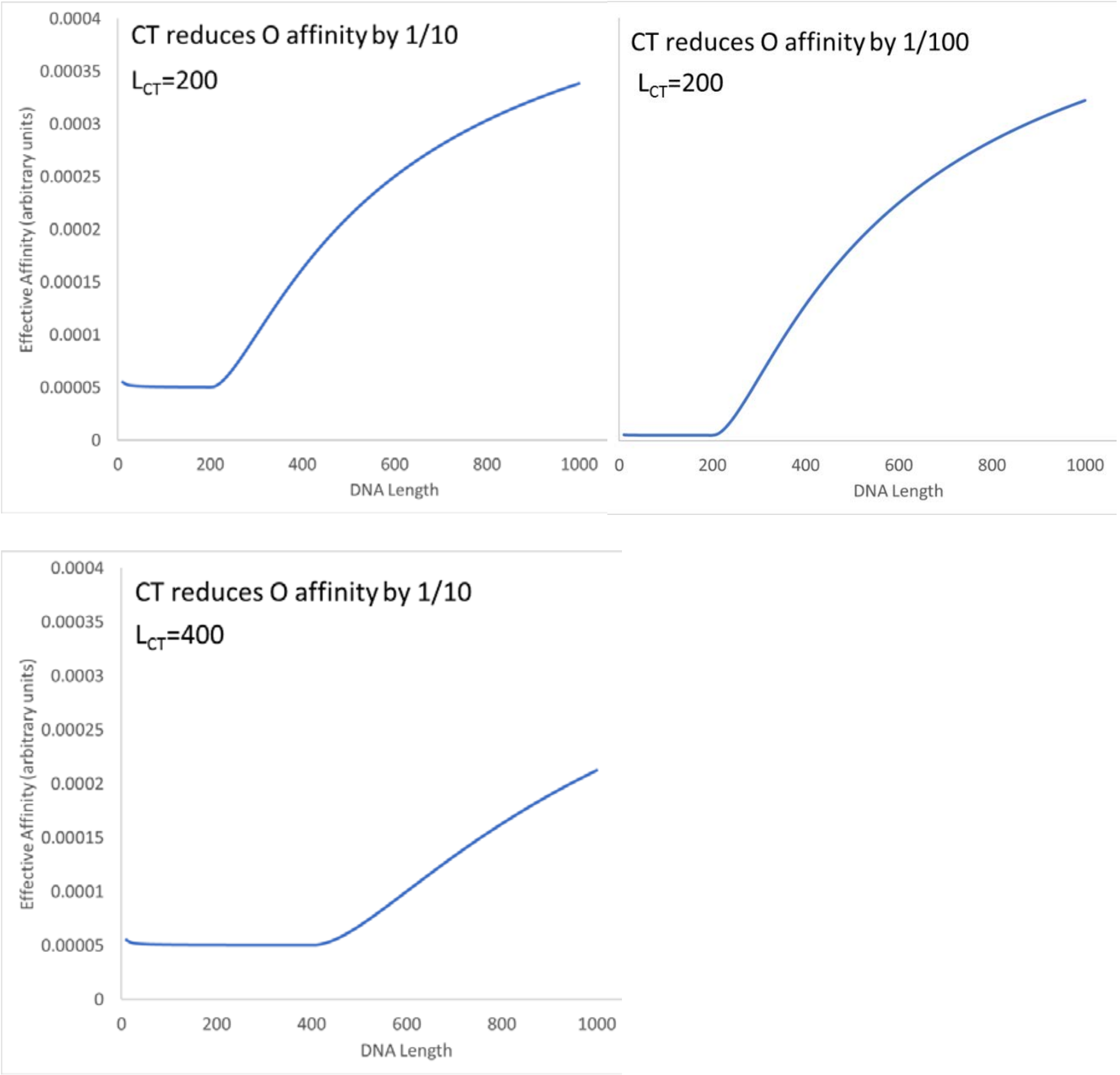

Figure 4.10 Plots of the effective affinity for two proteins bound to DNA under simulated conditions. In each case it was assumed that the reduced protein has 1000x weaker affinity for DNA when compared to the oxidized protein. The degree to which DNA CT decreases affinity manifests as a significant change for lengths near and below that distance, but becomes less noticeable at lengths significantly larger. A significant change in slope for a plot of the effective affinity vs DNA length should be observable when comparing lengths shorter than and longer than the DNA CT distance.

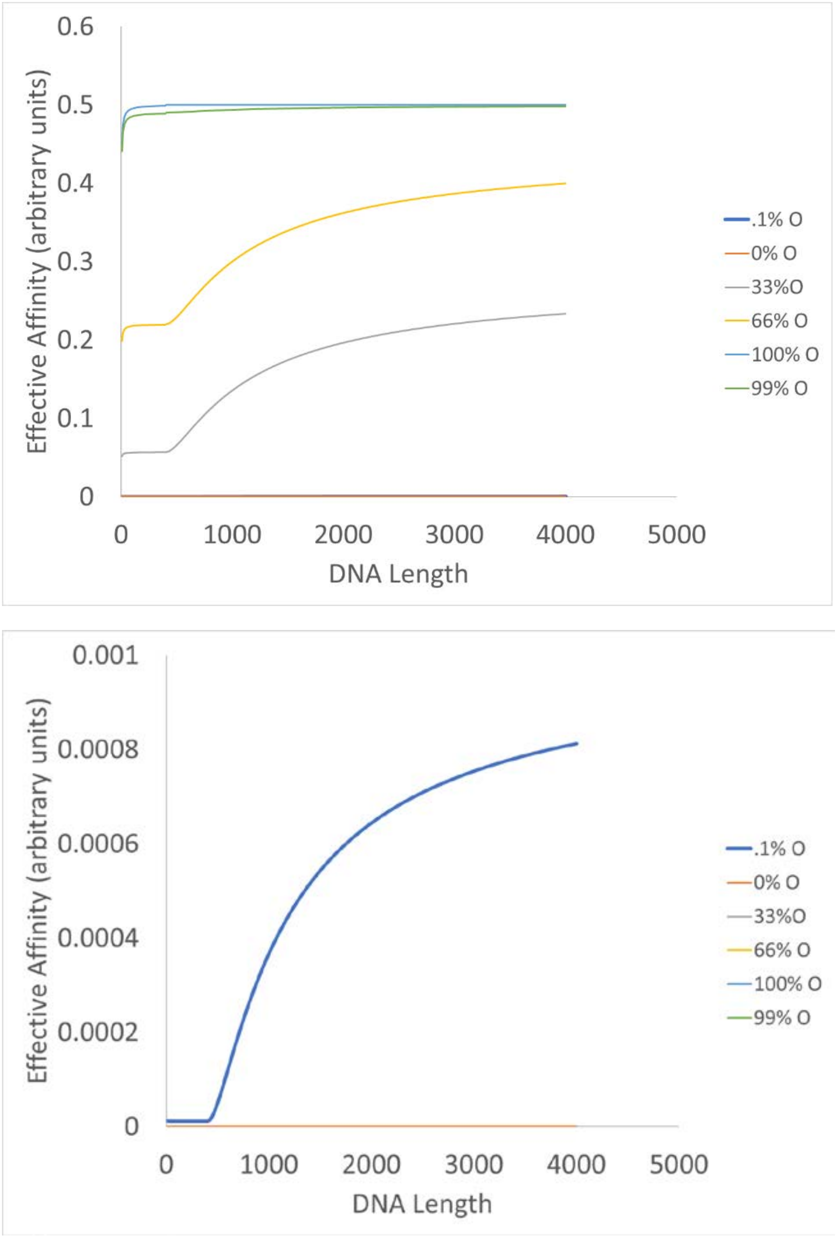

Figure 4.11 Plots of the effective affinity for two proteins bound to DNA under simulated conditions with varying proportion of oxidized protein. In each case it was assumed that the reduced protein has 1000x weaker affinity for DNA when compared to the oxidized protein. The length of DNA CT was assumed to be 400 bp. DNA CT was assumed to decrease the affinity of the two protein case to 1/100 its value without DNA CT.

Determining the effective DNA CT length will also allow for precise determination of the proportion of microstates where proteins can or cannot undergo DNA CT. Knowing the macrostate affinity, the proportion of microstates that can or cannot undergo DNA CT, the length of DNA used, and the DNA CT length, will allow for rough determination of the affinity change caused by DNA CT. Additional experiments could be performed to determine the proportion of reduced and oxidized proteins as well as their affinities, which will allow for more exact determination of the affinity change caused by DNA CT. Simply testing a single DNA length will not be able to determine these constants unless it is understood what side of the piecewise function the data lie on and they are modified accordingly.

DISCUSSION

Our model for how DNA repair proteins with 4Fe-4S clusters use DNA-mediated CT as a first step in locating lesions to repair is depicted in Figure 4.12. Critical to the model is the fact that the DNA binding affinity of a protein that has a 4Fe-4S cluster is dependent on the oxidation state of the cluster. For these proteins, the shift in reduction potential upon DNA binding necessitates a lower DNA binding affinity of two-to-three orders of magnitude for a 200 mV shift when in the reduced form (2+) compared to the oxidized form (3+) (19). Figure 1 shows that the DNA-bound potential is significantly shifted from that reported in the absence of DNA (30). Therefore, as illustrated in Figure 4.12, 4Fe-4S clusters in these proteins when they are freely diffusing are expected to be in the 2+ state. Upon binding to DNA, however, the proteins are activated towards oxidation.

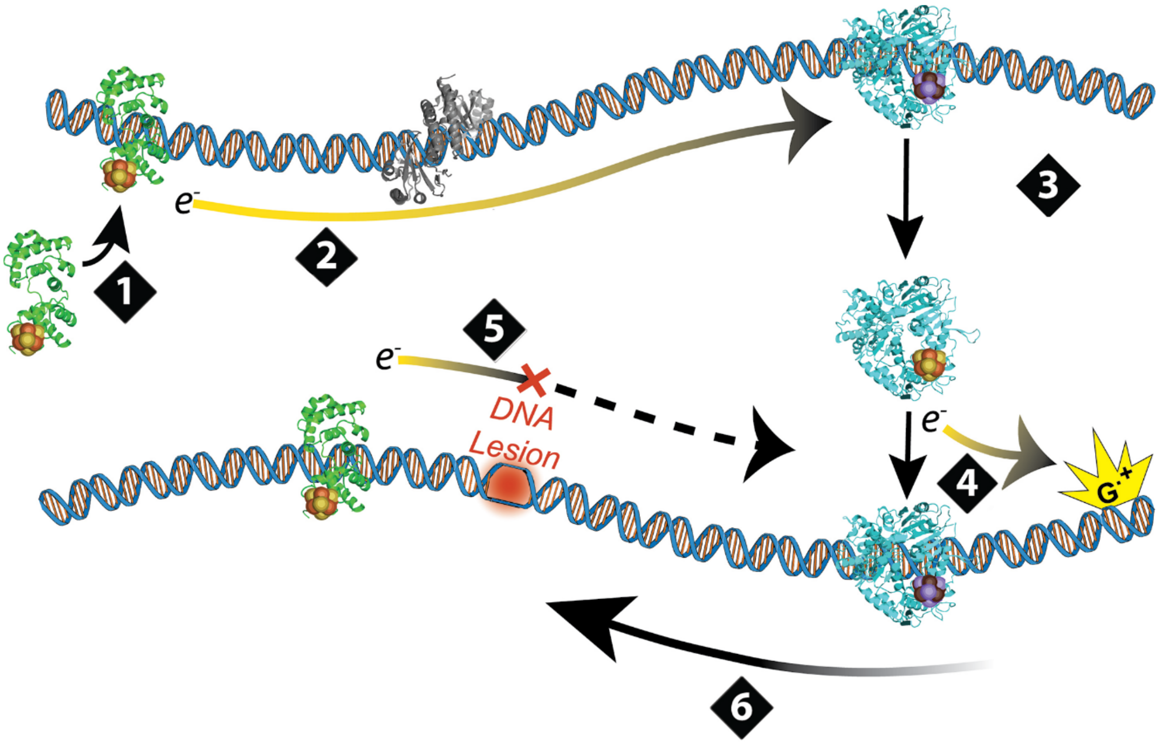

Figure 4.12 Scheme depicting how repair proteins may use DNA-mediated signaling to search for damage. The model describes how DNA CT can drive the redistribution of the repair proteins into the vicinity of damage. [1] A protein with a reduced (orange-yellow) iron-sulfur cluster binds to DNA. [2] This protein's iron-sulfur cluster is oxidized (purple-brown) by another DNA-bound redox-active protein. This oxidation can occur over long distances and through other DNA-bound proteins (grey) so long as the π-orbital stacking of bases between the reductant and oxidant is unperturbed. [3] Reduction promotes the repair protein's dissociation from DNA. [4] The repair protein binds to an alternate DNA site where it is oxidized either by a guanine radical or another protein. [5] DNA lesions between proteins inhibit electron transport, so protein dissociation is not promoted. [6] Proteins that are now in close proximity to the lesion are able to move processively towards the damage for repair.

A given protein already bound to DNA in the oxidized form, perhaps oxidized from a distance by a guanine radical generated under oxidative stress (44), could thus be reduced in a DNA-mediated fashion by another distinct redox-active protein that binds within CT distance of the first protein. Reducing this second protein would promote its dissociation from DNA. This inter-protein signaling requires an undamaged path between the two proteins; intervening DNA damage prevents the protein from receiving reducing equivalents so that its dissociation is not promoted. Effectively, this electron transfer event signals the repair protein to dissociate from undamaged regions and search for damage elsewhere in the genome. If there is an intervening damage product that blocks CT, however, then the repair protein stays bound in the vicinity of damage, and the protein can move on a slower timescale to the local site in need of repair. This process would lead to the redistribution of repair proteins in the vicinity of damage through an efficient scanning of the genome by proteins of similar redox potential.

In essence, these proteins inform one another about the integrity of DNA by using DNA as a medium through which they transmit electronically encoded information. Because this signaling occurs over long distances, this mechanism would significantly reduce the time required to scan the genome, allowing for enzymes to repair the genome on biological timescales. Indeed, even when CT distances of only 100 bases, that which we have documented, are permitted in our model, a significant reduction in search time to scan the *E. coli* genome can be predicted (22). Importantly, other models have been investigated for how BER enzymes similar to EndoIII can scan the genome and locate their substrates. For example, it has been shown that one-dimensional sliding along DNA can be fast enough for glycosylases to come into contact with bases in the genome on the order of seconds (45-47). Models for one-dimensional sliding do not, however, take into account protein traffic along the genome. It is important to note that DNA-mediated CT is not interrupted by intervening bound proteins as long as the proteins do not perturb the base pair stack. Thus sliding, hopping, and DNA CT models taken together offer an appealing means to explain how the search process may be optimized under the realistic conditions of the cell.

Data from DNA-modified electrochemistry experiments show that the DNA-bound reduction potential of DinG is remarkably similar to that for EndoIII, MutY, and SaXPD (19-21). As such, DinG is competent to shuttle electrons through DNA to or from EndoIII or MutY via its 4Fe-4S cluster, as would be required by the model proposed for the redistribution of these proteins to sites of damage. As with EndoIII and MutY, we consider the redox potential of DinG to correspond to the $[4Fe\text{-}4S]^{3+/2+}$ couple that is now accessible due to the negative potential shift associated with binding to the DNA polyanion (19). The ATP-dependent increase in current intensity observed for DinG on electrodes is consistent with previous results for SaXPD, except that the signal increase is nearly an order of magnitude higher than that observed for the thermophilic SaXPD (21). This substantial difference in signal increase is understandable based upon the significantly lower rate of ATP hydrolysis of SaXPD versus DinG at ambient temperature. It is interesting to consider that the increase in signal intensity could be a general characteristic of these DNA enzymes that contain redox-active clusters, where they signal not only their presence, but also their activity. For DinG, there could be signaling to upstream proteins that DinG is in the process of unwinding its substrate.

The atomic force microscopy experiments, moreover, support signaling between EndoIII and DinG *in vitro*. Based on the model, we expect the redistribution of proteins that use DNA-mediated CT signaling onto strands containing a single base mismatch and away from fully matched duplex DNA, which is the observed result. Proteins that are defective in DNA CT, furthermore, do not relocate to the mismatched strand, as predicted by our model.

These data are not able to determine the effective DNA CT length nor a quantitative measurement of how much DNA CT reduces the effective affinity of proteins for DNA. The most adequate way to determine the effective DNA CT length may be to collect AFM data for proteins bound to DNA with different lengths. Plotting the effective affinities for different lengths of DNA under identical conditions and determine the effective CT distance by looking for the length at which the piecewise function changes. These data could accurately determine CT distance and the effective change in affinity caused by DNA-mediated CT.

Overall these results provide substantial evidence that *E. coli* enzymes from distinct repair pathways signal one another from a distance through DNA as long as the proteins remain competent to carry out DNA-mediated CT, as measured electrochemically. The AFM experiments show that a single base mismatch in a 3.8 kb duplex is sufficient to promote the redistribution of the 4Fe-4S proteins to damaged DNA, driven by long range signaling. Signaling through DNA CT is fast (ps) (48), can occur over long molecular distances, and allows for the binding of many intervening proteins, as long as their distortion of the DNA duplex is minimal. As such, DNA CT provides a mechanism for efficient signal transduction on biological timescales, as the cell requires. Our proposed redistribution model is one way in which proteins may use DNA CT to efficiently scan the genome as a first step in finding lesions to repair and to prepare the genome for replication. The utilization of DNA CT by enzymes to maintain cellular viability and genomic integrity represents a novel role for 4Fe-4S clusters in DNA-processing enzymes. A growing body of evidence is emerging that highlights the importance of iron-sulfur clusters in enzymes that are involved in nearly every aspect of DNA metabolism. The results here provide a basis for understanding the ubiquity of 4Fe-4S clusters in proteins that maintain the integrity of the genome throughout the phylogeny.

REFERENCES

1. Genereux, J. C.; Boal, A. K.; Barton, J. K. *J. Am. Chem. Soc.* **2010**, *132*, 891.
2. Wu, Y.; Brosh, R. M., Jr. *Nucleic Acids Res.* **2012**, *40*, 4247.
3. White, M. F.; Dillingham, M. S. *Curr. Opin. Struct. Biol.* **2012**, *22*, 94.
4. Cunningham, R. P.; Asahara, H.; Bank, J. F.; Scholes, C. P.; Salerno, J. C.; Surerus, K.; Munck, E.; McCracken, J.; Peisach, J.; Emptage, M. H. (1989) *Biochemistry* **1989**, *28*, 4450.
5. Wu, Y.; Suhasini, A. N.; Brosh, R. M., Jr. *Cell Mol. Life Sci.* **2009**, *66*, 1209.
6. Weiner, B. E.; Huang, H.; Dattilo, B. M.; Nilges, M. J.; Fanning, E.; Chazin, W. J. *J. Biol. Chem.* **2007**, *282*, 33444.
7. Netz, D. J. A.; Stith, C. M.; Stümpfig, M.; Köpf, G.; Vogel, D.; Genau, H. M.; Stodola, J. L.; Lill, R.; Burgers, P. M. J.; Pierik, A. J. *Nat. Chem. Biol.* **2011**, *8*, 125.
8. Yeeles, J. T. P.; Cammack, R.; Dillingham, M. S. *J Biol Chem.* **2009**, *284*, 7746.

9. Saikrishnan K, Yeeles, J. T.; Gilhooly, N. S.; Krajewski, W. W.; Dillingham, M. S.; Wigley, D. B. *EMBO J.* **2012**, *31*, 1568.
10. Pokharel, S.; Campbell, J. L. *Nucleic Acids Res*. **2012**, *40*, 7821.
11. Liu, H.; Rudolf, J.; Johnson, K. A.; McMahon, S. A.; Oke, M.; Carter, L.; McRobbie, A. M.; Brown, S. E.; Naismith, J. H.; White, M. F. *Cell* **2008**, *133*, 801.
12. Fan L.; Fuss, J. O.; Cheng, Q. J.; Arvai, A. S.; Hammel, M.; Roberts, V. A.; Cooper, P. K.; Tainer, J. A. *Cell* **2008**, *133*, 789.
13. Wolski, S. C.; Kuper, J.; Haenzelmann, P.; Truglio, J. J.; Croteau, D. L.; Van-Houten, B.; Kisker, C. *PLoS Biol* **2008**, *6*, 1332.
14. Porello, S. L.; Cannon, M. J.; David, S. S. *Biochemistry* **1998**, *37*, 6465.
15. Veatch, J. R.; McMurray, M. A.; Nelson, Z. W.; Gottschling, D. E. *Cell* **2009**, *137*, 1247.
16. Stehling, O.; Vashisht, A. A.; Mascarenhas, J.; Jonsson, Z. O.; Sharma, T.; Netz, D. J. A.; Pierik, A. J.; Wohlschlegel, J. A.; Lill, R. *Science* **2012**, *337*, 195.
17. Gari K.; Léon Ortiz, A. M.; Borel, V.; Flynn, H.; Skehel, J. M.; Boulton, S. J. *Science* **2012**, *337*, 243.
18. Sontz, P. A.; Muren, N. B.; Barton, J. K. *Acc. Chem. Res.* **2012**, *45*, 1792.
19. Gorodetsky, A. A.; Boal, A. K.; Barton, J. K. *J. Am. Chem. Soc.* **2006**, *128*, 12082.
20. Boal, A. K.; Yavin, E.; Lukianova, O. A.; O' Shea, V. L.; David, S. S.; Barton, J. K. *Biochemistry* **2005**, *44*, 8397.
21. Mui T. P.; Fuss, J. O.; Ishida, J. P.; Tainer, J. A.; Barton, J. K. *J. Am. Chem. Soc.* **2011**, *133*, 16378.

22. Boal, A. K.; Genereux, J. C.; Sontz, P. A.; Gralnick, J. A.; Newman, D. K.; Barton, J. K. *Proc. Natl. Acad. Sci. U.S.A.* **2009**, *106*, 15237.
23. Genereux, J. C.; Barton J. K. *Chem. Rev.* **2010**, *110*, 1642.
24. Boal, A. K.; Barton, J. K. *Bioconj. Chem.* **2005**, *16*, 312.
25. Boon, E. M.; Salas, J. E.; Barton, J. K. *Nat. Biotechnol.* **2002**, *20*, 282.
26. Kelley, S. O.; Jackson, N. M.; Hill, M. G.; Barton, J. K. *Angew. Chem. Int. Ed.* **1999**, *38*, 941.
27. Gorodetsky, A. A.; Buzzeo, M. C.; Barton, J. K. *Bioconj. Chem.* **2008**, *19*, 2285.
28. Núñez, M. E.; Hall, D. B.; Barton, J. K. *Chem. and Biol.* **1999**, *6*, 85.
29. Slinker, J. D.; Muren, N. B.; Renfrew, S. E.; Barton, J. K. *Nat. Chem.* **2011**, *3*, 228.
30. Ren, B.; Duan, X.; Ding, H. *J. Biol. Chem.* **2009**, *284*, 4829.
31. Voloshin, O. N.; Vanevski, F.; Khil, P. P.; Camerini-Otero, R. D. *J. Biol. Chem.* **2003**, *278*, 28284.
32. Voloshin O. N.; Camerini-Otero, R. D. *J. Biol. Chem.* **2007**, *282*, 18437.
33. Boubakri, H.; Langlois de Septenville, A.; Viguera, E.; Michel, B. *EMBO J.* **2010**, *29*, 145.
34. Pheeney, C. G.; Arnold, A. R.; Grodick, M. A.; Barton, J. K. *J. Am. Chem. Soc.* **2013**, *135*, 11869.
35. Sontz, P. A.; Mui, T. P.; Fuss, J. O.; Tainer, J. A.; Barton, J. K. *Proc. Natl. Acad. Sci. U.S.A.* **2012**, *109*, 1856.
36. Datsenko, K. A.; Wanner, B. L. *Proc. Natl. Acad. Sci. U.S.A.* **2000**, *97*, 6640.
37. Kovach, M. E.; Elzer, P. H.; Hill, D. S.; Robertson, G. T.; Farris, M. A.; Roop, R. M., II.; Peterson, K. M. *Gene* **1995**, *166*, 175.

38. Cupples, C. G.; Miller, J. H. *Proc. Natl. Acad. Sci. U.S.A.* **1989,** *86*, 5345.
39. Thomason, L.; Constantino, N.; Court, D. L. *Curr. Protoc. Mol. Biol.* **2007**, *79*, 10.5.1-10.5.11.
40. Miller, J. H. *A Short Course in Bacterial Genetics*; CSHL Press **1992**.
41. Tano K.; Iwamatsu, Y.; Yasuhira, S.; Utsumi, H.; Takimoto, K. *J. Radiat. Res.* **2001**, *42*, 409.
42. Thayer, M. M.; Ahern, H.; Xing, D.; Cunningham, R. P.; Tainer, J. A. *EMBO J.* **1995**, *14*, 4108.
43. Aguilera, A.; García-Muse, T. *Mol. Cell* **2012**, *46*, 115.
44. Yavin, E.; Boal, A. K.; Stemp, E. D. A.; Boon, E. M.; Livingston, A. L.; O'Shea, V. L.; David, S. S.; Barton, J. K. *Proc. Natl. Acad. Sci. U.S.A.* **2005**, *102*, 3546-3551.
45. Blainey, P. C.; van Oijen, A. M.; Banerjee, A.; Verdine, G. L.; Xie, X. S. *Proc. Natl. Acad. Sci. U.S.A.* **2006**, *103*, 5752.
46. Dunn, A. R.; Kad, N. M.; Nelson, S. R.; Warshaw, D. M.; Wallace, S. S. *Nucleic Acids Res.* **2011**, *39*, 7487.
47. Wallace, S. S. *Environmental and Molecular Mutagenesis* **2013**, *54*, 691.
48. Wan, C.; Fiebig, T.; Kelley, S. O.; Treadway, C. R.; Barton, J. K.; Zewail, A. H. *Proc. Natl. Acad. Sci. U.S.A.* **1999**, *96*, 6014.

Chapter 5

Redox-active [4Fe4S] Clusters Modulate the DNA-Binding Affinity of DNA Repair Proteins

Edmund Tse designed and conducted electrochemistry experiments, and designed the electrostatic model, and performed atomic force microscopy experiments. Theodore Zwang designed and assisted with atomic force microscopy experiments, and assisted with electrochemistry experiments.

Introduction

Exogenous and endogenous damage to deoxyribonucleic acid (DNA), originating from sources such as reactive oxygen species, UV irradiation, and environmental mutagens, causes lesions, mismatches, and base pair modifications in the genome of organisms on the order of millions per cell per day (1,2). Many repair mechanisms have evolved to uphold genome integrity by repairing DNA damage caused by oxidative stress (3,4). DNA repair systems utilize diverse teams of proteins to respond, search, and repair DNA damage in a timely fashion (5,6). An increasing number of DNA-processing enzymes, including many that are involved in the repair of DNA damage, have been found in archaea, bacteria, and eukaryotes to contain [4Fe4S] clusters (7-10). Elucidating the role of these clusters remains an active area of investigation (11-14). Initially, these clusters were proposed to serve primarily a role in maintaining protein structural integrity. However, recent experiments demonstrate that the presence of the [4Fe4S] cluster is not essential for the overall protein structure and thermal stability of a DNA repair enzyme, even though the cluster contributes significantly to DNA binding and enzymatic activity (15). Other studies detailing processes loading iron-sulfur clusters into repair proteins indicate that these multistep assembling procedures are resource-intensive and suggest that these clusters may have other roles (16-20).

Calculations have been performed to estimate the time needed for these [4Fe4S] repair proteins to search for DNA damage, and the results indicate that 3D random collisions, 2D sliding and hopping, and facilitated diffusion are not fast enough to explain the quick action of these proteins (21). Given the low copy number of unique DNA-processing [4Fe4S] enzymes, ranging from 500 to as low as 10 per cell (22,23), and the vast number of DNA lesions, we have proposed that these proteins aid one another through signaling using DNA-mediated charge transport (CT) between their [4Fe4S] clusters to search for and locate DNA damage sites more efficiently (21,24,25).

The highly ordered π-stacking structure of aromatic bases enables efficient CT through double-stranded DNA (dsDNA) (26-28). One single base pair mismatch, lesion, or abasic site that disrupts π-stacking can attenuate DNA-mediated CT significantly. (29-31) Ground state CT mediated by dsDNA has been measured over 100 base pairs of length, and, given a very shallow distance dependence, there is no clear indication for the maximum distance that charge can move through dsDNA (32).

Experiments with DNA repair proteins in the native 2+ oxidation state for the cluster show that CT-active proteins containing [4Fe4S] clusters localize in the vicinity of damage (24,25,33). The DNA-mediated redox properties of [4Fe4S] proteins have been established *in vitro* using biochemical assays and DNA-modified electrodes. These experiments show that the [4Fe4S] cluster within a protein can be reduced to the 2+ state or oxidized to the 3+ state by CT through a DNA duplex. The efficiency of this process is diminished when the DNA contains a mismatch or abasic site located between the protein and the electrode (29-31). Furthermore these experiments have found that binding to DNA shifts the $[4Fe4S]^{2+/3+}$ couple negative by about 200 mV to ca. +80 mV vs. NHE (34,35). This shift thermodynamically should increase the DNA-binding affinity of proteins with an oxidized [4Fe4S] cluster by at least two orders of magnitude when compared to the reduced protein.

In this report, we systematically vary the oxidation state of the [4Fe4S] cluster and measure how the redox state of the metallocofactor modulates DNA binding and, in turn, controls DNA damage detection activity of repair proteins. We specifically interrogate how oxidative stress influences the ability of [4Fe4S]-containing DNA repair proteins, Endonuclease III (EndoIII) and DinG, to bind preferentially to a 3 kilobase pairs (kbp) DNA duplex with a single-base mismatch *in vitro.* EndoIII is a base excision repair (BER) glycosylase that repairs oxidized pyrimidines in *Escherichia coli* (*E. coli*) (9). DinG is a DNA helicase that unwinds R-loops caused by invasion of DNA duplexes by nascent mRNA strands at transcription bubbles in *E. coli* (36). Both proteins have been identified to contain high-potential [4Fe4S] clusters (HiPIPs), which cycle between the $[4Fe4S]^{3+}$ and $[4Fe4S]^{2+}$ states at physiological potentials when bound to dsDNA. Previous reports have demonstrated that EndoIII and DinG can interact with each other in a synergistic fashion by localizing on mismatch-containing DNA strands *in vitro* and rescuing *E. coli* growth *in vivo* (33,37). Neither protein binds preferentially to a mismatch site, so the preference for binding the mismatch-containing strand is attributed instead to the ability of the mismatch to inhibit DNA CT (21,25,38). Here, we selectively oxidize and reduce the [4Fe4S] metallocofactors in EndoIII and DinG using electrochemical methods instead of adding chemical reagents, which could damage the proteins and DNA strands (39). We then utilize atomic force microscopy (AFM) to examine the DNA-protein interactions with varying amounts of [4Fe4S] cluster oxidation. We further develop an electrostatic model based upon the electrostatic interactions between DNA and [4Fe4S] cluster proteins to understand the change in protein binding with oxidation state.

Materials and methods

General Procedures. Chemicals were obtained from commercial sources (Sigma Aldrich, Fisher Scientific, VWR, and New England Biolabs) and used without further purification unless otherwise specified. Protein buffer (pH 7.5, 20 mM NaH_2PO_4, 100 mM NaCl, 5% glycerol, 1 mM EDTA) and DNA buffer (pH 7.0, 5 mM NaH_2PO_4, 50 mM NaCl) were prepared using Milli-Q water (>18 MΩ cm). Solutions were degassed and sparged with Ar overnight prior to conducting electrochemical experiments and preparing AFM samples inside an anaerobic chamber (Coy Lab Products). Experiments performed were replicated at least three times using different samples, and data presented are from representative trials.

Preparation of DNA-modified Electrodes for Electrochemical Studies. DNA sequences were prepared using phosphoramidites (Glen Research) on a DNA Synthesizer (Applied Biosystems 3400) or purchased from Integrated DNA Technologies and then purified by high performance liquid chromatorgraphy (HPLC, HP 1100, Agilent). Thiolated DNA was prepared according to established methods by modifying the 5' end using a C6 S–S phosphoramidite (32). Deprotection, purification, quantification, matrix-assisted laser desorption ionization (MALDI) characterization using a Autoflex MALDI TOF/TOF (Bruker), annealing of DNA, fabrication of Au electrodes, and preparation of the DNA-modified Au electrodes were performed as described previously (32,40,41). The Au electrodes were assembled and then incubated in a solution (200 µL) of thiol-modified dsDNA (50 µM) in DNA buffer for 24 h at room temperature in the dark. The electrode modified with a monolayer of thiolated-DNA was then backfilled with mercaptohexanol (1 mM, 200 µL) for 45 min, washed three times with DNA buffer or protein buffer prior to adding protein samples to the DNA-modified Au surfaces.

DNA sequences used for EndoIII electrochemistry:

HS-C6-5'-GT GAG CTA ACG TGT CAG TAC-3'

3'-CA CTC GAT TGC ACA GTC ATG-5'

DNA sequences used for DinG electrochemistry:

HS-C6-5'-GT GCT GCA ACG TGT CTG CGC-3'

3'-CA CGA CGT TGC ACA GAC GCG AGA GCA

GAC GTC AGA-5'

(HS-C6 = hexanethiol linker)

Protein Preparation and Characterization. Wild-type proteins (EndoIII and DinG) were prepared as described previously (33). Crude proteins were harvested from cells and purified using fast protein liquid chromatography (FPLC, Bio-Rad) at 4 °C. Protein concentration was quantified based on the [4Fe4S] cluster absorbance (ε_{410} = 17000 M^{-1} cm^{-1}) using a 100 Bio UV-visible spectrophotometer (Cary, Agilent) (42). Cluster loading was over 70%. Protein samples (5 μM) were sealed in Teflon-capped cuvettes under anaerobic condition and characterized at room temperature on a Model 430 circular dichroism spectrometer (Aviv). Continuous-wave electron paramagnetic resonance (EPR) and pulse electron spin echo envelope modulation (ESEEM) experiments were conducted on an EMX X-band CW-EPR Spectrometer (Bruker) and an ELEXSYS-E580 X,Q-band Pulse EPR Spectrometer (Bruker) at 10 K with samples sealed in EPR tubes in the glove bag.

Electrochemistry. Electrochemical studies were performed as described previously (34,41,42). Electrochemical experiments were carried out in a three-electrode set-up under an anaerobic atmosphere. The working electrode was a DNA-modified Au electrode, the counter electrode was a piece of freshly-polished Pt wire separated from the solution by an agarose gel tip filled with NaCl (3 M), and the reference electrode was a Ag/AgCl electrode stored in saturated NaCl solution modified with an agarose gel tip filled with NaCl (3 M). All redox potentials were converted to and reported versus the NHE scale.

Cyclic voltammetry, square wave voltammetry, and chronoamperometry were carried out using a 760 D Electrochemical Workstation (CH Instruments) at room temperature inside an anaerobic chamber. The atmosphere of the anaerobic chamber (< 1 ppm O_2, ca. 3.4% H_2) was monitored using a CAM-12 O_2 and H_2 sensor (Coy Lab Products). The chamber was maintained O_2-free by using two ventilated Pd catalyst packs (Coy Lab Products). Protein sample was placed on an electrode surface and successive potential cycling treatments between +0.4 V and –0.2 V vs. NHE at a scan rate of 100 mV/s using cyclic voltammetry were taken until the signal stabilizes. Bulk electrolytic oxidation and reduction of proteins were conducted by holding the electrode potential at +250 mV and –50 mV respectively vs. NHE for 25 min which is when the current stabilizes at a value similar to the background current obtained in a trial without protein in solution. The amount of charge passed during bulk electrolysis was calculated by integrating the area under the background-subtracted curve in the current vs. time chronoamperometric plot. The integrated charge was then divided by the Faraday's constant (96485 C/mol) to convert to the total number of moles of electrons passed (43).

Since a [4Fe4S] cluster undergoes a 1-electron redox process, the number of moles of electrons passed equals to the number of proteins oxidized or reduced (44). The number of moles of proteins present in the solution prior to bulk electrolysis was calculated from the molarity and volume of the protein solution used. The bulk electrolysis yield was then computed as the percentage of [4Fe4S] cluster protein oxidized or reduced in the whole protein sample.

Synthesis of DNA Strands for AFM Experiments. Short well-matched DNA duplex, long well-matched DNA duplex, and long DNA duplex with a C:A mismatch engineered in the middle were prepared using published protocols. (21,25,33) Briefly, four primers were synthesized, phosphorylated, and purified using phenol–chloroform extraction followed by ethanol precipitation. After drying under vacuum overnight, primers were used in PCR reactions using pUC19 as a template to generate two DNA duplexes containing 14-nucleotide single-strand overhang. Short and long duplexes were annealed and ligated together. Incomplete reaction resulted in a mixture of ligated (3767 bp, ca. 1.2 μm in length) and unligated (1610 bp and 2157 bp, ca. 0.5 μm and 0.7 μm in length) dsDNA samples that were identical with the exception of the presence of the mismatch site engineered at the overhang region. The single-strand overhang of unligated dsDNA was conjugated to complementary DNA strands prior to AFM experiments.

AFM Experiments. AFM was conducted following protocol reported previously (21,25,33). Briefly, mica surfaces were freshly cleaved with tape. Protein stock solution containing either 5 μM EndoIII or 2 μM DinG was collected after bulk electrolysis. Stock DNA solution (6 ng/μL) contained the mixture of ligated duplexes and the two unligated duplexes in Tris elution buffer (EB, Qiagen). A solution with a final protein concentration

(12 nM) and a final DNA concentration (1 ng/µL) was prepared and incubated at room temperature for 1 h to allow for the loading of protein onto DNA to reach equilibrium under an anaerobic atmosphere and minimize cluster degradation. $MgCl_2$ (200 mM, 1.5 µL per 25 µL total volume) was added to promote DNA adsorption on mica for AFM experiments. After pipetting 10 µL of DNA/protein/$MgCl_2$ solution onto a mica surface and incubating for 2 min, a continuous stream of deoxygenated Milli-Q water (2 mL) was slowly poured over the top portion of the modified mica surface while holding the piece of mica in a vertical position to linearize the DNA. A piece of kimwipe was used to dab dry the bottom edge of the mica surface. The surface was dried using a stream of N_2 flowing in the same direction as the water rinse for 2 min. pUC19 (2,686 bp, ca. 0.9 µm) linearized by HindIII (New England Biolabs) was used instead of the ligated and unligated DNA to quantify how the DNA-binding activity of EndoIII changes as a function of the ratio of oxidized $[4Fe4S]^{3+}$ cluster in the protein sample.

AFM Instrumentation. FESPA-V2 AFM tapping mode probes (Bruker Nano, Inc.) with a mean force constant of 2.8 N/m and mean resonance frequency of 75 kHz were used in a MFP-3D AFM (Asylum Research). Images were captured in air with scan areas of 3×3 μm^2 in tapping mode at a scan rate of 1 Hz in order to obtain images of quality high enough for AFM redistribution assay analysis (512 pixels/line, 512 lines/image). The images were collected and analyzed blind.

Differential Binding Density Ratio Calculations. WSxM software (Igor Pro) was used to measure DNA contour lengths and height profiles of the proteins as described previously (21,25,33). DNA and proteins were identified using the relative differential height profiles between protein and DNA. For each data set, images from at least three independent samples were analyzed, compared, and pooled (> 400 long and short duplexes). Distinguishable DNA and proteins were counted by hand. Duplexes that were overlapped, indistinguishable, or cut off by the edge of the image were excluded from our counting procedure. For each sample, the binding density ratio, *r*, (see Eq. 5.1) is defined as the ratio of the proteins bound on long duplexes divided by proteins bound on short duplexes, which serve as an internal normalization factor to correct changes in concentration across samples that may confound results. Data presented are from representative trials, and error bars represent standard error of all trials based on the total number of proteins observed (n > 200 for all experiments). The differential binding density ratio, *dr*, (see Eq. 5.2) is calculated by dividing the *r* from the mismatched sample by the *r* from the well-matched sample.

$$r = \frac{\#\ of\ proteins\ on\ long\ duplexes}{\#\ of\ proteins\ on\ short\ duplexes} \qquad Eq. 5.1$$

$$dr = \frac{r_{mismatched}}{r_{well-matched}} = \frac{\left(\frac{\#\ of\ proteins\ on\ mismatched\ long\ duplexes}{\#\ of\ proteins\ on\ short\ duplexes}\right)}{\left(\frac{\#\ of\ proteins\ on\ well\text{-}matched\ long\ duplexes}{\#\ of\ proteins\ on\ short\ duplexes}\right)} \quad Eq. 5.2$$

Microscale Thermophoresis. Microscale thermophoresis (MST) was carried out using a Monolith NT.115 series instrument (NanoTemper) at 21 °C. Oligonucleotides (21 bp in length) based on the DNA sequence used in the AFM studies were synthesized and annealed to generate well-matched DNA of 21 bp in length. For measurements of EndoIII primarily in the reduced state, native EndoIII with His_6-tag (200 nM, 100 µL) was mixed with MO-L008 His-tag labeling kit RED-tris-NTA (100 nM, 100 µL, NanoTemper) for

30 min at room temperature. The sample was centrifuged at 4 °C and 15,000 g for 10 min. Serial dilution of dsDNA as titrants was performed in PCR 8-strip tubes with individual caps (USA Scientific) following the user manual provided by NanoTemper. Labeled protein (50 nM) was mixed with DNA titrant in the dark for 10 min. Samples with a final dye concentration of 25 nM were then loaded into MO-K003 Monolith NT.115 hydrophobic capillaries (NanoTemper) and were measured at 60% LED and 40% MST power. DNA buffer with 0.05% Tween 20 was used for MST studies. For measurements of EndoIII primarily in the oxidized state, EndoIII (1 µM, 200 µL) was oxidized in the absence of O_2 using DNA-modified electrode previously described. Oxidized EndoIII was labeled with RED-tris-NTA under anaerobic condition in an aluminum-wrapped Eppendorf tube. MST samples were loaded into hydrophobic capillary tubes inside a glove bag in the dark. Capillaries were sealed with HR4-328 capillary wax (Hampton Research) using a hand-held wax pen (Hampton Research) in the absence of O_2 and light.

DNA sequences used for MST measurements:

5'-ACT GAA CTC TGT ACC TGG CAC-3'

3'-TGA CTT GAG ACA TGG ACC GTG-5'

Isothermal Titration Calorimetry

Isothermal titration calorimetry (ITC) was carried out using a iTC200 MicroCalorimeter (MicroCal) at 21 °C. The DNA sequences used in ITC experiments were identical to the sequences used in MST experiments. For measurements of EndoIII primarily in the reduced state, native EndoIII (71 µM, 200 µL) was placed in the cell port and 21-mer (355 µM, 40 µL) was used as the titrant. For measurements of EndoIII primarily in the oxidized state, EndoIII (7.1 µM, 200 µL) was oxidized using a DNA-modified electrode in the glove bag previously described and the oxidized EndoIII solution was sealed in the glove bag with parafilm prior to transporting to the ITC instrument room. The oxidized EndoIII solution was then placed in the MicroCalorimeter cell port. 21-mer (71 µM, 40 µL) was used as the titrant. Residual glycerol in protein samples was removed via diafiltration using Ultracel centrifugal filters (10 kDa cutoff, Amicon Ultra). DNA titrant was dialyzed using Slide-A-Lyzer MINI dialysis units (2,000 MWCO, Thermo Scientific) against DNA buffer overnight, degassed with Ar, and centrifuged at 14,000 rpm to remove gas bubbles. Titrant was added in 16 successions (2.5 µL each) and the reaction mixture was allowed to equilibrate for 540 s between each addition. The stirring speed was kept at 1000 rpm.

DNA sequences used for ITC and EMSA measurements:

5'-ACT GAA CTC TGT ACC TGG CAC-3'

3'-TGA CTT GAG ACA TGG ACC GTG-5'   (complement)

Electrophoretic Mobility Shift Assay

Electrophoretic mobility shift assay (EMSA), also known as gel-shift assay, was conducted on radioactive hot benches. First, phosphorylation of the complement strand in the 21-mer (5 µM) used in MST and ITC experiments was carried out using radioactive [γ-32P]-labeled ATP (6000 Ci/mmol 150 mCi/ml Lead, 5 mCi, PerkinElmer) by T4 PNK (New England Biolabs) at 37 °C for 2 h and heat inactivated at 80 °C for 15 min. Radioactive 21-mer ssDNA was removed from the crude reaction containing unused ATP and denatured T4 PNK using Oligonucleotide Cleanup Kit (Monarch) by precipitating the 21-mer ssDNA onto the spin column using EtOH, then washed with 70% EtOH PE buffer solution for 3 times, and recovered using EB buffer (50 µL). Labeled 21-mer ssDNA was then gel-purified using a 20% polyacrylamide urea denaturing gel. The desired 21-mer ssDNA band was then visualized using an X-ray developer (Kodak) and excised using a razor blade. The excised band was re-dissolved in triethylammonium acetate buffer (TEAA, 100 mM, 1 mL) and incubated at 37 °C overnight. Water was removed from the reaction by SpeedVac and salt was removed by passing through Micro Bio-Spin 6 column (Bio-Rad) twice. Annealing titration between radio-labeled 21-mer complement strand and unlabeled 21-mer ssDNA that had been previously heated to 90 °C for 10 min and cooled to room temperature over a period of 3 h was conducted using 10% polyacrylamide native gel (Bio-Rad) at 4 °C and 50 V in 0.5X Tris/Borate/EDTA (TBE) buffer. Radioactively labeled 21-mer dsDNA was then degassed with Ar and incubated with native or oxidized EndoIII for 1 h in pH 7 DNA buffer with 20% glycerol to reach equilibrium under anaerobic condition. To quantify protein-DNA interaction, EMSA was then carried out using 10% polyacrylamide native gel (Bio-Rad) at 4 °C and 50 V in 0.5X TBE buffer inside the glove bag. The protein-DNA and DNA bands were transferred to a piece of Amersham Hybond-N nucleotide blotting paper (GE Healthcare) in transfer buffer (25 mM Tris-HCl, 200 mM glycine, 10% methanol, pH 8.5) using a HEP-1 Semidry Electroblotter (Thermo Scientific Owl). Exposure time was determined using a LS 6000SC Scintillation Counter (Beckman Coulter). The blotting film containing the transferred band was then exposed to a phosphorimaing storage screen (GE Healthcare) and imaged using a Typhoon FLA 9000 Imager (GE Healthcare).

Electrostatic Modeling. Distances between the [4Fe4S] cluster of EndoIII and the phosphate groups on the backbone of the DNA-bound EndoIII in the native state were obtained from a published crystal structure (PDB: 1ORN) (45). The 1ORN crystal structure also provided the number of phosphates interacting with protein residues. The dielectric constant of the portion of EndoIII of interest was estimated by calculating the average dielectric constant of the amino acid residues surrounding the [4Fe4S] cluster and in between the [4Fe4S] cluster and the bound DNA strand. In this electrostatic model, the [4Fe4S] cluster and the phosphate groups on the DNA backbone were modeled as point charges (46). The potential energy (PE) between two charged particles was calculated using Eq. 5.3

$$PE = \frac{(q_1)(q_2)}{4\,\pi\,\varepsilon_0\,\varepsilon_r\,d} \qquad Eq. 5.3$$

with q = charge, ε_0 = permittivity of free space, ε_r = dielectric constant, and d = distance between charges. The difference in

PE between EndoIII in the reduced and oxidized states was computed by calculating the difference between the total PE for the $[4Fe4S]^{3+}$ case and the total PE for the $[4Fe4S]^{2+}$ case. The experimental energy difference between the 3+ case and the 2+ case was calculated using the Nernst equation by converting the redox potential shift recorded using electrochemical techniques (34). The electrostatic model was supported by comparing the modeled PE and the experimental energy difference.

Results

Oxidation and Reduction of [4Fe4S] Proteins using Electrochemical Methods. Cyclic voltammetry (CV) was used to investigate the electrochemical properties of EndoIII on DNA-modified Au electrodes (Figure 5.1). These data, along with square wave voltammetry and differential pulse voltammetry measurements (Figures 5.2, 5.3) show that within our potential window EndoIII exhibits a single redox couple with a DNA-bound midpoint potential of about +80 mV vs NHE, consistent with previous measurements of the $[4Fe4S]^{2+/3+}$ redox couple in EndoIII when associated to DNA (34,35,39).

Solutions of primarily reduced or primarily oxidized EndoIII with an intact [4Fe4S] cluster were generated using bulk electrolysis and confirmed using electron paramagnetic resonance (EPR) and circular dichroism (CD) (Figure 5.4, 5.5). Randles-Sevcik analysis (Figures 5.6, 5.7) demonstrates that there is exchange between proteins in solution and on the surface of the DNA-modified electrode so that a constant applied potential could oxidize or reduce the majority of proteins in the sample. The CVs shown in Figure 5.1 identify potentials at which the [4Fe4S] clusters of the proteins can be oxidized or reduced, which allow us to conduct bulk electrochemical oxidation and reduction of EndoIII at +250 mV and –50 mV vs. NHE, respectively. Similar electrolysis experiments were utilized to examine primase using its [4Fe4S] cluster as a redox switch (47). Figure 5.1 also shows the oxidation of EndoIII on a DNA-modified electrode held at a constant potential for 25 min to drive electrolysis to completion. Applying an oxidizing

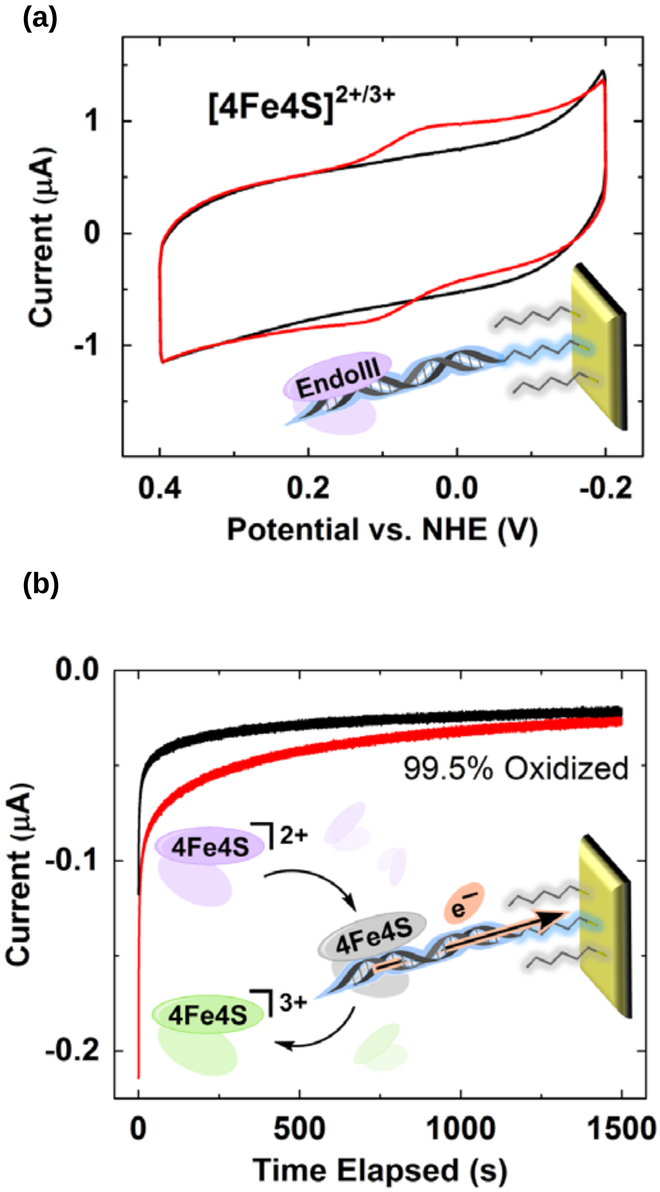

Figure 5.1 Electrochemistry of EndoIII on DNA-modified electrodes. (a) CVs at a scan rate of 100 mV/s and (b) bulk electrolysis held at +250 mV vs. NHE in DNA buffer (pH 7.0, 5 mM NaH_2PO_4, 50 mM NaCl) without (black) and with 1 µM EndoIII (red) using DNA-modified electrodes passivated with mercaptohexanol.

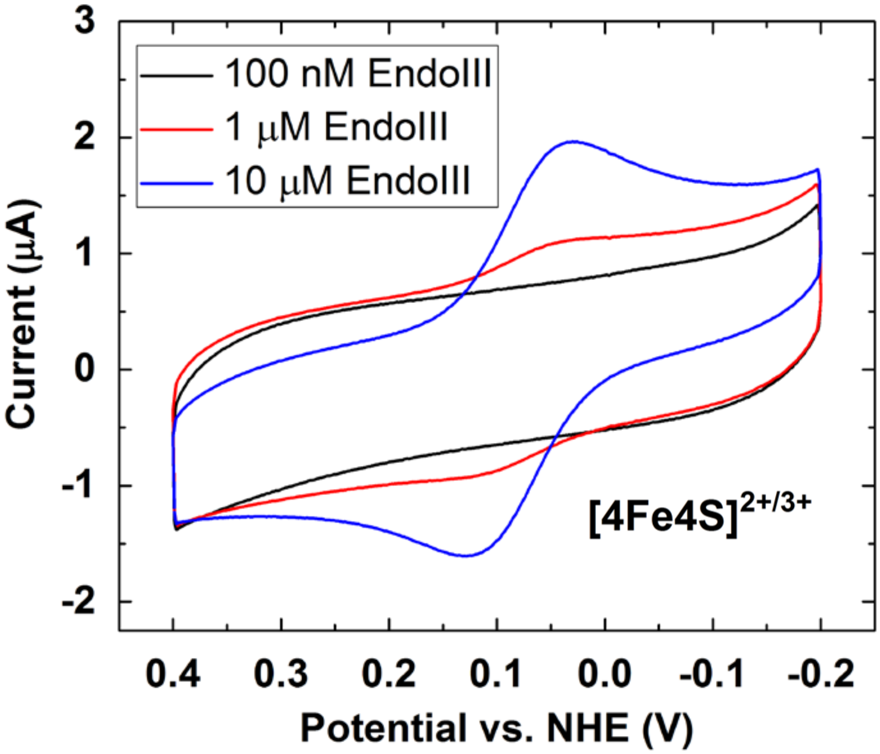

Figure 5.2 Cyclic voltammetry of EndoIII on a duplex DNA modified electrode. CVs in DNA buffer (pH 7.0, 5 mM NaH_2PO_4, 50 mM NaCl) with 100 nM EndoIII (black), 1 μM EndoIII (red), and 10 μM EndoIII (blue) added at a scan rate of 100 mV/s. E_{mid} = +80 mV vs. NHE.

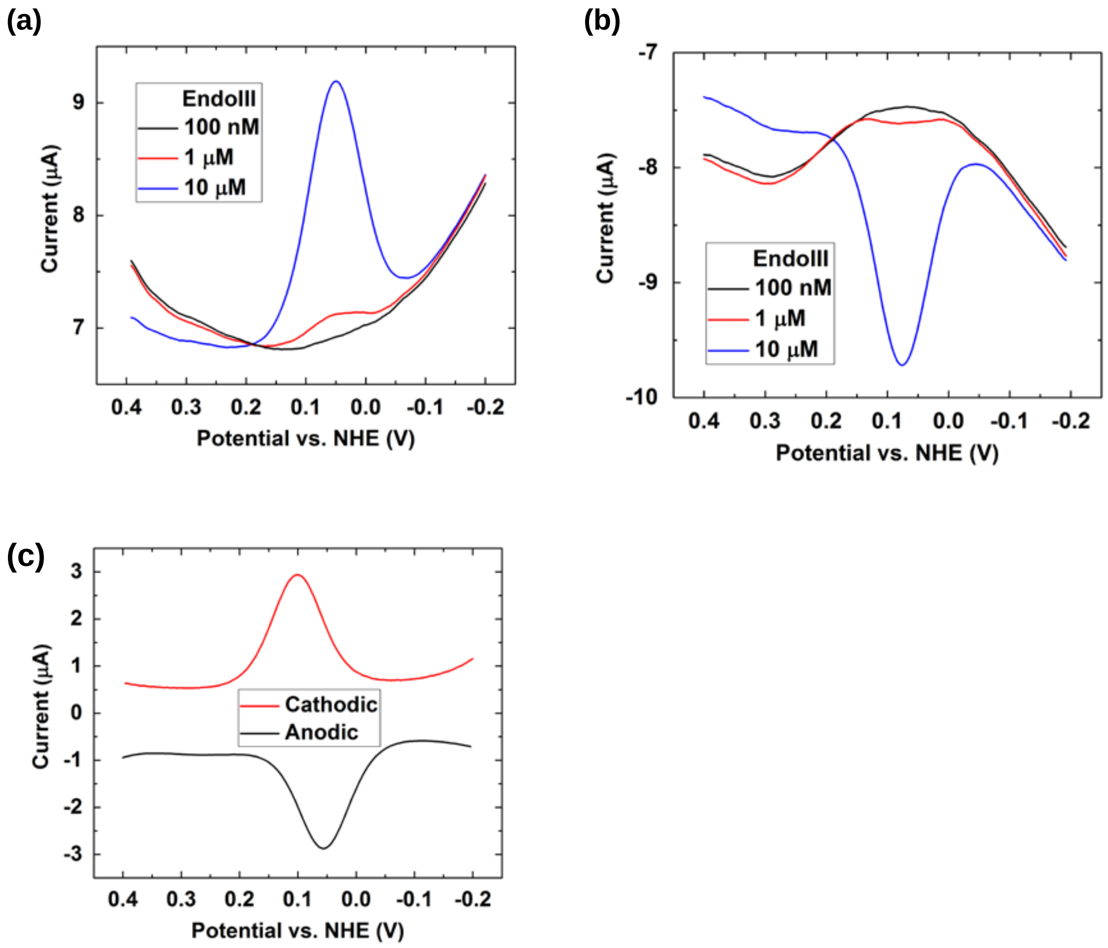

Figure 5.3 Square wave voltammetry (SWV) and differential pulse voltammetry (DPV) of EndoIII on a dsDNA modified electrode. (a) Cathodic and (b) anodic SWVs in DNA buffer (pH 7.0, 5 mM NaH_2PO_4, 50 mM NaCl) with 100 nM EndoIII (black), 1 µM EndoIII (red), and 10 µM EndoIII (blue) added. (C) Cathodic (red) and anodic (black) DPVs in DNA buffer (pH 7.0, 5 mM NaH_2PO_4, 50 mM NaCl) with 10 µM EndoIII added.

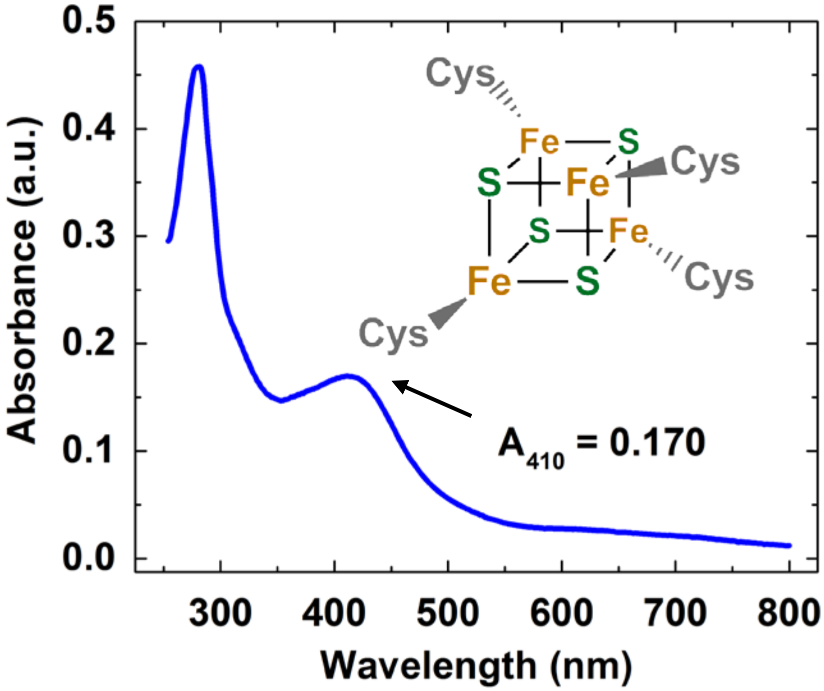

Figure 5.4 UV-visible absorbance spectra of EndoIII. The [4Fe4S] redox cofactor exhibits an $\mathcal{E}$ of 17,000 M^{-1} cm^{-1} at 410 nm. Cluster loading was at least 70%.

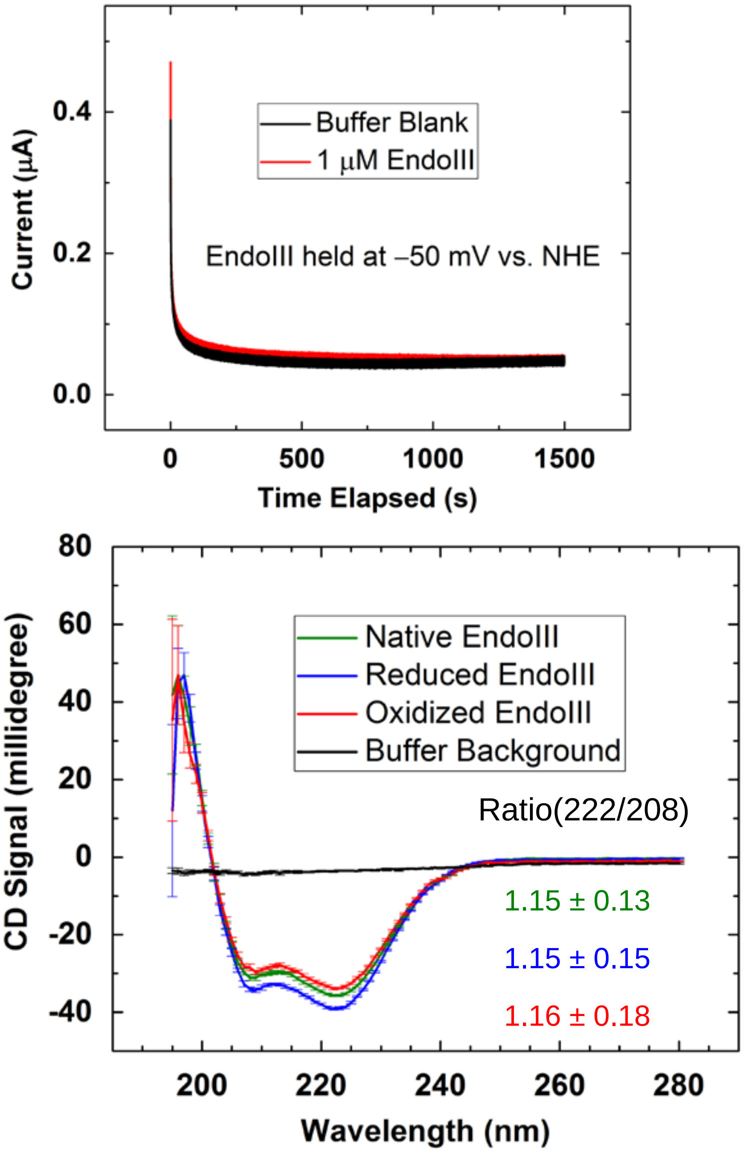

Figure 5.5. The influence of bulk electrolysis on EndoIII structure as monitored by circular dichroism. (Top) Bulk electrolysis in DNA buffer (pH 7.0, 5 mM NaH_2PO_4, 50 mM NaCl, black line) with 1 μM EndoIII added (red line) held at –50 mV vs. NHE. Only a small portion of the proteins present in the solution was reduced, suggesting that the native or as-isolated oxidation state of the protein is primarily in the reduced $[4Fe4S]^{2+}$ state. (Bottom) Circular dichroism spectra of DNA buffer (pH 7.0, 5 mM NaH_2PO_4, 50 mM NaCl, black line) with native (green), reduced (blue), and oxidized (red) EndoIII (5 μM, 1000 μL) added. The slight change in signal intensity is likely due to a change in the optical density. Measuring the ratio of the CD signal at 222 nm to that at 208 nm is typically used to analyze α-helical proteins. Coiled coils and isolated α-helix exhibit ratios of 1.1 and 0.9, respectively. Here, native, reduced, and oxidized EndoIII exhibit ratios of ca. 1.15, suggesting that EndoIII retains its coiled coils and that the overall structure of EndoIII is not perturbed by bulk electrolysis.

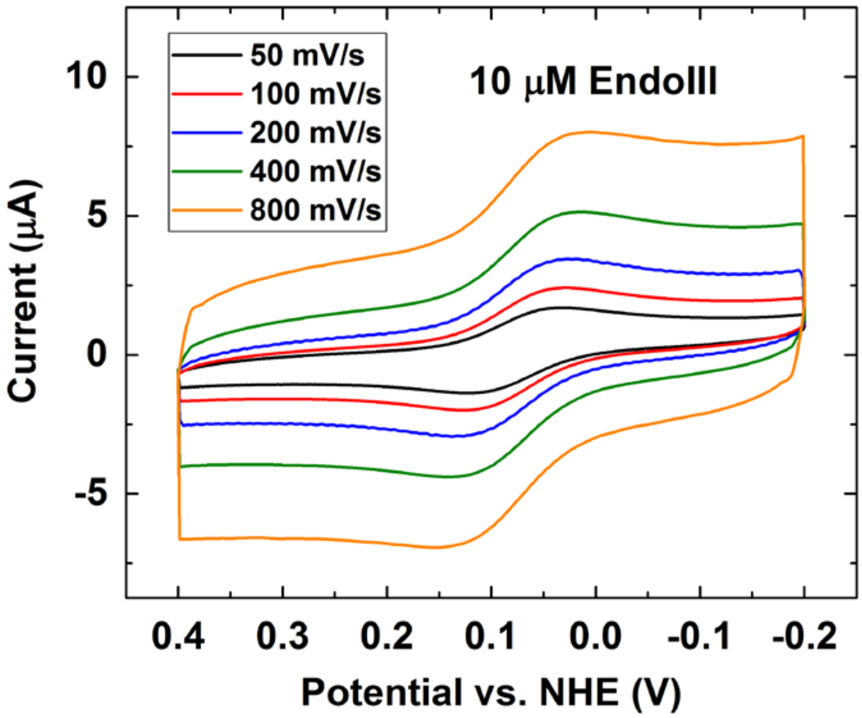

Figure 5.6. Cyclic voltammetry of EndoIII on a dsDNA modified electrode with varying scan rates. CVs in DNA buffer (pH 7.0, 5 mM NaH_2PO_4, 50 mM NaCl) with 10 µM EndoIII added at a scan rate of 50 (black), 100 (red), 200 (blue), 400 (green), and 800 (orange) mV/s. 10 µM is chosen as the concentration to allow for clear visualization of the redox waves.

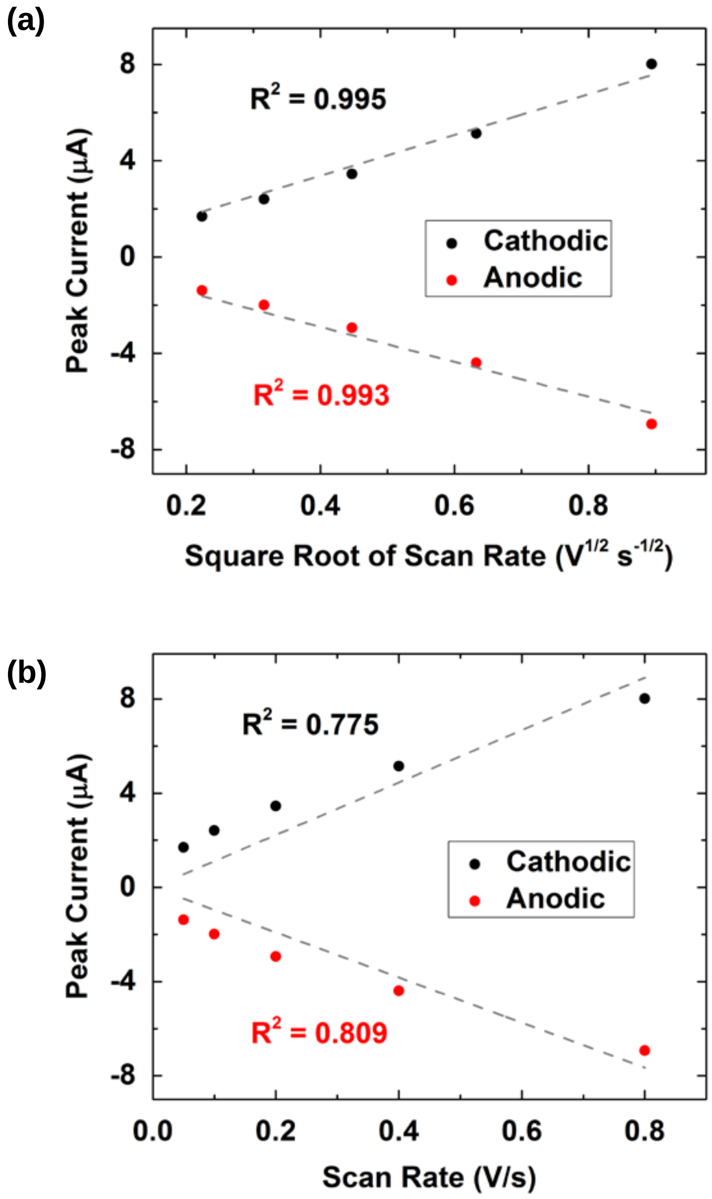

Figure 5.7. Randles-Sevcik plots of the peak currents of EndoIII. 10 μM EndoIII was plotted at various scan rates versus (a) the square root of the scan rate, and (b) the scan rate. The poor linear relationship observed for the Randles-Sevcik plot of EndoIII with the peak current versus the scan rate indicates that the redox event does not originate from a surface-bound species and that EndoIII does not adsorb very strongly onto DNA-modified electrodes under this condition. By contrast, the peak currents of both the anodic and cathodic peaks scale with the square root of the scan rate, indicating that under these conditions the redox reaction of EndoIII is in a diffusion-controlled regime. Therefore, at concentrations at or below 10 μM, EndoIII likely diffuses from the bulk solution to the electrode surface to undergo redox reaction upon binding to DNA and then diffuses back into the bulk solution to allow for freshly exposed DNA surfaces for other copies of EndoIII to approach and participate in subsequent redox events.

or reducing potential to a solution with protein present results in a larger magnitude current than measured in the buffer control (Figure 5.1). This difference is indicative of the proteins being oxidized or reduced on the DNA-modified electrode surface, and the current decreases over time as the oxidation or reduction approaches completion (> 99% yield). We then utilized EPR to characterize the reduced and oxidized EndoIII generated by bulk electrolysis (Figure 5.8). The reduced EndoIII is EPR-silent and the oxidized EndoIII exhibits an EPR signal with a g value of 2.07, which are consistent with $[4Fe4S]^{2+}$ and $[4Fe4S]^{3+}$ clusters, respectively (48).

Binding Affinity Measurements Comparing EndoIII with Oxidized and Reduced [4Fe4S] Cluster. AFM was used to explore how the DNA-binding activity of EndoIII changes as the amount of oxidized and reduced clusters in the protein sample was varied (Figure 5.9). We then recorded the number of EndoIII present on the linearized pUC19 plasmid DNA as a function of the proportion of oxidized $[4Fe4S]^{3+}$ cluster in the protein sample. As the ratio of EndoIII with oxidized $[4Fe4S]^{3+}$ metallocofactors increases, the number of EndoIII bound on DNA increases (Figure 5.9). This trend indicates that oxidized EndoIII binds more tightly to DNA than does the reduced protein. We then utilized electrophoretic mobility shift assay (EMSA), isothermal titration calorimetry (ITC), and microscale thermophoresis (MST) to probe the non-specific DNA-binding affinity of EndoIII to well-matched dsDNA of 21 bp in length. In all three cases, we observed an increase in binding affinity of EndoIII to dsDNA upon oxidizing the [4Fe4S] metallocofactor from the 2+ state to the 3+ state (Table 5.1).

ITC is not anaerobic and EMSA generates O_2 *in situ*, both of which result in cluster degradation that prevent accurate binding affinity measurements. EMSA is

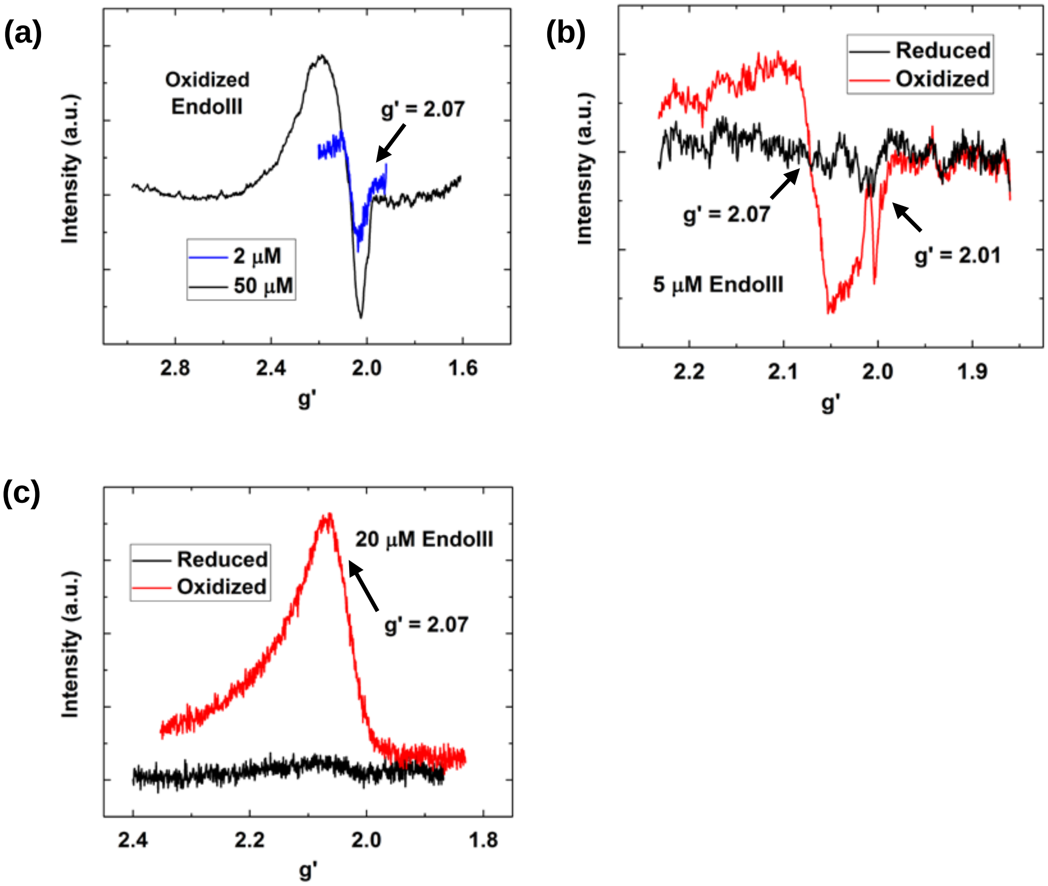

Figure 5.8 Continuous wave electron paramagnetic resonance spectra of EndoIII. (a) 2 μM (blue) and 50 μM (black) oxidized EndoIII prepared under anaerobic conditions, (b) reduced (black) and oxidized (red) 5 μM EndoIII exposed to ambient air, and (c) pulse electron spin echo envelope modulation (ESEEM) spectra of reduced (black) and oxidized (red) 20 μM EndoIII in protein buffer (20 mM NaH_2PO_4 pH 7.5, 100 mM NaCl, 5% glycerol, 1 mM EDTA). Instrument settings: modulation amplitude = 10 G at 100 kHz; frequency = 9.37 GHz; microwave power = 4.7 mW; and temperature = 10 K. for samples prepared under an N_2 atmosphere, an absence of an EPR signal with a g value of 2.01 indicates that no detectable $[3Fe4S]^{1+}$ degradation product was generated. As a positive control, for the oxidized EndoIII sample that was exposed to O_2 by passive diffusion in ambient air, we observed an EPR signal at a g value of 2.01, which is indicative of the presence of degraded $[3Fe4S]^{1+}$ clusters.

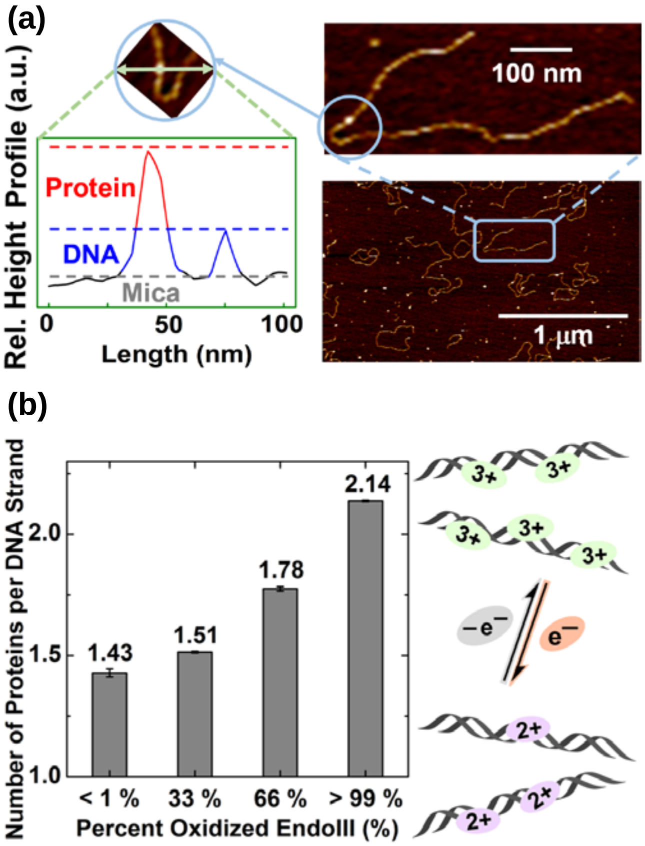

Figure 5.9 AFM visualization of EndoIII binding to DNA. (a) Visualization of proteins on DNA duplexes using AFM. The relative height of proteins allows for them to be distinguished from DNA and counted. (b) Plot of the amount of EndoIII bound on a DNA strand as a function of the extent of oxidation of the protein samples. The 33% and 66% oxidized EndoIII samples were prepared by mixing reduced and oxidized EndoIII in a 2:1 and 1:2 ratios, respectively. Curved lines in the schematic on the right represent linearized pUC19 DNA duplexes.

Table 5.1 Binding affinity measurements of EndoIII to 21-mer dsDNA in the reduced and oxidized forms using MST, ITC, and EMSA.

Method	K_D (Red)	K_D (Ox)	$\frac{K_D(\text{Red})}{K_D(\text{Ox})}$
MST	6.1 ± 0.9 μM	0.011 ± 0.002 μM	550 ± 130
ITC	3.3 ± 0.4 μM	0.12 ± 0.03 μM	28 ± 8
EMSA	19 ± 2 μM	5.9 ± 0.3 μM	3.2 ± 0.3

K_D (Red) and K_D (Ox) denote the DNA-binding affinities of proteins with $[4Fe4S]^{2+}$ and $[4Fe4S]^{3+}$ clusters, respectively. Variations in K_D obtained across the three techniques are likely due to differences in experimental conditions. (see S.I. for further discussion) DNA buffer (pH 7.0, 5 mM NaH_2PO_4, 50 mM NaCl) was used for all cases with the following modifications: for MST 0.05% Tween 20 was added and for EMSA 20% glycerol was added. The buffer ionic strength in all three cases was kept constant. MST was carried out at 21–24 °C using wax-sealed capillary tubes, ITC was conducted at 21 °C in air, and EMSA was conducted at 4 °C in an anaerobic glove bag. N > 3 for all three methods.

commonly used to measure the binding affinity between proteins and DNA. The EMSA experimental setup, even when conducted in an anaerobic chamber at 4 °C, is not compatible with oxidized EndoIII. The [4Fe4S] clusters of DNA repair proteins in the oxidized state degrade in the presence of O_2. Efforts including pre-running gel in degassed buffer and then switching to freshly-degassed buffer prior to protein loading were not successful. The amount of O_2 generated by the Pt electrodes during the gel running process resulted in cluster degradation. For an EMSA gel-shift experiment, about 20 pmol (10 µL per lane) of protein is typically used.

The amount of O_2 generated per second during a gel-shift experiment is about 10 µmol (= 50 V × 0.02 A × 1 s × 1 mol / 96485 C), and the total amount of O_2 generated over the course of a 4-hour EMSA gel-shift experiment is about 37 mmol. Since the solubility of O_2 in aqueous solution is about 1.2×10^{-6} mol cm^{-3}, the maximum amount of dissolved O_2 saturated in 1 L TBE buffer is ca. 1.2 mmol. The O2 diffusion coefficient in aqueous medium is about 1.9×10^{-5} cm^2 s^{-1}. The amount of O_2 liberated during a gel-shift experiment is more than enough to saturate the running buffer with O_2. Accordingly, oxidized EndoIII likely is overwhelmed by O_2 generated in situ during the gel running process. ITC measurements show a 28× increase in the affinity of the predominantly oxidized protein sample for DNA when compared to the predominantly reduced sample. However, instrument limitation prevented ITC from being operated anaerobically. We therefore switched to using MST to determine the DNA binding affinity of EndoIII. MST is a technique that allows for anaerobic determination of the binding affinity of O_2-sensitive proteins such as FeS cluster biogenesis machinery to their substrates.

We utilized MST to probe the binding affinity of EndoIII to DNA in different redox states. MST results show that oxidized EndoIII with [4Fe4S]3+ cluster binds 21-mer dsDNA 550 times stronger than EndoIII predominantly in the reduced state (Figure 5.10). This comparison may understate the true difference in affinity between the reduced and oxidized proteins, because it is unlikely that bulk electrolysis has completely removed all oxidized protein from the reduced sample. The presence of a small amount of oxidized protein will convolute the affinity measurement in any sample, even when the oxidized protein is in low concentration compared to the reduced protein, because the oxidized protein has a significantly higher affinity for DNA. This phenomenon infers that the values measured by MST that show a 550× change in affinity between the two protein redox states may be obfuscated by a change in the amount of oxidized protein present in the sample. Calculating the 99% confidence interval for the ratio of measured affinities suggests that the oxidized sample has between 276× and 1157× increase in affinity over the reduced sample.

To prevent cluster degradation, we utilized MST for anaerobic binding affinity measurement (49). MST results show that EndoIII predominantly in the reduced state exhibits a K_D of 6.1 µM ± 0.9 µM for unmodified duplex DNA and EndoIII predominantly in the oxidized state displays a K_D of 0.011 µM ± 0.002 µM. Thus, we observed a 550 ± 130 times increase in DNA-binding affinity of EndoIII upon oxidation, which further supports the trend observed using AFM that the EndoIII occupancy on DNA increases upon oxidation.

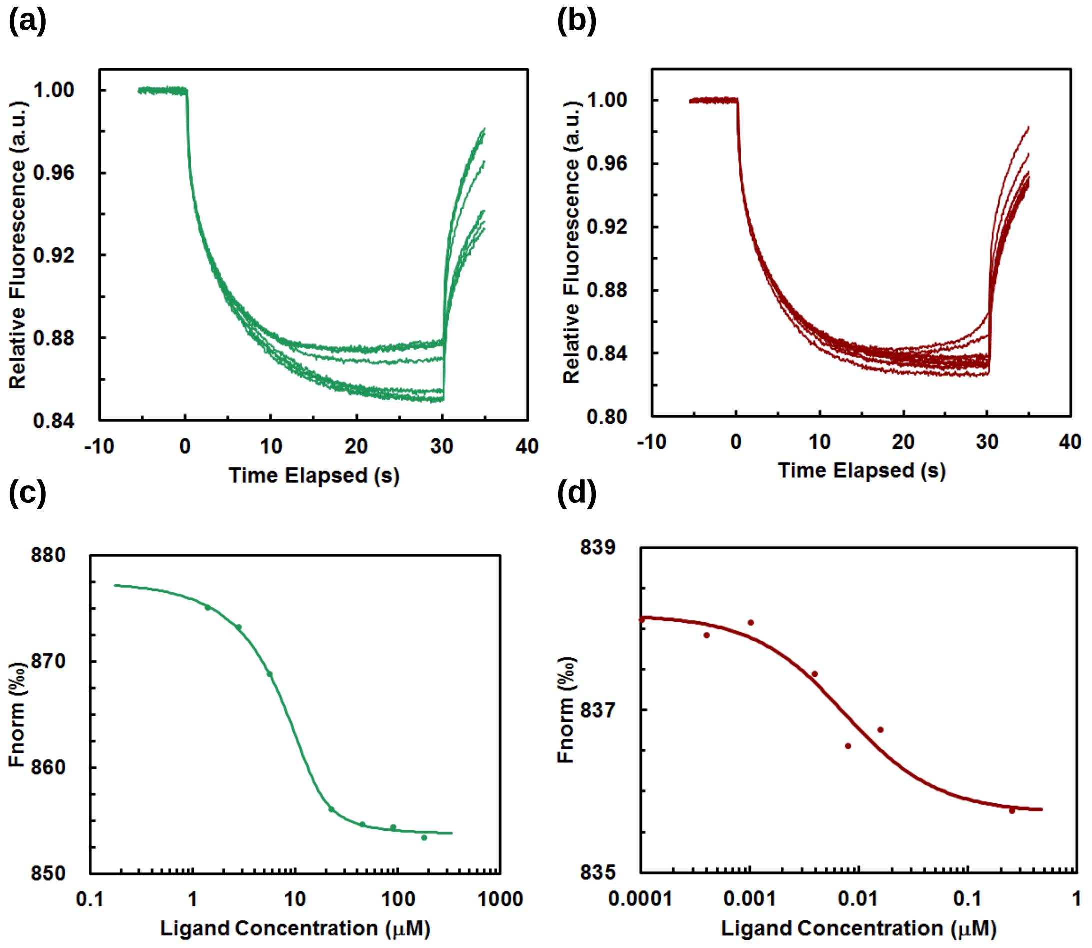

Figure 5.10. MST traces of native and oxidized EndoIII. MST plots of (c) native and (d) oxidized EndoIII. 21-mer was used as the titrant. A 550-fold increase in binding affinity was observed for EndoIII upon oxidation.

Electrostatic DNA-Protein Binding Model. To understand the origin of the redox-modulated affinity, we developed an electrostatic model that investigates the perturbation in the electrostatic interactions between DNA and proteins upon the addition or removal of an electron at the [4Fe4S] metallocofactor (Figure 5.11). This electrostatic model incorporates atomic distances obtained from crystallographic data and knowledge regarding the DNA-binding pocket from published literature (9,45,50). The crystal structure (PDB: 1ORN) revealed that eight negatively-charged phosphates on the DNA backbone not bound by cations interact with the amino acid residues of EndoIII. Another crystallographic study demonstrated that a high-potential iron-sulfur protein (HiPIP) undergoes only minor structural changes upon toggling the redox state of the [4Fe4S] cluster between 2+ and 3+ (51). Therefore, we assumed the coordinates of the atoms in the EndoIII protein structure are the same for both the $[4Fe4S]^{3+}$ and $[4Fe4S]^{2+}$ cases. The binding energy resulting from electrostatic interactions between the positively charged [4Fe4S] cluster and the negatively-charged phosphate groups on the DNA backbone are calculated to be ca. 7 kcal/mol, comparable to the energy change measured from the redox potential shift of EndoIII upon binding DNA using the Nernst equation, ca. 5 kcal/mol (52). This model shows that the difference in binding affinity for the two oxidation states, $[4Fe4S]^{2+}$ and $[4Fe4S]^{3+}$, can be explained primarily by the electrostatic interactions between the cluster and DNA without a substantial protein structural change.

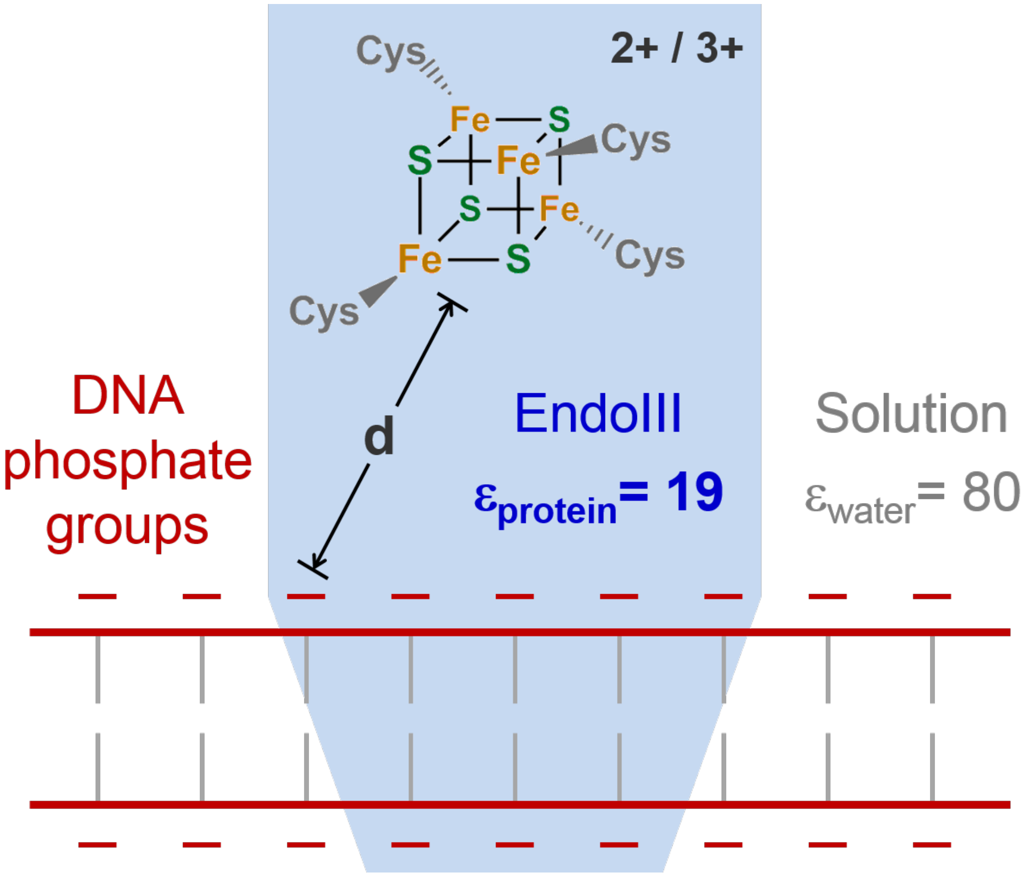

Figure 5.11 Model describing the electrostatic interactions between EndoIII and DNA. Eight phosphates on the DNA backbone interact with the amino acid residues of EndoIII. The average distance between the redox-active metallocofactor and the eight phosphate groups is about 18 Å. The neighboring phosphate groups that do not directly interact with the protein binding surface are not crucial in this calculation because (1) PE ∝ 1/d, (2) d increases for phosphate groups further away from the [4Fe4S] cluster, and (3) the dielectric constant (ε_r) between the two point charges needs to take into account of the intervening water molecules that have a ε_r of 80. The modeled ΔPE is ca. 7 kcal/mol, while the energy difference estimated from electrochemical studies is ca. 5 kcal/mol. Similar modeled ΔPE is also obtained for other DNA-processing proteins containing [4Fe4S] clusters or flavin cofactors, such as MutY, Dna2, and photolyase.

Signaling Between Oxidized and Reduced EndoIII to Search for DNA Damage. We then examined the effect of the redox state of the [4Fe4S] metallocofactor on the ability of EndoIII to differentiate between well-matched (WM) and mismatched (MM) DNA strands by AFM. Solutions of EndoIII with controlled amounts of oxidized $[4Fe4S]^{3+}$ cluster and reduced $[4Fe4S]^{2+}$ cluster were incubated with two different mixtures of DNA and then the two sets of AFM results were compared. The first DNA mixture contained long and short duplexes with no mismatches, while the second DNA mixture contained both short DNA duplexes with no mismatches and long DNA duplexes with a single C:A mismatch, which is not a native substrate for EndoIII but does inhibit DNA CT, engineered in the middle of the strand. The short WM DNA duplexes are identical in the two sets of experiments so the binding distribution profiles across the two data sets can be normalized and compared to one another (Table 5.2). Figure 5.12 shows a bar graph summarizing the ability for solutions of EndoIII with varying proportions of oxidized proteins to bind preferentially to DNA with a single-base mismatch. Here we observed that the ability for EndoIII to differentiate between MM and WM DNA strands decreases as the percentage of oxidized protein in the sample increases. It should be noted that these data could also be used to determine the change in binding affinity with oxidation. On this basis, we found a 4–30 fold increase in DNA-binding affinity upon oxidizing the [4Fe4S] cluster of EndoIII. The trend observed is consistent with that obtained using other techniques, but the magnitude of change is significantly smaller.

Condition	# of Short DNA	# of Proteins on Short DNA	Proteins: Short DNA	# of Long DNA	# of Proteins on Long DNA	Proteins: Long DNA
< 1 % Ox - MM	280	496	1.77	49	174	3.55
< 1 % Ox - WM	139	185	1.33	31	49	1.58
33 % Ox - MM	140	192	1.37	23	55	2.39
33 % Ox - WM	372	428	1.15	69	100	1.45
66 % Ox - MM	352	594	1.69	49	134	2.73
66 % Ox - WM	375	473	1.26	76	129	1.70
> 99 % Ox - MM	169	210	1.24	25	39	1.56
> 99 % Ox - WM	108	137	1.27	22	30	1.36

Table 5.2 Number of DNA and proteins counted in the AFM redistribution assay using EndoIII oxidized to various extent.

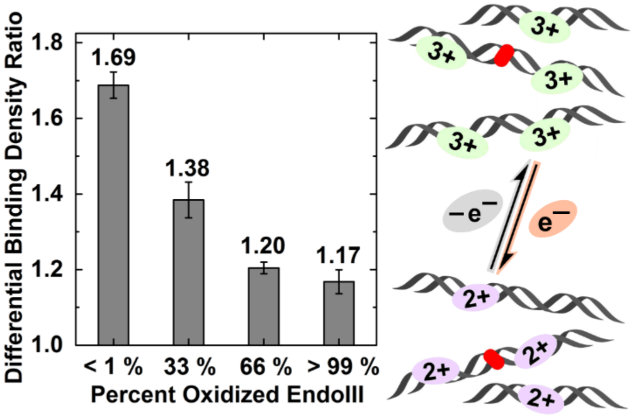

Figure 5.12 AFM redistribution assay of EndoIII samples oxidized to various extent. The 33% and 66% oxidized EndoIII samples were prepared by mixing reduced and oxidized EndoIII in a 2:1 and 1:2 ratios, respectively. In the schematic on the right, short curved lines, long curved lines, and long curved lines with a red feature in the middle represent short well-matched DNA duplexes, long well-matched DNA duplexes, and long DNA duplexes with a C:A mismatch engineered in the middle.

This difference likely can be attributed to the protein-DNA sample not being at equilibrium in the AFM experiment, because of kinetic limitations associated with tight DNA binding, precluding rapid, full redistribution of proteins along the DNA.

Signaling Between EndoIII and DinG to Search for DNA Damage. This change in binding density ratio, associated with a change in oxidation state, could be used as a diagnostic of oxidation state in the AFM experiment and therefore a means to identify redox signaling between proteins. We evaluate whether DinG, another DNA-processing enzyme containing a [4Fe4S] cluster, exhibits the same redox-modulated ability as EndoIII to bind preferentially to DNA duplexes with an intervening lesion. We chose to incorporate DinG because it has been shown to carry out DNA signaling with EndoIII; both proteins in the native oxidation state search for DNA damage *in vitro* and there is evidence that EndoIII helps DinG rescue defective growth *in vivo* (33). DinG exhibits a DNA-bound redox potential comparable to that of EndoIII (Figures 5.13 and 5.14) and also shows that the protein in solution exchanges with the surface similar to EndoIII (Figures 5.15 and 5.16). Thus we subjected DinG to bulk electrolysis conditions similar to EndoIII to generate DinG with oxidized and reduced [4Fe4S] metallocofactors. Analogous to EndoIII, oxidizing DinG decreases its ability to bind preferentially to DNA duplexes with a single-base mismatch (Figure 5.17).

Mixtures of reduced DinG and oxidized EndoIII, as well as mixtures of oxidized DinG and reduced EndoIII, were then prepared to address whether a reduced protein can signal with a different oxidized protein. This cross experiment includes four scenarios: two contain proteins at the 33% overall oxidized state, and two contain proteins at the

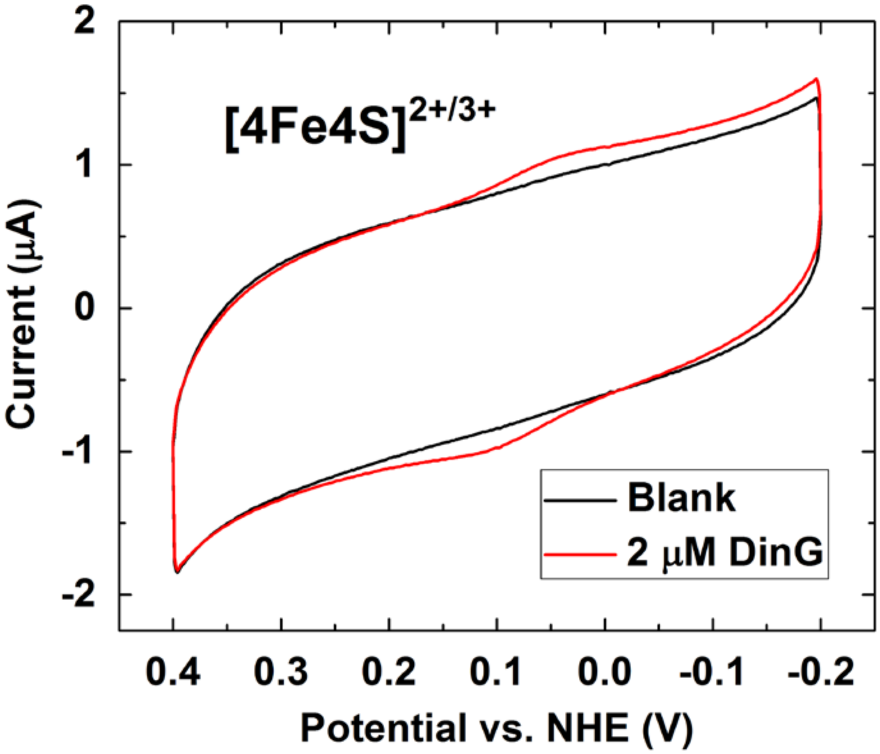

Figure 5.13 Cyclic voltammetry of DinG incubated with a dsDNA modified gold electrode. CVs in protein buffer (20 mM NaH_2PO_4 pH 7.5, 100 mM NaCl, 5% glycerol, 1 mM EDTA, black line) with 2 μM DinG added (red line) at a scan rate of 100 mV/s.

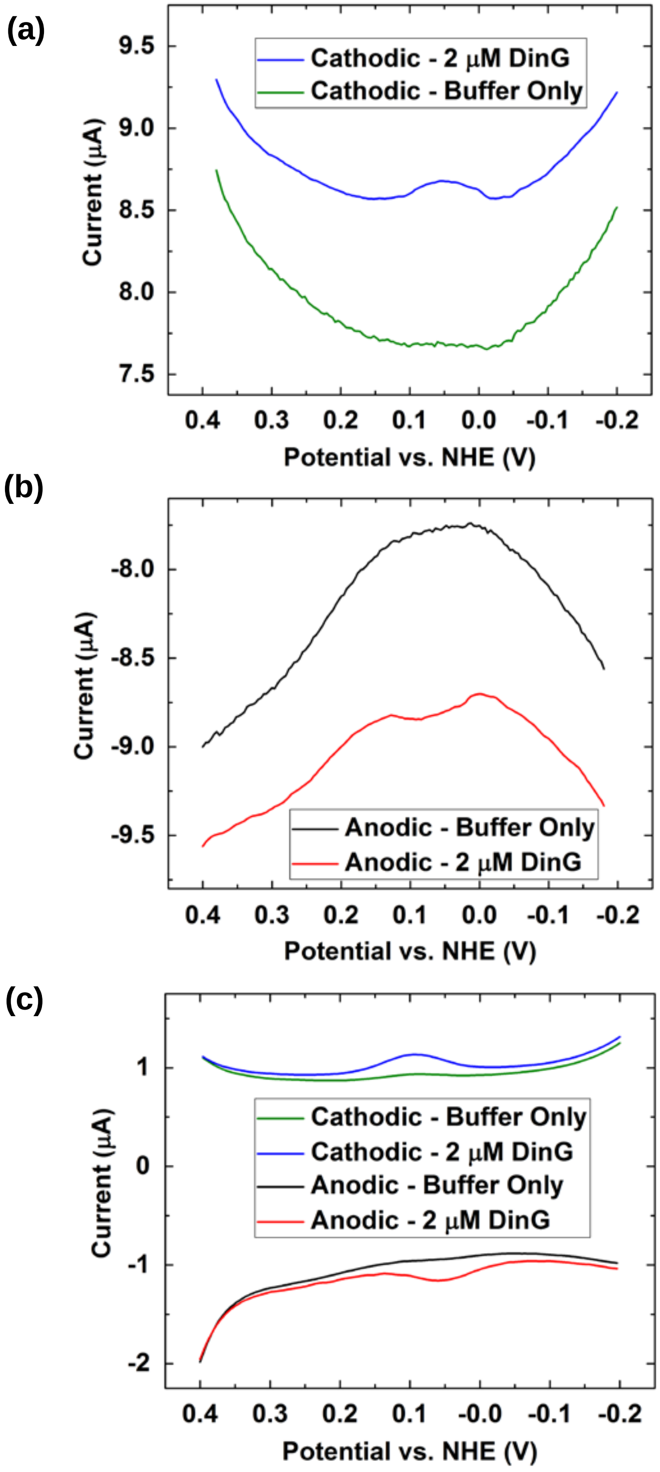

Figure 5.14 Squarewave and differential pulse voltammetry of DinG incubated on a duplex DNA modified gold electrode. (a) Cathodic SWVs, (b) anodic SWVs, and (c) cathodic and anodic DPVs in protein buffer (20 mM NaH_2PO_4 pH 7.5, 100 mM NaCl, 5% glycerol, 1 mM EDTA) with 2 μM DinG added.

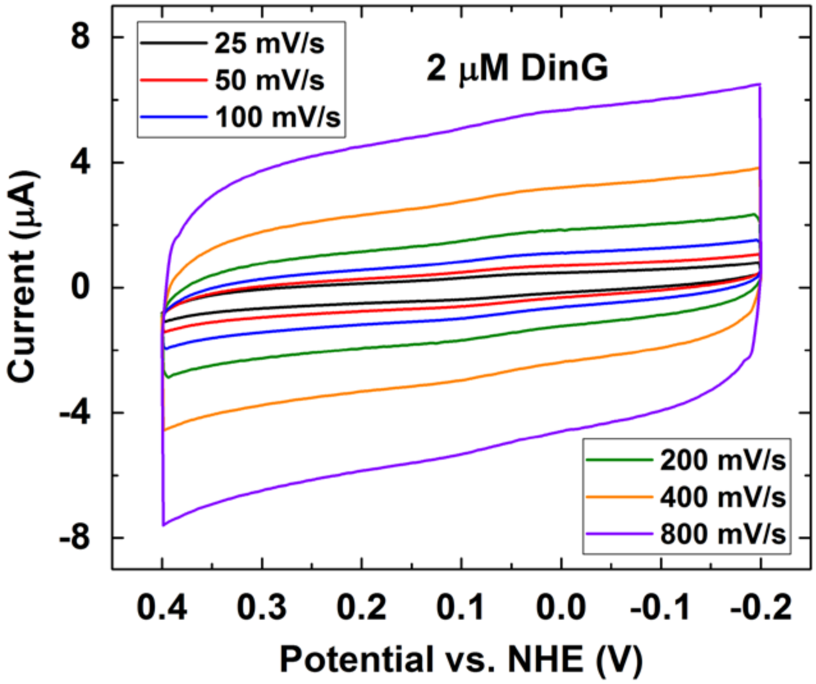

Figure 5.15 Cyclic voltammetry of DinG incubated with a dsDNA modified gold electrode at different scan rates. CVs in 2 μM DinG in protein buffer (20 mM NaH_2PO_4 pH 7.5, 100 mM NaCl, 5% glycerol, 1 mM EDTA) at a scan rate of 25 (black), 50 (red), 100 (blue), 200 (green), 400 (orange), and 800 (purple) mV/s.

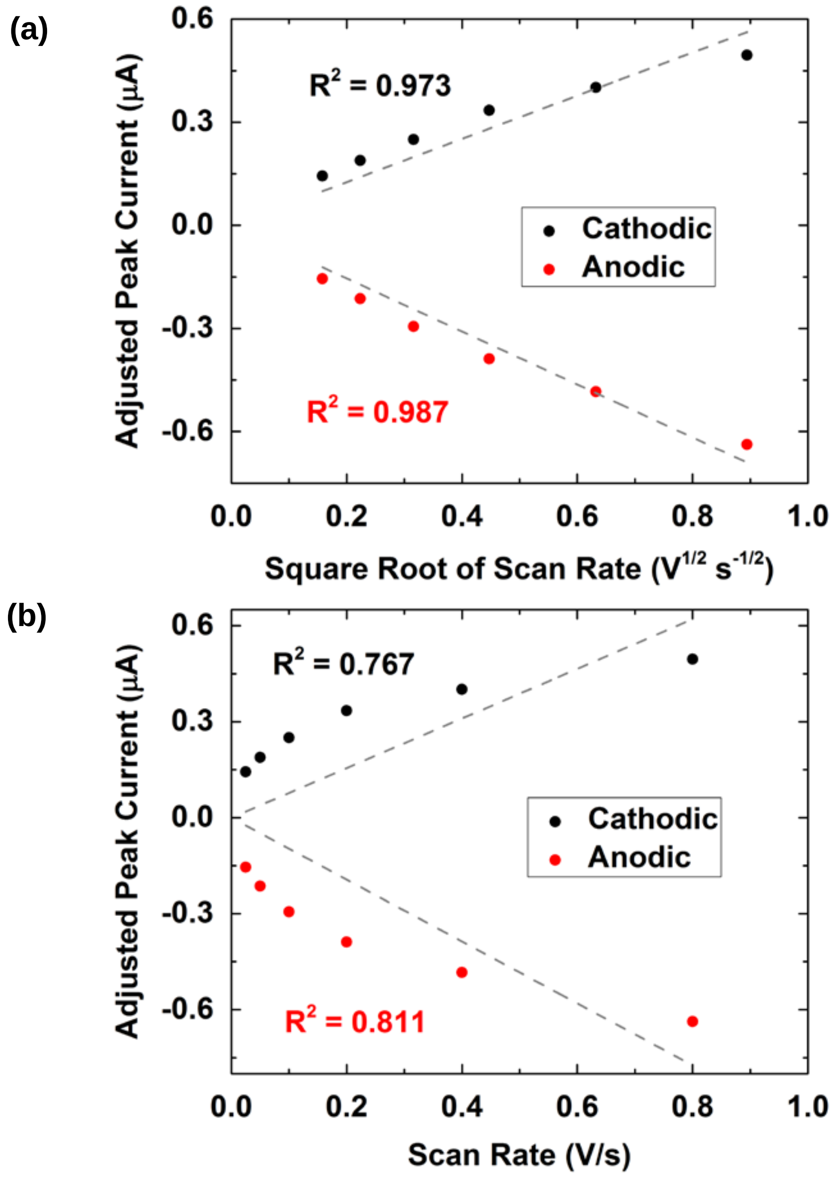

Figure 5.16 Randles-Sevcik plots of DinG electrochemistry. The background-subtracted peak currents of 2 μM DinG were plotted versus (a) the square root of the scan rate, and (b) the scan rate.

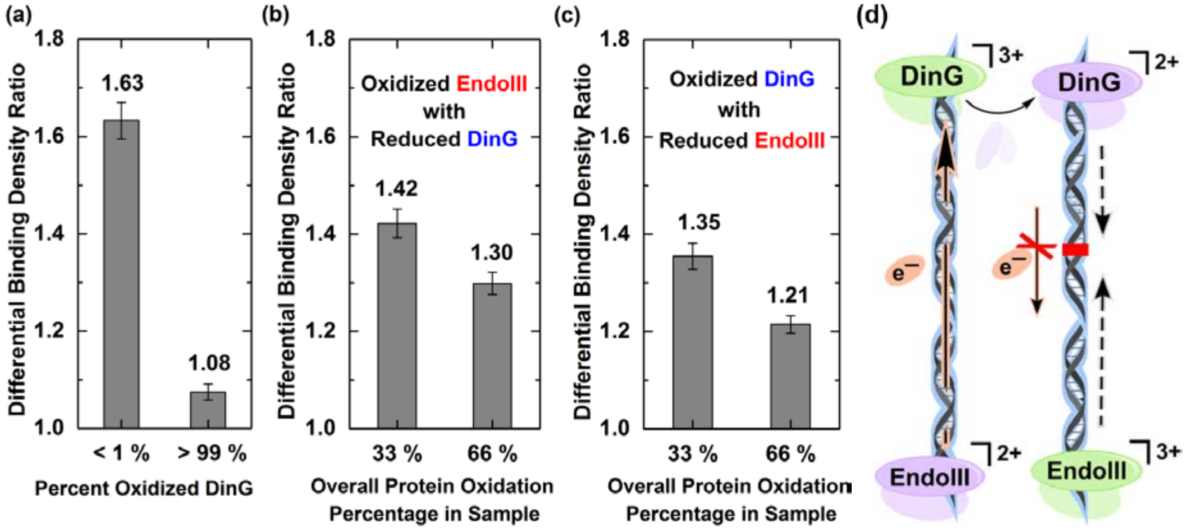

Figure 5.17 AFM redistribution assays for mixtures of DinG and EndoIII. Different protein mixturesmixtures were incubated with DNA: (a) oxidized and reduced DinG, (b) oxidized EndoIII with reduced DinG, and (c) oxidized DinG with reduced EndoIII. The 33% and 66% oxidized samples in (b) were prepared by mixing reduced DinG and oxidized EndoIII in a 2:1 and 1:2 ratios, respectively. The 33% and 66% oxidized samples in (c) were prepared by mixing reduced EndoIII and oxidized DinG in a 2:1 and 1:2 ratios, respectively. (d) Our proposed DNA damage search model for DNA-processing enzymes carrying redox-active [4Fe4S] clusters that uses DNA-mediated CT as the first step of damage detection. Reduction of the [4Fe4S] cluster through unperturbed WM DNA allows for proteins to release from the DNA and search elsewhere for damage. If, however, damage is present along the DNA, the protein will not be reduced and will localize in the vicinity of the DNA damage.

66% overall oxidized state. Figure 5.17 shows the results of the cross experiments. When the overall protein oxidation is either 33% and 66%, EndoIII and DinG exhibit intermediate binding density ratios in between the values obtained for predominantly reduced and predominantly oxidized protein samples. These findings demonstrate that reduced proteins from different repair pathways can undergo DNA-mediated redox signaling with oxidized proteins to collaboratively search for and preferentially bind to DNA duplexes with a single-base mismatch.

DISCUSSION

Redox-Active [4Fe4S] Cluster of Repair Proteins Functions as a DNA-Binding Affinity Switch. Non-specific binding to DNA is an important first step in the damage search and repair process (3-5,24). The binding affinity measurements reported in this work clearly indicate that the oxidized protein has an increased binding affinity for DNA relative to the reduced protein. This increased affinity is consistent with electrochemical results that previously demonstrated binding to DNA shifts the redox potential of the $[4Fe4S]^{2+/3+}$ couple of the cluster negative by about 200 mV, which indirectly showed that oxidation increases the protein/DNA binding affinity by at least two orders of magnitude (34,35,53,54).

We devised an electrostatic model to understand the underlying chemistry that dictates the apparent change in DNA-binding affinity. We assumed that changing redox state of the [4Fe4S] cluster does not significantly alter the structure of the protein, consistent with minimal structural changes observed in recent crystallographic studies on a HiPIP that is reduced or oxidized (51), EndoIII with and without DNA (9,45,50), and MutY spectroscopically examined with and without a cluster (15). Utilizing these structural data, we developed an electrostatic model to understand how the redox state of the [4Fe4S] cluster affects the charge-charge interaction. Crystallographic data confirms that EndoIII binds to the negatively-charged phosphate groups on the DNA backbone via a series of positively-charged residues (45). Our electrostatic model demonstrates that the redox-modulated DNA-binding affinity can be fully explained by the electrostatic interactions between the [4Fe4S] cluster and the phosphate groups on the DNA backbone without a significant structural change between oxidized and reduced DNA-bound forms.

Redox-Modulated DNA-Binding Affinity of [4Fe4S] Repair Proteins Regulates DNA-mediated CT Signaling. AFM experiments reveal that the oxidation state of the [4Fe4S] cluster influences the ability of the protein to localize on DNA duplexes with single-base mismatches. The total amount of oxidation is important for the efficiency of this DNA damage sensing process. Despite starting with oxidized protein that is unable to localize preferentially on mismatch-containing DNA, the addition of reduced protein with different enzymatic function is able to achieve preferential binding. Intriguingly, the amount of oxidized [4Fe4S] cluster among all proteins in a mixture is a better predictor of damage recognition than the identity of the proteins with initially reduced or oxidized [4Fe4S] metallocofactors; thus it can be used as a diagnostic of signaling between proteins.

To mimic cellular oxidative stress, our group previously used H_2O_2 to oxidize the [4Fe4S] cluster in EndoIII. These experiments found that H_2O_2 increases the preference of [4Fe4S] cluster proteins for DNA duplexes containing a mismatch (21). These results are fully consistent with the idea that repair proteins with $[4Fe4S]^{2+}$ clusters sense and respond to oxidative stress via cluster oxidation to the 3+ state. However, it is unclear what other effects the H_2O_2 may have on the proteins and DNA in this system. The electrochemical oxidation and reduction presented here provides a milder and well-controlled condition that allows for changing the redox state of [4Fe4s] clusters. Together, these data confirm that oxidative stress can generate repair proteins with $[4Fe4S]^{3+}$ clusters that can aid the DNA damage search. It is important to note that the short incubation time in both of these experiments, which was required for sample stability, means that the protein-DNA binding may not be at equilibrium. If anything, giving more time to equilibrate should result in higher preferential binding to the duplex with the mismatch.

These observations using AFM are consistent with a DNA damage search scheme based on DNA-mediated redox signaling between proteins with oxidized and reduced [4Fe4S] clusters (Figure 5.17). DNA-mediated CT can occur between two proteins and, our data shows conclusively, this CT results in a change in affinity for each of the proteins. Incorporating a single C:A mismatch within a DNA duplex, even though it is not a preferred substrate for either EndoIII or DinG (27,31), is able to increase the number of proteins bound to that duplex relative to a duplex with no mismatches. In these experiments the mismatch only serves to disrupt DNA CT between proteins and, therefore, DNA CT prevents the exchange of affinity that results from changing the redox state of the [4Fe4S] clusters. This change in redox state increases the effective affinity of these proteins for a duplex containing a mismatch because it allows for oxidized proteins to stay in the vicinity of the mismatch, or potentially any lesion that disrupts DNA CT, without being reduced and released from the duplex by another protein. These data bolster the claim that proteins, even with completely different cellular roles, can work in concert to aid their search for DNA damage by reducing and oxidizing one another via long-range CT through DNA (55-57).

Redox-Signaling Damage Search Model. DNA-mediated CT significantly expedites the search for DNA damage. Charge can be transported through large regions of DNA much faster than proteins can translocate, especially when the nuclear medium and DNA itself are crowded by other proteins (21). If a high-affinity, oxidized protein is bound to a region with no lesion, the protein may quickly become reduced by another protein along the duplex, and the decreased affinity will allow for it to release DNA and scan elsewhere (Figure 5.17). If, however, there is a lesion disrupting DNA CT, the protein will remain oxidized and associated to DNA. They can utilize both DNA CT and translocation making the search process faster and more efficient.

DNA-Mediated Redox Signaling Enables Low Copy Number Proteins to Efficiently Find Their Substrate. A growing number of proteins that process DNA have been discovered to contain redox-active [4Fe4S] clusters (7-10,20). Our data show that the oxidation state of the [4Fe4S] clusters is integral to the ability of proteins to search for DNA damage, but that the identity of the protein is unimportant for DNA-CT. The DNA-binding affinity depends on the oxidation state of the [4Fe4S] cluster in both EndoIII and DinG and likely holds true for other [4Fe4S] proteins. Importantly, this allows for DNA-processing proteins with different enzymatic functions to collaborate with each other to find damage so long as the [4Fe4S] clusters are in different redox states. This DNA-mediated redox signaling strategy between [4Fe4S] clusters may enable low copy number repair proteins to be aided by high copy number proteins to efficiently find and repair damage.

REFERENCES

(1) Jackson, S. P.; Bartek, J. The DNA-Damage Response in Human Biology and Disease. *Nature* **2009**, *461*, 1071−1078.

(2) Lindahl, T.; Barnes, D. E. Repair of Endogenous DNA Damage. *Cold Spring Harbor Symp. Quant. Biol.* **2000**, *65*, 127−134.

(3) Sancar, A.; Lindsey-Boltz, L. A.; Unsal-Kacmaz, K.; Linn, S. Molecular Mechanisms of Mammalian DNA Repair and the DNA Damage Checkpoints *Annu. Rev. Biochem.* **2004**, *73*, 39−85.

(4) Marteijn, J. A.; Lans, H.; Vermeulen, W.; Hoeijmakers, J. H. J. Understanding Nucleotide Excision Repair and Its Roles in Cancer and Ageing. *Nat. Rev. Mol. Cell. Biol.* **2014**, *15*, 465−481.

(5) David, S. S.; O'Shea, V. L.; Kundu, S. Base-Excision Repair of Oxidative DNA Damage. *Nature* **2007**, *447*, 941−950.

(6) Hoeijmakers, J. H. J. Genome Maintenance Mechanisms for Preventing Cancer. *Nature* **2001**, *411*, 366−374.

(7) Fuss, J. O.; Tsai, C.-L.; Ishida, J. P.; Tainer, J. A. Emerging Critical Roles of Fe–S Clusters in DNA Replication and Repair. *BBA-Mol. Cell Res.* **2015**, *1853*, 1253−1271.

(8) Rouault, T. A. Iron-Sulfur Proteins Hiding in Plain Sight. *Nat. Chem. Biol.* **2015**, *11*, 442−445.

(9) Kuo, C.; McRee, D.; Fisher, C.; O'Handley, S.; Cunningham, R.; Tainer, J. Atomic Structure of the DNA Repair [4Fe-4S] Enzyme Endonuclease III. *Science* **1992**, *258*, 434−440.

(10) Fan, L.; Fuss, J. O.; Cheng, Q. J.; Arvai, A. S.; Hammel, M.; Roberts, V. A.; Cooper, P. K.; Tainer, J. A. XPD Helicase Structures and Activities: Insights into the Cancer and Aging Phenotypes from XPD Mutations. *Cell* **2008**, *133*, 789−800.

(11) Lukianova, O. A.; David, S. S. A Role for Iron–Sulfur Clusters in DNA Repair. *Curr. Opin. Chem. Biol.* **2005**, *9*, 145−151.

(12) Veatch, J. R.; McMurray, M. A.; Nelson, Z. W.; Gottschling, D. E. Mitochondrial Dysfunction Leads to Nuclear Genome Instability Via an Iron-Sulfur Cluster Defect. *Cell* **2009**, *137*, 1247−1258.

(13) Saxena, N.; Maio, N.; Crooks, D. R.; Ricketts, C. J.; Yang, Y.; Wei, M.-H.; Fan, T. W. M.; Lane, A. N.; Sourbier, C.; Singh, A.; Killian, J. K.; Meltzer, P. S.; Vocke, C. D.; Rouault, T. A.; Linehan, W. M. SDHB-Deficient Cancers: The Role of Mutations That Impair Iron Sulfur Cluster Delivery. *J. Natl. Cancer Inst.* **2016**, *108,* djv287.

(14) Wu, Y.; Suhasini, A. N.; Brosh, R. M. Welcome the Family of FANCJ-Like Helicases to the Block of Genome Stability Maintenance Proteins. *Cell. Mol. Life Sci.* **2009**, *66*, 1209−1222.

(15) Golinelli, M.-P.; Chmiel, N. H.; David, S. S. Site-Directed Mutagenesis of the Cysteine Ligands to the [4Fe−4S] Cluster of Escherichia Coli MutY. *Biochemistry* **1999**, *38*, 6997−7007.

(16) Lill, R. Function and Biogenesis of Iron–Sulphur Proteins. *Nature* **2009**, *460*, 831−838.

(17) Stehling, O.; Vanshisht, A. A.; Mascarenhas, J.; Jonsson, Z. O.; Sharma, T.; Netz, D. J.; Pierik, A. J.; Wohlschlegel, J. A.; Lill, R. MMS19 Assembles Iron-Sulfur Proteins Required for DNA Metabolism and Genomic Instability. *Science* **2012**, *337*, 195−199.

(18) Gari, K.; León Ortiz, A. M.; Borel, V.; Flynn, H.; Skehel, J. M.; Boulton, S. J. MMS19 Links Cytoplasmic Iron-Sulfur Cluster Assembly to DNA Metabolism. *Science* **2012**, *337*, 243−245.

(19) Rouault, T. A. Mammalian Iron-Sulphur Proteins: Novel Insights into Biogenesis and Function. *Nat. Rev. Mol. Cell. Biol.* **2015**, *16*, 45−55.

(20) Rouault, T. A. Biogenesis of Iron-Sulfur Clusters in Mammalian Cells: New Insights and Relevance to Human Disease. *Dis. Model. Mech.* **2012**, *5*, 155−164.

(21) Boal, A. K.; Genereux, J. C.; Sontz, P. A.; Gralnick, J. A.; Newman, D. K.; Barton, J. K. Redox Signaling between DNA Repair Proteins for Efficient Lesion Detection. *Proc. Natl. Acad. Sci. USA* **2009**, *106*, 15237−15242.

(22) Demple, B.; Harrison, L. Repair of Oxidative Damage to DNA: Enzymology and Biology. *Annu. Rev. Biochem.* **1994**, *63*, 915−948.

(23) Li, G.-W.; Burkhardt, D.; Gross, C.; Weissman, Jonathan S. Quantifying Absolute Protein Synthesis Rates Reveals Principles Underlying Allocation of Cellular Resources. *Cell* **2014**, *157*, 624−635.

(24) O'Brien, E.; Silva, R. M. B.; Barton, J. K. Redox Signaling through DNA. *Isr. J. Chem.* **2016**, *56*, 705−723.

(25) Sontz, P. A.; Mui, T. P.; Fuss, J. O.; Tainer, J. A.; Barton, J. K. DNA Charge Transport as a First Step in Coordinating the Detection of Lesions by Repair Proteins. *Proc. Natl. Acad. Sci. USA* **2012**, *109*, 1856−1861.

(26) Genereux, J. C.; Barton, J. K. Mechanisms for DNA Charge Transport. *Chem. Rev.* **2010**, *110*, 1642−1662.

(27) Kelley, S. O.; Jackson, N. M.; Hill, M. G.; Barton, J. K. Long-Range Electron Transfer through DNA Films. *Angew. Chem. Int. Ed.* **1999**, *38*, 941−945.

(28) Guo, X.; Gorodetsky, A. A.; Hone, J.; Barton, J. K.; Nuckolls, C. Conductivity of a Single DNA Duplex Bridging a Carbon Nanotube Gap. *Nat. Nanotechnol.* **2008**, *3*, 163−167.

(29) Boal, A. K.; Barton, J. K. Electrochemical Detection of Lesions in DNA. *Bioconjugate Chem.* **2005**, *16*, 312-321.

(30) Bhattacharya, P. K.; Barton, J. K. Influence of Intervening Mismatches on Long-Range Guanine Oxidation in DNA Duplexes. *J. Am. Chem. Soc.* **2001**, *123*, 8649−8656.

(31) Boon, E. M.; Livingston, A. L.; Chmiel, N. H.; David, S. S.; Barton, J. K. DNA-Mediated Charge Transport for DNA Repair. *Proc. Natl. Acad. Sci. USA* **2003**, *100*, 12543−12547.

(32) Slinker, J. D. M., N. B.; Renfrew, S. E.; Barton, J. K. DNA Charge Transport over 34 nm. *Nat. Chem.* **2011**, *3*, 230−235.

(33) Grodick, M. A.; Segal, H. M.; Zwang, T. J.; Barton, J. K. DNA-Mediated Signaling by Proteins with 4Fe-4S Clusters Is Necessary for Genomic Integrity. *J. Am. Chem. Soc.* **2014**, *136*, 6470−6478.

(34) Gorodetsky, A. A.; Boal, A. K.; Barton, J. K. Direct Electrochemistry of Endonuclease III in the Presence and Absence of DNA. *J. Am. Chem. Soc.* **2006**, *128*, 12082−12083.

(35) Bartels, P. L.; Zhou, A.; Arnold, A. R.; Nuñez, N. N.; Crespilho, F. N.; David, S. S.; Barton, J. K. Electrochemistry of the [4Fe4S] Cluster in Base Excision Repair Proteins: Tuning the Redox Potential with DNA. *Langmuir* **2017**, *33*, 2523−2530.

(36) Boubakri, H.; de Septenville, A. L.; Viguera, E.; Michel, B. The Helicases Ding, Rep and Uvrd Cooperate to Promote Replication across Transcription Units *in vivo*. *EMBO J.* **2010**, *29*, 145−157.

(37) Grodick, M. A.; Muren, N. B.; Barton, J. K. DNA Charge Transport within the Cell. *Biochemistry* **2015**, *54*, 962−973.

(38) O'Handley, S.; Scholes, C. P.; Cunningham, R. P. Endonuclease III Interactions with DNA Substrates. 1. Binding and Footprinting Studies with Oligonucleotides Containing a Reduced Apyrimidinic Site. *Biochemistry* **1995**, *34*, 2528−2536.

(39) Boal, A. K.; Yavin, E.; Lukianova, O. A.; O'Shea, V. L.; David, S. S.; Barton, J. K. DNA-Bound Redox Activity of DNA Repair Glycosylases Containing [4Fe-4S] Clusters. *Biochemistry* **2005**, *44*, 8397−8407.

(40) Slinker, J. D.; Muren, N. B.; Gorodetsky, A. A.; Barton, J. K. Multiplexed DNA-Modified Electrodes. *J. Am. Chem. Soc.* **2010**, *132*, 2769−2774.

(41) Kelley, S. O.; Barton, J. K.; Jackson, N. M.; Hill, M. G. Electrochemistry of Methylene Blue Bound to a DNA-Modified Electrode. *Bioconjugate Chem.* **1997**, *8*, 31−37.

(42) Cunningham, R. P.; Asahara, H.; Bank, J. F.; Scholes, C. P.; Salerno, J. C.; Surerus, K.; Munck, E.; McCracken, J.; Peisach, J.; Emptage, M. H. Endonuclease III Is an Iron-Sulfur Protein. *Biochemistry* **1989**, *28*, 4450−4455.

(43) Bard, A. J.; Faulkner, L. R. *Electrochemical Methods: Fundamentals and Applications*; Wiley, 2000.

(44) Venkateswara Rao, P.; Holm, R. H. Synthetic Analogues of the Active Sites of Iron−Sulfur Proteins. *Chem. Rev.* **2004**, *104*, 527−560.

(45) Fromme, J. C.; Verdine, G. L. Structure of a Trapped Endonuclease III–DNA Covalent Intermediate. *EMBO J.* **2003**, *22*, 3461−3471.

(46) Li, L.; Li, C.; Zhang, Z.; Alexov, E. On the Dielectric “Constant” of Proteins: Smooth Dielectric Function for Macromolecular Modeling and Its Implementation in Delphi. *J. Chem. Theory Comput.* **2013**, *9*, 2126−2136.

(47) O’Brien, E.; Holt, M. E.; Thompson, M. K.; Salay, L. E.; Ehlinger, A. C.; Chazin, W. J.; Barton, J. K. The [4Fe4S] Cluster of Human DNA Primase Functions as a Redox Switch Using DNA Charge Transport. *Science* **2017**, *355*, 813−822.

(48) Agarwalla, S.; Stroud, R. M.; Gaffney, B. J. Redox Reactions of the Iron-Sulfur Cluster in a Ribosomal RNA Methyltransferase, Ruma: Optical and Epr Studies. *J. Biol. Chem.* **2004**, *279*, 34123−34129.

(49) Webert, H.; Freibert, S.-A.; Gallo, A.; Heidenreich, T.; Linne, U.; Amlacher, S.; Hurt, E.; Mühlenhoff, U.; Banci, L.; Lill, R. Functional Reconstitution of Mitochondrial Fe/S Cluster Synthesis on Isu1 Reveals the Involvement of Ferredoxin. *Nat. Commun.* **2014**, *5*, 5013.

(50) Thayer, M. M.; Ahern, H.; Xing, D.; Cunningham, R. P.; Tainer, J. A. Novel DNA Binding Motifs in the DNA Repair Enzyme Endonuclease III Crystal Structure. *EMBO J.* **1995**, *14*, 4108−4120.

(51) Ohno, H.; Takeda, K.; Niwa, S.; Tsujinaka, T.; Hanazono, Y.; Hirano, Y.; Miki, K. Crystallographic Characterization of the High-Potential Iron-Sulfur Protein in the Oxidized State at 0.8 Å Resolution. *PLoS ONE* **2017**, *12*, e0178183.

(52) Atkins, P.; de Paula, J. *Atkins' Physical Chemistry*; OUP Oxford, 2010.

(53) Boon, E. M.; Pope, M. A.; Williams, S. D.; David, S. S.; Barton, J. K. DNA-Mediated Charge Transport as a Probe of MutY/DNA Interaction. *Biochemistry* **2002**, *41*, 8464−8470.

(54) Boal, A. K.; Yavin, E.; Barton, J. K. DNA Repair Glycosylases with a [4Fe-4S] Cluster: A Redox Cofactor for DNA-Mediated Charge Transport? *J. Inorg. Biochem.* **2007**, *101*, 1913−1921.

(55) Merino, E. J.; Boal, A. K.; Barton, J. K. Biological Contexts for DNA Charge Transport Chemistry. *Curr. Opin. Chem. Biol.* **2008**, *12*, 229−237.

(56) Arnold, A. R.; Grodick, M. A.; Barton, J. K. DNA Charge Transport: From Chemical Principles to the Cell. *Cell Chem. Biol.* **2016**, *23*, 183−197.

(57) Genereux, J. C.; Boal, A. K.; Barton, J. K. DNA-Mediated Charge Transport in Redox Sensing and Signaling. *J. Am. Chem. Soc.* **2010**, *132*, 891

Chapter 6

Summary and Perspective

DNA-mediated charge transport (DNA CT) is well established in both ground and excited state systems. DNA CT arises from the physical structure and dynamics of DNA, so it is intriguing to consider how these structures, or perturbations to these structures, may impart other exciting and useful characteristics. In particular, the integrity of the extended π-stack of the aromatic heterocycles, the nucleic acid bases, plays a critical role in facilitating DNA CT. Electron donors and acceptors must be electronically well coupled into the π-stack, typically via intercalation, and perturbations that distort the π-stack, such as single-base mismatches, abasic sites, base lesions, and protein binding that kinks the double helix, attenuate DNA CT dramatically.

This thesis work describes experiments that expand the understanding of how the structural changes to DNA may influence its function. Although previous work using dry DNA in air or under vacuum indicated that DNA could filter spin, it was unclear whether this spin selectivity would translate to hydrated DNA. We developed experiments to test for spin selective charge transport on a DNA-modified ferromagnetic electrode. Magnetizing the electrode changed the proportion of spin up and spin down electrons that were injected into the DNA, and also changed the yield of charge transport to intercalated redox probes. Our experiments thus demonstrate that magnetic fields can affect the flow of electrons through native, hydrated dsDNA.

Significantly, our data show that spin selectivity is observed only at films containing duplex DNA and with redox probes intercalated into the π-stack that undergo DNA-mediated CT. Magnetic field effects are not observed with redox reporters bound electrostatically to the DNA duplex nor with tethered reporters that contact the surface directly. These data emphasize that DNA-mediated CT is necessary for the observed spin selectivity. It is not simply the electrostatic helical field that is responsible for the spin selectivity. Nor is it simply the chiral centers on the DNA; redox reporters bound to single stranded DNA do not show magnetic field effects. As with DNA CT, the extended π-stack appears to play a crucial role: reversing the handedness of the helix in the films generates a diode-like spin-filtering response. It is interesting to consider how conformational changes such as that between B- and Z-DNA might be utilized as a diode in organic spintronics and how this spin filtering might be applied in practical devices.

This exquisite spin selectivity begged the question: how might biology take advantage of such a spin filter? This question led to electrochemical studies that monitor the repair of cyclobutane pyrimidine dimer lesions by *E coli* photolyase and truncated *A Thaliana* Cryptochrome 1 with an applied magnetic field. We find that the yield of dimer repair is dependent on the strength and angle of the applied magnetic field even when using magnetic fields weaker than 1 Gauss, though spin selective DNA CT is not found to be involved.

These experiments illustrate how nature can design a magnetic field compass that functions at weak field strengths. Experiments with photolyase active site mutants and uracil-containing lesions show that the chemistry involved in the repair of cyclobutane pyrimidine dimers (CPD) is the likely source of magnetosensitivity that we observe. These data suggest that the photolyase active site is able to facilitate a delicately balanced competition between two reaction pathways that can be influenced by weak magnetic fields. Magnetic field-independent and dependent pathways are in competition in the enzymatic repair of CPDs, which allows a magnetic field to change how much of CPD is repaired or left intact. It is intriguing to consider how this chemistry may be used *in vivo* to inform magnetoreceptive behavior.

In a second line of work, electrochemistry and atomic force microscopy experiments were used to explore the ability of [4Fe-4S] cluster containing DNA processing enzymes to locate DNA damage using DNA CT. The [4Fe-4S] clusters in these proteins when they are freely diffusing are expected to be in the 2+ state. The proteins are activated towards oxidation upon binding to DNA. A given protein already bound to DNA in the oxidized form could thus be reduced in a DNA-mediated fashion by another distinct redox-active protein that binds within CT distance of the first protein. Reducing this second protein promotes its dissociation from DNA. Intervening DNA damage prevents DNA CT and the resulting dissociation.

Based on the model, we expect the redistribution of proteins that use DNA-mediated CT signaling onto strands containing a single base mismatch and away from fully matched duplex DNA, which is the observed result. Proteins that are defective in DNA CT do not relocate to the mismatched strand, as predicted by our model. The atomic force microscopy experiments show that proteins are not only able to signal with themselves, but mixtures of different 4Fe-4S cluster containing proteins, such as EndoIII and DinG, are able to signal with one another.

These observations using AFM are consistent with a DNA damage search scheme based on DNA-mediated redox signaling between proteins with oxidized and reduced [4Fe4S] clusters. Our data shows conclusively that this CT results in a change in affinity for each of the proteins. This change in redox state increases the effective affinity of these proteins for a duplex containing a mismatch because it allows for oxidized proteins to stay in the vicinity of the mismatch, or potentially any lesion that disrupts DNA CT, without being reduced and released from the duplex by another protein.

Our data show that the oxidation state of the [4Fe4S] clusters is integral to the ability of proteins to search for DNA damage, but that the identity of the protein is unimportant for DNA CT. The DNA-binding affinity depends on the oxidation state of the [4Fe4S] cluster in both EndoIII and DinG and likely holds true for other [4Fe4S] proteins. Importantly, these data show that DNA-processing proteins with different enzymatic functions can collaborate to find damage so long as the [4Fe4S] clusters are in different redox states. This DNA-mediated redox signaling between [4Fe4S] clusters may enable low copy number repair proteins to be aided by high copy number proteins to more quickly find and repair DNA damage.

Highlighted by this thesis work are three ways that DNA structure enables fascinating electrochemistry. The helicity of duplex DNA controls which electron spin migrates *through* the duplex with higher yield. Thymine dimer repair by photolyase and cryptochrome is exquisitely sensitive to magnetic fields thanks to radicals formed during the dimer breaking process, and a single base mismatch is able to disrupt DNA-mediated charge transport between [4Fe-4S] cluster containing proteins, which enables the proteins to efficiently locate DNA damage. Together, these experiments show that both small and large changes in structure can dramatically change the electrochemistry that DNA carries out. It is exciting consider the varied ways that functionality imparted by changes in DNA structure could be taken advantage of in practical devices and also how Nature may exploit this chemistry in some context.